

A POLYTOPAL ELEMENT FRAMEWORK FOR
IMPROVED SOLUTION ACCURACY AND ROBUSTNESS

By

BRIAN DORAN GIFFIN
B.S. (University of California, Davis) 2013
M.S. (University of California, Davis) 2014

DISSERTATION

Submitted in partial satisfaction of the requirements for the degree of

DOCTOR OF PHILOSOPHY

in

CIVIL AND ENVIRONMENTAL ENGINEERING

in the

OFFICE OF GRADUATE STUDIES

of the

UNIVERSITY OF CALIFORNIA

DAVIS

Approved:

MARK M. RASHID, CHAIR

N. SUKUMAR

BORIS JEREMIĆ

Committee in Charge

2017

Copyright © 2017 by
Brian Doran Giffin
All rights reserved.

To Lyle ...

*for teaching me how to think deeply, to analyze new information objectively, and to
appreciate the complexity and nuanced beauty in all things.*

And to Nancy ...

*for inspiring me to explore my creativity, for giving me canvases to paint on, and the
confidence to paint, without fear of failure.*

CONTENTS

List of Figures	v
List of Tables	ix
Abstract	xi
Acknowledgments	xii
1 Introduction	1
1.1 Historical Development	1
1.2 Recent Developments in Polytopal Discretization	9
1.3 Scope of the Present Work	13
2 An Overview of Computational Solid Mechanics	15
2.1 The Lagrangian Description of Motion	16
2.2 Conservation of Linear and Angular Momentum	18
2.3 Constitutive Relations	20
2.4 Model Boundary Value Problem	22
2.5 Galerkin Approximations to the Weak Form	25
2.6 Requirements for Convergence of an Approximation Method	28
3 Partitioned Element Methods	33
3.1 Overview	33
3.2 Definition of Polytopal Element Shape Functions	34
3.3 Shape Function Approximation Methods	37
3.4 Non-conforming Galerkin Approximations to (Generalized) Harmonic Shape Functions	40
3.5 Piecewise Polynomial Approximations to (Generalized) Harmonic Shape Functions	43
3.6 Partition-Based Quadrature Rules	52

4 An Implementational Framework	
for the DG-PEM	57
4.1 Arbitrary Polytopal Meshes	57
4.2 Element Partitioning Schemes	62
4.3 Abstract Geometric Data Structures	64
4.4 Partition-Based Approximation Spaces	67
4.5 Linearization and Assembly of the DG-PEM Systems of Equations	69
4.6 Numerical Conditioning of the DG-PEM Systems of Equations	73
5 A Numerical Evaluation of the PEM	76
5.1 Tests for Polynomial Reproducibility	76
5.2 Finite Element Patch Tests	82
5.3 Tests for Element Quality	91
5.4 Convergence Studies	103
5.5 Large Deformation Problems with Elasto-plastic Material Behavior	113
6 Conclusions and Future Work	121
A An Exact Solution for the Incompressible Twisting Annulus Problem	125

LIST OF FIGURES

2.1 A depiction of the motion of material points in a body Ω	16
3.1 A representative polyhedral element $\Omega \subset \mathbb{R}^3$, a polygonal face $F \subset \partial\Omega$, a linear edge $E \subset \partial F$, and a node V	35
3.2 The harmonic shape function corresponding to the indicated node V , defined hierarchically on each edge, face, and the element.	36
3.3 A representative polyhedral element $\Omega \subset \mathbb{R}^3$, and its hierarchical partition into cells, facets, segments, and vertices.	43
3.4 Polygonal element partitioning schemes: (top-left) edge-based partition, (top-right) node-based partition, (bottom-left) random Delaunay partition, (bottom-right) random Voronoi partition.	44
3.5 The CG-PEM approximation to a given harmonic shape function, defined hierarchically on the element's faces and edges.	46
4.1 Canonical node numbering schemes for a linear tetrahedral element (left) and a linear hexahedral element (right). Each of these standard orderings induce corresponding nodal orderings for each triangular or quadrilateral face of the element, as well.	58
4.2 Illustration of the data necessary to describe an arbitrary polyhedral element Ω_e . The local node ID ordering for the face F_1 shown would be $\{n_i\}_{i=1}^5 = \{14, 1, 9, 8, 13\}$	59
4.3 Illustration of the data necessary to describe a quadratic serendipity polyhedral element Ω_e . The local node ID ordering for the face F_1 shown would be $\{n_i\}_{i=1}^{10} = \{14, 34, 1, 18, 9, 26, 8, 32, 13, 33\}$	60
4.4 The resulting segment, facet, and cell decomposition for the proposed edge-based partitioning algorithm.	64

4.5	The resulting segment, facet, and cell decomposition for the proposed edge-based partitioning algorithm, applied to a quadratic serendipity polyhedral element.	64
4.6	A representative entity tree diagram for a 2-dimensional facet σ and its children.	65
4.7	A representative 2-dimensional sub-element $F \subset \partial\Omega$ (a polygonal face), and its corresponding sub-element tree diagram. The partition of F consists of polygonal facets $\sigma_i \in \mathcal{T}_\sigma(F) \forall i = 1, \dots, 5$	67
5.1	A representative polygonal element and its corresponding edge-based partition.	80
5.2	Depiction of the 2D linear patch test.	83
5.3	Meshes used for the linear patch test: (left) polygonal mesh, (right) distorted quadrilateral mesh.	83
5.4	Hexahedral meshes: (left) regular, (right) distorted.	86
5.5	Patch of polyhedral elements.	87
5.6	Depiction of the 2D quadratic patch test.	88
5.7	Quadrilateral meshes: (left) regular, (right) distorted.	89
5.8	Patch of serendipity polygonal elements.	89
5.9	Patch of serendipity polyhedral elements.	90
5.10	A representative sampling of hexagonal elements: (A) strictly convex, (B) two collinear edges, (C) non-convex.	93
5.11	Delaunay partitions for elements A, B, and C.	93
5.12	Comparison of the shape functions computed for elements A, B, and C using the VETFEM, CG-PEM, and DG-PEM.	94
5.13	Two convex pentagonal elements: (left) regular pentagon with edges of equal length $l = 1.0$, (right) pentagon with a comparatively short edge of length $l = 0.01$	97
5.14	Comparison of shape functions computed for the two pentagonal elements with $l = 1.0$ and $l = 0.01$ using VETFEM, CG-PEM, and DG-PEM.	98

5.15 Patches generated by PolyMesher, each containing 1,000 polygonal elements.	99
5.16 Histograms of various mesh metrics associated with the polygonal meshes depicted in Figure 5.15: (a) and (b) show the distributions of edge lengths contained in the random Voronoi and Lloyd meshes, respectively. (c) and (d) show the distributions for the smallest edge length ratios ρ_e in the random Voronoi and Lloyd meshes, respectively.	100
5.17 Eigenvalue spectra $\{\lambda_i\}_{i=1}^{N-3}$ for the (elastic) global stiffness matrix \mathbf{K} , computed for the CG-PEM and the DG-PEM ($\epsilon = +1$, $\alpha_{\gamma 1} = 0$).	101
5.18 Depiction of the smallest non-zero eigenvalues and corresponding eigenmodes computed using the DG-PEM ($\epsilon = +1$, $\alpha_{\gamma 0} = 10$, $\alpha_{\gamma 1} = 0$). N denotes the size of the global stiffness matrix \mathbf{K} , and $\lambda_N = \lambda_{N-1} = \lambda_{N-2} = 0$ correspond to the zero-energy modes of deformation.	102
5.19 Infinite plate with a circular hole placed in uniaxial tension.	104
5.20 Quadrilateral meshes with varying levels of refinement.	105
5.21 Convergence plots for the plate with hole problem using FEM and DG-PEM. 105	
5.22 Depiction of the twisting annulus problem.	107
5.23 Hexahedral meshes with varying levels of refinement for the twisting annulus problem.	108
5.24 Distorted hexahedral meshes with varying levels of refinement for the twisting annulus problem.	109
5.25 Polyhedral meshes with varying levels of refinement for the twisting annulus problem.	110
5.26 Convergence plots for the twisting annulus problem using FEM for hexahedra and DG-PEM for polyhedra.	111
5.27 Comparison of pressure fields for various element types and formulations. Color scales are kept consistent between similar mesh types.	112

5.28 Tensile specimen dimensions, in inches. The thickness of the plate specimen shown is 0.5 in., resulting in a square cross-section along the gage length. The area shown in grey represents the eighth-symmetric modeling domain.	114
5.29 Plate specimen meshes used for the tensile necking problem, modeled as an eighth-symmetric problem.	114
5.30 Comparison of necking behavior at 16.5% elongation, depicting deformed shapes and color map values of equivalent plastic strain $\bar{\epsilon}^p$ and von Mises stress σ_v (ksi).	115
5.31 Plotted results for the FEM and DG-PEM models, both with and without the kinematic enhancement discussed in [63]. The estimated point of rupture is indicated by an X in each plot.	116
5.32 Impact specimen meshes used for the Taylor bar problem, modeled using quarter-symmetry.	118
5.33 DG-PEM element inversion when using the kinematic enhancement of [63], viewed from the bottom of the mesh (the impacting surface).	119
5.34 Comparison of results between the FEM and PEM models at the final time $t = 0.08$ ms, depicting deformed shape and color map values of equivalent plastic strain $\bar{\epsilon}^p$	119
5.35 Comparison of von Mises stress σ_v (in Pascals) within the FEM and PEM models at the final time $t = 0.08$ ms.	120

LIST OF TABLES

5.1	Computed values of $E_1(\Omega)$ and $\kappa(\mathbf{J})$ for the element in Figure 5.1, using various DG-PEM penalty parameter settings.	80
5.2	Computed values of $E_1(\Omega)$ and $\kappa(\mathbf{J})$ for a comparatively thin element with an aspect ratio of 100:1, using various DG-PEM penalty parameter settings.	81
5.3	Linear patch test results comparison for FEM, CG-PEM, and DG-PEM.	84
5.4	Computed values of $\ \boldsymbol{\sigma}^h - \boldsymbol{\sigma}\ /\ \boldsymbol{\sigma}\ $ for the DG-PEM using various penalty parameter settings. No gradient correction scheme was utilized. Identical trends were observed for $\ \mathbf{u}^h - \mathbf{u}\ /\ \mathbf{u}\ $	85
5.5	The effects of interpolation error on patch test errors in the DG-PEM. No gradient correction scheme was utilized.	85
5.6	3D linear patch test results comparison for FEM and DG-PEM.	87
5.7	Quadratic patch test results comparison for FEM and DG-PEM.	89
5.8	3D quadratic patch test results comparison for FEM and DG-PEM.	91
5.9	Comparison of maximum and minimum (non-zero) eigenvalues of the element stiffness matrices for the elements shown in Figure 5.10.	95
5.10	Comparison of maximum and minimum (non-zero) eigenvalues of the element stiffness matrix for element C, computed for various DG-PEM penalty parameter values.	96
5.11	Comparison of maximum and minimum (non-zero) eigenvalues of the element stiffness matrices computed for the elements shown in Figure 5.13..	97
5.12	Computed values for the condition number $\kappa(\mathbf{K})$ of the global stiffness matrix \mathbf{K} (excluding rigid body modes).	103
5.13	Average and maximal convergence rates for each method. The optimal rates are shown in parentheses.	106
5.14	Average and maximal convergence rates for each element type/formulation. The optimal rates are shown in parentheses.	110

- 5.15 Tensile test data results comparison. The values of % elongation were recorded after reaching 60% reduction in area. 117
- 5.16 Measurements of the rod's final base diameter D_{final} and overall length L_{final} . 120

ABSTRACT

A Polytopal Element Framework for Improved Solution Accuracy and Robustness

A high-level discussion of the fundamental problems accompanying finite element discretizations in the form of locking, addressing the scope of the work under consideration.

ACKNOWLEDGMENTS

Many thanks to the following: Professor Amit Kanvinde who inspired much of my initial motivation for applying to graduate school; Professor N. Sukumar for exposing me to the realm of computational solid mechanics; Dr. Joseph Bishop at Sandia for being involved in my early (and continuing) development in the field of solid mechanics; Professor Mark Rashid who turned my spark of interest in the subject into a roaring fire of passion; Dr. Steven Wopschall and Mr. Omar Hafez for being my mentoring older brothers throughout my journey in graduate school; Mr. Subhajit Banerjee and Mr. Eric Chin whose fruitful discussions assisted greatly in developing a personal sense of calm and confidence prior to my qualifying examination; Professor Yannis Dafalias, Professor John Bolander, and Professor Elbridge Puckett, whose enthusiasm as lecturers and courtesy as QE examiners were indespensable; Dr. Joseph Jung, Dr. Kendall Pearson, Dr. Nathan Crane, Mr. Mark Merewether, Dr. Michael Tupek, and the whole of the Sierra Solid Mechanics Team at Sandia who introduced me to the fascinations of code development; Ms. Carly Arthur, Mr. Sam Mish, and Ms. Aimée Sylvia whose conversations as fellow class-mates and advisees were incredibly helpful and insightful; and foremost to Ms. Maha Kenawy, who has served as my primary role-model and source of inspiration for completing this thesis – I love you.

Chapter 1

Introduction

For decades, finite element methods (FEM) have been widely used by engineers and physicists in the modeling of solid continua. Numerous extensions of the method have been developed to model more complex physical processes, including nonlinear kinematic and material behavior. In spite of these advances, traditional finite element methods have been plagued by recurrent issues of numerical accuracy pertaining to locking and poor mesh quality. Various strategies have been proposed to overcome some of these issues, though few have been able to address the underlying problem of element distortion sensitivity.

This thesis presents a novel polytopal element framework in an effort to address the aforementioned issues as a whole. The use of arbitrary polygonal and polyhedral shapes in place of canonical isoparametric element shapes seeks to resolve the issue of distortion sensitivity directly, obviating issues of meshing and mesh quality, while maintaining many of the desirable features of the FEM and its extensions.

1.1 Historical Development

According to [30], finite element methods originated in the 1950s to address engineering challenges in, among other things, the design of aircraft. The method was subsequently given a more rigorous mathematical treatment by early contributors (Irons, Melosh, Strang), and its usage permeated to other fields of study (namely, structural engineering). Following the advent of the isoparametric element concept, displacement-

based finite element formulations gained widespread popularity. Most early applications considered only linear kinematic and material behavior. Subsequently, advanced solution methodologies were developed to accommodate various sources of nonlinearity, including finite deformations, nonlinear constitutive behavior, and contact.

Over half a century after its initial development, the finite element method is still widely used, and recognized as the industry standard technology for modeling complicated structural and dynamic systems. Its reigning popularity can be attributed to several desirable features of the method:

- The compact support property of the isoparametric basis functions helps to facilitate more efficient solution methodologies. In particular, the assembly of finite element systems of equations is made more efficient by an element-wise assembly process.
- The Kronecker delta property and precise description of mesh boundaries allow for a relatively straightforward application of boundary conditions and contact constraints.
- Numerical quadrature on element domains derived from product Gauss rules balances accuracy, efficiency, and stability. Domain quadrature rules also naturally accommodate nonlinear kinematic behavior and “black box” constitutive models.

However, despite these advantageous characteristics, finite element methods have suffered from two major (related) issues:

- I.) Standard element formulations are prone to the effects of numerical locking phenomena, which can significantly degrade the accuracy of the method. These issues are more prevalent for low-order elements, especially for linear triangles and tetrahedra. Moreover, very thin or distorted elements tend to exhibit more severe pathologies.
- II.) The process of discretizing complex geometries into traditional finite element shapes is not always possible with current automated meshing techniques. Contemporary meshing tools typically require extensive human intervention to produce meshes for complex shapes. This process is further encumbered by the aforementioned concerns

over locking, to the extent that it becomes difficult – if not impossible – to produce quality discretizations within a reasonable amount of time.

Despite recent efforts to pursue automated quad-dominant [64] and hex-dominant [36] meshing algorithms which seek to optimize certain mesh quality metrics, the inherent problem of element distortion sensitivity still remains. Consequently, substantial efforts have been made to address the locking problem through a variety of approaches. An overview of locking and its remedies is given in the following section.

Locking in Finite Elements

Locking, as a general phenomenon [7], is characterized by a drastic loss of solution accuracy and/or convergence for particular choices of material or discretization parameters. In mathematical terms, an approximation method is deemed *robust* (with respect to a given problem parameter) if its numerical solution converges “uniformly” to the exact solution under mesh refinement, for all values of the indicated problem parameter. Conversely, a method is said to exhibit *locking* if the accuracy of the numerical solution degenerates as the chosen problem parameter approaches some limiting value.

As a specific example, one of the most commonly discussed and addressed forms of locking in computational solid mechanics is the issue of *volumetric locking*, wherein displacement-based element formulations suffer from a marked loss of accuracy when utilized to model the deformation of nearly incompressible materials. For an isotropic linear elastic material model, the parameter dependency in question relates to the Poisson’s ratio of the material.

Other forms of locking may manifest as a sensitivity to geometric/discretization parameters. These are collectively referred to as *geometric locking* phenomena, which include: *shear locking*, which is linked to the aspect ratio of continuum elements subjected to bending-dominated deformations; *membrane locking*, which occurs in curved shell elements (see [86]); and *trapezoidal locking*, which affects the bending response of distorted four-node quadrilateral elements (see [52]).

Early efforts to address locking sought to develop more robust discretizations through the use of higher-order elements. In [6] and [75], Babuška and Suri rationalized the

ability of high-order elements to overcome the effects of volumetric locking (for triangular discretizations). The improved convergence behavior of these elements made them an attractive option for seeking efficiency gains, as well. Nonetheless, higher-order elements were generally seen as too complex in comparison with the standard low-order elements commonly used for commercial applications. For example, many cite the relative difficulty of obtaining lumped mass matrices for high-order elements [43]. Moreover, the accuracy of high-order isoparametric elements can be severely degraded if the elements possess curved edges, as demonstrated in [49].

As an alternative to the standard displacement-based FEM, some have argued for the use of *mixed finite element methods* (MFEM), which provide, in the most general case, a separate interpolation of the displacement, strain, and stress fields. Mixed methods are derived from a 3-field Hu-Washizu variational principle in the specification of the weak form. While these methods are generally less vulnerable to locking (as noted in [6] and [7]), they are not altogether immune to its effects. Moreover, mixed methods are subject to potential issues of stability, i.e. the Babuška-Brezzi – or inf-sup – conditions ([5], [13].) Additionally, mixed methods tend to be less efficient in comparison with displacement-based FEM, and are not as flexible in their ability to handle arbitrary constitutive relationships.

In an effort to retain some of the beneficial characteristics of mixed finite element methods, *(mixed) assumed strain methods* were formalized for geometrically linear problems in [71], and extended to nonlinear problems in [69] and [70]. Assumed strain methods are closely related to the *method of incompatible modes* first proposed by Wilson [85], which considers the inclusion of additional element-specific modes of deformation that allow for discontinuities in the resulting displacement field at element boundaries. By contrast, assumed strain methods are derived from a 3-field variational principle, and rely upon energy orthogonality between an enhanced strain field and the resulting stress field to eliminate the need for an independent stress interpolation space. Assumed strain methods may therefore be viewed as a class of mixed 2-field formulations, involving a compatible displacement field and an enhanced/assumed strain field. Though the method is effective

in treating a variety of geometric locking phenomena, it nonetheless leads to spurious instabilities in both linear and nonlinear problems (see [76] and [59], respectively), even for element formulations satisfying the inf-sup conditions.

Other attempts to adapt mixed formulations for more general use with arbitrary material models without relying upon an explicit interpolation of the stress or strain fields include *selective reduced integration* (SRI) and equivalent *strain projection* techniques. These methods were fairly successful in overcoming the issues of volumetric locking via the B-bar projection approach for linear problems discussed in [43], and via the F-bar approach for nonlinear problems discussed in [23]. Though these methods can be both effective and efficient, their success has been limited to the problem of volumetric locking; they are somewhat less successful with regard to treating other forms of locking, such as shear locking in continuum finite elements (as noted in [53]). Also, SRI can lead to stability problems if the strain projection spaces are not selected carefully.

At the opposite end of the spectrum – in recognition of the inherent issues of stability plaguing mixed methods and reduced integration techniques, methodologies employing *orthogonal hourglass control* have been suggested [32]. These approaches consider the use of low-order quadrature rules to avoid common locking phenomena, supplemented by artificial stiffness terms to maintain stability while preserving essential convergence characteristics. While these formulations tend to be highly efficient computationally (particularly for explicit dynamics analyses), the obvious disadvantage of these approaches relates to their reliance upon user-specified artificial stiffness and viscosity parameters. Appropriate selection of these parameters is not always a trivial matter, and often warrants problem-specific investigations via sensitivity analyses.

Ultimately, the foregoing methodologies have had only limited success in resolving the full spectrum of locking problems, particularly with regard to geometric locking phenomena. Moreover, many of the proposed enhancements are limited to specific element types (typically low-order quadrilaterals or hexahedra), and are not readily generalizable to other discretizations.

Alternative Numerical Methods and Discretizations

Driven primarily by concerns over meshing (and additionally by concerns over element quality), a variety of alternative approximation methods have been explored in recent decades.

In direct response to these considerations, so-called *mesh-free* methods were developed in an effort to construct approximation spaces that are defined independently of a mesh. Mesh-free methods encompass a broad class of approximation schemes, including smoothed particle hydrodynamics (SPH), the element-free Galerkin (EFG) method, the natural element method (NEM), and the reproducing kernel particle method (RKPM), among others. A majority of these methods rely upon an *a priori* specification of weighting functions used to construct an associated set of polynomially reproducing basis functions. The resulting mesh-free basis yields relatively smooth solutions which are less sensitive to the specific choice and distribution of weighting functions.

The departure from defining an approximation space on a structured partition of the domain presents a number of challenges, however. Specifically, mesh-free methods still require the definition of a background mesh to effect numerical integration of the weak form, partially invalidating the namesake of the method. Moreover, because the mesh-free basis functions are typically non-polynomial in form (and because their supports are not disjoint on element domains), they are more challenging to accurately integrate.

Chen et al. have proposed a means of overcoming these issues in [15] through a *variationally consistent integration* scheme, though this approach is susceptible to numerical instabilities. Additionally, because the basis functions do not in general exhibit the Kronecker delta property, the application of boundary conditions and contact constraints becomes less straightforward. Several techniques have been proposed to address this issue [31], including Lagrange multiplier methods, Nitsche's method, and mesh blending at domain boundaries.

As another alternative, *discontinuous Galerkin* (DG) methods have gained recent attention due to their more flexible representation of solution fields as piecewise polynomials over individual elements, resulting in solution discontinuities at element boundaries. To

stabilize the resulting approximation space, DG methods supplement the weak form with interior penalty terms that seek to minimize these discontinuities. A detailed review of several primal interior penalty DG schemes may be found in [65]. DG methods are advantageous in that they may accommodate arbitrary element shapes, and exhibit desirable distortion robustness characteristics.

DG approaches are not without their own problems, however. One commonly cited issue relates to the fact that DG methods can become sensitive to the choice of penalty parameters used to weakly enforce inter-element continuity and boundary conditions. Indeed, the selection of these parameters is problem dependent. Additionally, DG methods tend to suffer from poor numerical conditioning problems if the discretization does not conform to relatively stringent regularity requirements, thereby limiting the types of discretizations used with the method.

The more recent *weak Galerkin* (WG) finite element method first introduced by Wang and Ye for elliptic problems in [82], and for parabolic equations by Li and Wang in [50], pursues the discretization of a (2D) problem domain into polygonal elements and element edges. The method considers a space of “weak functions” defined independently on element interiors and their boundaries, such that for any function $v = \{v|_{\Omega}, v|_{\partial\Omega}\}$, its (discrete) “weak gradient” $\nabla_{w,k}v \in V(\Omega, k)$ is defined on the interior of a given element $\Omega \subset \mathbb{R}^d$ through its action on a vector field $\mathbf{q} \in V(\Omega, k)$:

$$\int_{\Omega} \mathbf{q} \cdot \nabla_{w,k}v \, dA = - \int_{\Omega} v|_{\Omega} \nabla \cdot \mathbf{q} \, dA + \int_{\partial\Omega} v|_{\partial\Omega} \mathbf{q} \cdot \mathbf{n} \, dS, \quad \forall \mathbf{q} \in V(\Omega, k), \quad (1.1)$$

where $V(K, k) \subset [P^k(\Omega)]^d$ is a subspace of the vector-valued polynomials of maximal degree k defined on Ω . A weak Galerkin approximation method uses the discrete weak gradient operator in place of the classical gradient.

The discrete approximation spaces under consideration are typically low-order polynomials (commonly just constants) defined on the elements and their edges. However, there are some non-trivial choices that must be made regarding an optimal selection of these polynomial spaces for the sake of computational efficiency (discussed in greater detail in reference [57]). The method has so-far only been applied to the solution of linear problems.

The computational accuracy of the weak Galerkin approach has been explored by Mu et. al. in [55], showing that for certain problems, the weak Galerkin method converges at rates comparable to those of the standard FEM. Lin et. al. performed a comparative study between the weak Galerkin, discontinuous Galerkin, and mixed finite element methods in [51], demonstrating some of the competitive and desirable characteristics of WG in contrast to DG or MFEMs: no need for penalty parameters, and definiteness of the resulting linear system of equations.

Mu et. al. adapted the method for use on arbitrary polytopal meshes in [56] and [57], albeit with a number of shape regularity restrictions placed on the elements. In general, the implementation of WG considers the mesh degrees of freedom as belonging to both the elements and their edges, however in [57] it is noted that the local element degrees of freedom can be expressed in terms of the bounding edge degrees of freedom alone, to improve computational efficiency. A modified approach by Wang et. al. in [83] instead chooses to express functions on edges only implicitly. Although this approach successfully eliminates the computational expense associated with edge-based degrees of freedom, it requires the inclusion of an additional interior penalty term in the weak form, similar to a discontinuous Galerkin method.

In the wake of these investigations, it becomes clear that the combination of desirable properties held by the FEM (compact support, Kronecker delta, quadrature efficiency, DoF efficiency, stability, and inter-element compatibility) are qualities worth preserving. To this end, recent efforts within the numerical methods development community have focused on improving and generalizing existing element formulations for arbitrary element shapes – polygons and polyhedra. Rather than relying upon shape functions defined through an isoparametric transformation from a parent element domain, recent polytopal element methodologies have explored various techniques for constructing approximants directly on physical element domains. In doing so, issues regarding distortion sensitivity of the elements are largely obviated, and new opportunities for discretizing the domain with irregular shapes are made possible. In like fashion, recent advances in meshing technologies have made polyhedral element methods a readily feasible option. Very recently,

Ebeida et. al. have released VoroCrust [28]: a robust voronoi discretization tool based on constrained Poisson disk sampling. Concurrent technologies have also advanced polyhedral mesh generation via boolean intersection of a background hexahedral mesh with a piecewise linear boundary representation (or B-rep).

For these reasons, efficient and robust polyhedral element formulations are in high demand, leading to a proliferation of new approaches. A number of these are discussed in the following section.

1.2 Recent Developments in Polytopal Discretization

Polytopal element methods combine many of the attractive features of FEM with the geometric flexibility afforded by arbitrary element shapes, the primary motivation for which arises from the aforementioned concerns over discretization sensitivity. Most of these methods share a few distinguishing features in common with one another: mesh degrees of freedom are borne by nodes – the geometric vertices of (low-order) elements; nodal basis functions are compactly supported over adjoining element domains, and satisfy the Kronecker delta property; basis functions are defined directly on the element’s physical domain, rather than on a parent domain.

Where these methods differ is in the way that they choose to define an element’s shape functions (if at all). These approaches may be loosely organized into three distinct categories: methods which explicitly define the element’s basis functions via a continuous interpolation scheme; methods which define the element’s shape functions only implicitly – i.e. “virtual” element methods; and methods which form a discrete representation of the element’s shape functions via an approximation scheme. These three methodologies are elaborated upon in the following sections.

Continuous Interpolation on Arbitrary Polytopes

A key advantage of isoparametric elements relates to their straight-forward, point-wise definition of an element’s shape functions. In an effort to preserve this desirable characteristic, various authors have sought to explicitly define shape functions directly on arbitrary polytopal element domains. These efforts have led to the creation of a broad family of

interpolation schemes, collectively referred to as *generalized barycentric coordinates*.

At a minimum, shape functions which fall into this category must: form a partition of unity, satisfy linear completeness, and interpolate the nodal data (i.e. satisfy the Kronecker delta property). These coordinates are uniquely defined according to the standard barycentric coordinate system for simplicial domains. For arbitrary polytopal domains, numerous such coordinate systems exist, including Wachspress' coordinates [81], mean value coordinates [33], harmonic coordinates [46], and maximum entropy coordinates [74], among others. In many cases, such coordinates are restricted to strictly convex polytopes.

Though generalized barycentric coordinates have been applied in the context of finite elements, their development has largely been propelled by the graphics community on account of their relatively smooth interpolatory properties. However, the smooth (non-polynomial) character of the shape functions presents a challenge with regard to accurate numerical integration. Consequently, relatively high-order quadrature schemes are required to achieve reasonable solution accuracy and satisfaction of patch tests. More recently, a polynomial projection scheme has been suggested in [77] to remedy these integration errors for linear problems; for general nonlinear problems, a gradient correction scheme has been proposed in [79] and [17]. These developments have illuminated new possibilities for defining more efficient quadrature rules on polytopes, while still satisfying the essential requirements for convergence.

Yet in spite of these developments, many existing coordinate schemes are still limited by moderate to severe restrictions on element shape/convexity, and produce sharp gradients in the presence of degenerate geometric features. These concerns, and a recognition of the fact that the shape functions need not be defined point-wise for finite element applications, have motivated research efforts toward discrete representations of element interpolants.

Virtual Element Methods

The *virtual element method* (VEM) summarized in [21] is a relatively new approach, based in part upon the older concept of mimetic finite differences (MFD). Although the method supposes that continuous basis functions *exist* within arbitrary polytopal elements, the VEM never explicitly *defines* how these shape functions vary on element

interiors. Instead, the VEM supposes that these “virtual” functions may be separated (via projection operators) into polynomial and non-polynomial parts, which are handled in different ways. The cornerstone of the method is the idea that the bilinear form for a given element may be decomposed into two distinct parts: a term which guarantees variational consistency (Galerkin exactness) involving the low-order polynomial part of the shape functions, and a term which provides stability involving the non-polynomial part. The consistency term must be integrated exactly, but the stability term can be evaluated approximately. Because this decomposition relies upon the linearity of the bilinear form, direct generalizations of the method to nonlinear problems are not immediately available.

VEM has been applied to three-dimensional linear elasticity problems in [35]. In [22], a VEM formulation for low-order elements which accommodates nonlinear “black-box” constitutive algorithms is presented, and in [16] an extension to finite deformations (with appropriate stabilization terms) is introduced. Given the means by which these approaches exploit the use of a projected uniform gradient to integrate the weak form, however, it is unclear how they could be extended to accommodate higher-order elements.

Nonetheless, VEM formulations are able to tolerate geometric degeneracies and element non-convexity without encountering serious numerical difficulties, though their good behavior in the presence of these features is often governed by an ad hoc approximation of the stabilization terms. A more rigorous development of the corresponding stability terms for more complicated element domains remains to be explored.

Approximate Interpolation on Arbitrary Polytopes

In contrast with the previously described approaches, yet another strategy considers the representation of the element’s shape functions in an approximate way, while enforcing a few essential requirements, namely: polynomial reproducibility, inter-element compatibility, and weak form consistency.

In [61] and [63], Rashid and co-workers explored the *variable element topology finite element method* (VETFEM), characterized by an approximate representation of the element’s shape functions as low-order polynomials satisfying weak continuity requirements at element boundaries. Within this framework, the element shape functions are deter-

mined by a local minimization problem, resulting in polynomial shape functions which optimize specified continuity and smoothness objectives. This minimization procedure is constrained by the requirements of consistency and reproducibility to guarantee satisfaction of linear patch tests. Dohrmann and Rashid later extended this approach to higher-order elements in [24], instead focusing on a direct construction of shape function derivatives, rather than of the shape functions themselves.

The VETFEM may be viewed as a non-conforming finite element method, as the minimization process altogether allows for residual discontinuities at inter-element boundaries. Nonetheless, because the elements satisfy weak continuity requirements, the method exhibits proper convergence characteristics. Additionally, because the VETFEM yields a point-wise representation of the shape functions as low-order polynomials, direct integration of the weak form can be carried out using relatively efficient domain quadrature rules.

Although the VETFEM was developed to handle arbitrary polygonal elements, it was observed to suffer from sensitivity to geometric degeneracies and element non-convexity. In response to these issues, a *discrete data polyhedral finite element method* (DDPFEM) proposed in [68] was suggested to exploit the fact that for typical solid mechanics applications, it is generally only necessary to evaluate the element's shape functions (and their derivatives) at a discrete number of quadrature points. The proposed method shares several characteristics in common with the VETFEM, utilizing a similarly posed constrained minimization procedure to obtain the precise values and gradients of the shape functions at discrete points on the element's interior. One of the cited challenges with this approach pertains to the appropriate selection of an efficient quadrature rule for the elements.

Nonetheless, the initial thoughts put forward by the DDPFEM ultimately led to the development of the *partitioned element method* (PEM) presented in [62]. The PEM proceeds by partitioning an element into polygonal quadrature cells, and allowing the element's shape functions to vary according to a local polynomial defined within each of these cells, resulting in piecewise polynomial shape functions which are discontinuous at quadrature cell boundaries. The polynomial coefficients defined in each cell are obtained

by minimizing the discontinuities in the shape functions across all cell interfaces, subject to the necessary consistency and reproducibility constraints. The original presentation in [62] considers the shape functions to be approximate solutions of Laplace’s equation on the partitioned element. Later developments have dispensed with this supposition, instead only penalizing discontinuities in the shape functions (and their gradients) at cell boundaries.

Subsequently, Bishop has proposed a very similar partitioned element scheme in [11], wherein the elements and their faces are subdivided into simplices, resembling a local FE discretization of the element domain. The shape functions are obtained as the solution to Laplace’s equation on this subdivision. Because this approach utilizes an FE-like discretization, the resulting shape functions are piecewise linear and C^0 continuous, thereby avoiding the need for a penalty term to enforce continuity. However, the method still requires the use of a gradient correction scheme to account for quadrature error and recover consistency with the weak form.

In light of these developments, we choose to recognize a new class of methods, herein collectively referred to as *partitioned element methods*. These may be viewed as a generalization of the original PEM presented in [62]. It is the subject of this thesis to further explore these methods, and to expose their particular merits and potential shortcomings.

1.3 Scope of the Present Work

In this work, we put forth a general framework for partitioned element methods – a collection of different approaches for constructing approximate representations of element shape functions on arbitrary polytopes. These methods are characterized by several distinguishing features:

- (1) Elements are discretized (partitioned) into non-overlapping polygonal cells. These cells are used to inform the quadrature rule of the element.
- (2) A local approximation space is defined on the partitioned element geometry.
- (3) A set of BVPs and appropriate constraints are posed, whose solutions yield the shape functions of the element.

- (4) A stable numerical scheme is developed to obtain approximate solutions to these BVPs using the approximation space defined in (2).

Numerous formulations are possible within this framework; a few of these are explored within the scope of this thesis.

The proposed application area of interest for these methods is in nonlinear solid mechanics. The efficacy of the methods explored will be assessed within this context, particularly with regard to their ability to naturally accommodate nonlinear kinematic and material behavior. The robustness of the resulting elements, and their performance in the face of locking phenomena will be evaluated. Additionally, several methodologies which leverage the partitioned element framework to combat certain forms of locking will be discussed.

The remainder of this dissertation is organized as follows: chapter 2 establishes the context of nonlinear computational solid mechanics, chapter 3 presents the overarching framework for partitioned element methods, chapter 4 details a particular implementational framework for the PEM, chapter 5 provides a number of numerical investigations of the PEM, and chapter 6 concludes with a discussion of opportunities for further research and development.

Chapter 2

An Overview of Computational Solid Mechanics

This chapter addresses some of the essential aspects of numerical approximation methods for modeling solid continua. The discussion herein will focus on the mathematical foundations of solid mechanics, beginning with the kinematics of motion and some common forms of constitutive relationships, followed by the expressions for conservation of momentum in both strong and weak form, and concluding with an analysis of the standard numerical methods utilized to solve these equations in an approximate sense. In the course of our discussion, we will make explicit the ensuing requirements placed upon any prospective approximation scheme. This will aid our analysis in subsequent chapters, and hopefully justify particular choices made in the construction of partitioned element methods.

2.1 The Lagrangian Description of Motion

Consider a body $\mathcal{B}_0 \subset \mathbb{R}^d$ consisting of a set of material points whose positions in some reference configuration at time $t = 0$ are denoted \mathbf{X} . At a later time $t > 0$, the body occupies a new configuration $\chi(\mathcal{B}_0, t) = \mathcal{B}_t \subset \mathbb{R}^d$, such that the motion of individual material points yield new spatial positions \mathbf{x} according to the bijection $\chi_t : \mathbf{X} \leftrightarrow \mathbf{x}$, i.e.

$$\mathbf{x} = \chi(\mathbf{X}, t), \quad \mathbf{X} = \chi^{-1}(\mathbf{x}, t). \quad (2.1)$$

The displacement \mathbf{u} of a given material point may be expressed as $\mathbf{u} = \mathbf{x} - \mathbf{X}$, and its corresponding velocity is denoted $\mathbf{v} = \dot{\mathbf{x}} = \partial \mathbf{x} / \partial t$. Figure 2.1 provides a visual interpretation of the situation described.

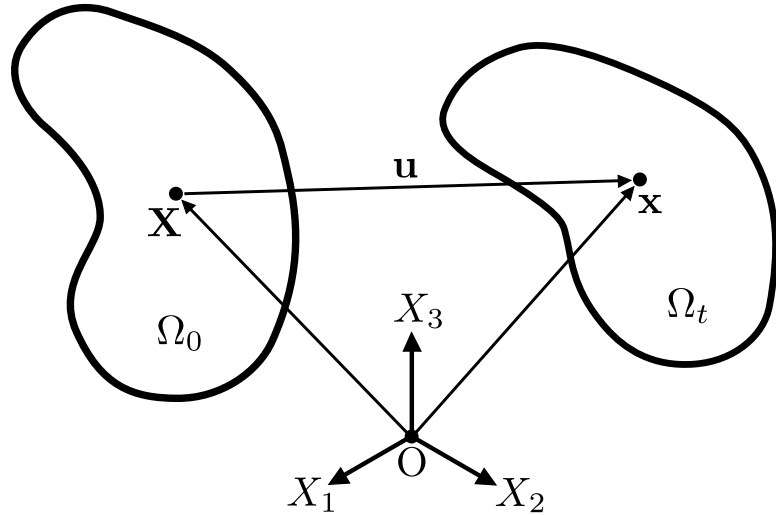


Figure 2.1: A depiction of the motion of material points in a body Ω .

At a given time t , the Jacobian of the deformation mapping χ_t yields the deformation gradient $\mathbf{F} = \nabla_{\mathbf{X}} \mathbf{x}$ (a rank-2 tensor), defined as

$$\mathbf{F} = \frac{\partial \mathbf{x}}{\partial \mathbf{X}} = \mathbf{1} + \nabla_{\mathbf{X}} \mathbf{u}, \quad (2.2)$$

where $\nabla_{\mathbf{X}}$ denotes the gradient with respect to \mathbf{X} . The deformation gradient may be used to map differential line segments $d\mathbf{X}$, surface areas $d\mathbf{A}$, and volumes dV defined in the reference configuration into their corresponding transformed quantities ($d\mathbf{x}$, $d\mathbf{a}$, dv) at time t :

$$d\mathbf{x} = \mathbf{F} d\mathbf{X}, \quad d\mathbf{a} = J \mathbf{F}^{-T} d\mathbf{A}, \quad dv = J dV, \quad (2.3)$$

where $J \equiv \det \mathbf{F}$.

In like fashion, the spatial velocity gradient $\mathbf{L} = \nabla_x \mathbf{v}$ (where ∇_x denotes the gradient with respect to \mathbf{x}) may be expressed as

$$\mathbf{L} = \frac{\partial \mathbf{v}}{\partial \mathbf{x}} = \frac{\partial \dot{\mathbf{x}}}{\partial \mathbf{X}} \frac{\partial \mathbf{X}}{\partial \mathbf{x}} = \dot{\mathbf{F}} \mathbf{F}^{-1}, \quad (2.4)$$

which may be further decomposed into a symmetric part \mathbf{D} (the rate of deformation tensor) and an anti-symmetric part \mathbf{W} (the spin tensor):

$$\mathbf{D} = \frac{1}{2}(\mathbf{L} + \mathbf{L}^T), \quad \mathbf{W} = \frac{1}{2}(\mathbf{L} - \mathbf{L}^T). \quad (2.5)$$

Compatibility

Compatibility refers to the idea that a given body remains a contiguous medium following some deformation described by χ_t . In other words, χ_t must characterize a continuous mapping of material points between different configurations in time, such that the topology of body remains unchanged. Compatibility is characterized by the following necessary and sufficient conditions:

$$\nabla_X \times \mathbf{F} = \mathbf{0} \quad \forall \mathbf{X} \in \mathcal{B}_0. \quad (2.6)$$

Satisfaction of the above compatibility condition implies that there exists a continuous, single-valued displacement field which gives rise to the deformation characterized by \mathbf{F} .

Finite Strain Measures

Consider the set of all material line segments $d\mathbf{X}$ which lie in a small neighborhood around a given material point \mathbf{X} . Also, consider these same material line segments $d\mathbf{x}$ in the current configuration of the body after some deformation corresponding to $\mathbf{F}(\mathbf{X}, t)$ has taken place, such that $d\mathbf{x} = \mathbf{F}d\mathbf{X}$.

At a given material point \mathbf{X} , the deformation gradient $\mathbf{F}(\mathbf{X}, t)$ is a linear operator, which may be decomposed into two step-wise operations: a stretching operation \mathbf{U} (or \mathbf{V}), and a rotation \mathbf{R} , yielding the polar decomposition of \mathbf{F} :

$$\mathbf{F} = \mathbf{R}\mathbf{U} = \mathbf{V}\mathbf{R}, \quad (2.7)$$

where \mathbf{U} is termed the right stretch tensor, and \mathbf{V} is the left stretch tensor. There arise from \mathbf{U} and \mathbf{V} two primary deformation measures: the right Cauchy-Green deformation

tensor $\mathbf{C} = \mathbf{U}^2$, and the left Cauchy-Green deformation tensor $\mathbf{B} = \mathbf{V}^2$. Each of these, in turn, yield the two most commonly utilized finite strain measures: the Green-Lagrangian strain tensor $\mathbf{E} = \frac{1}{2}(\mathbf{C} - \mathbf{I})$, and the Eulerian-Almansi strain tensor $\mathbf{e} = \frac{1}{2}(\mathbf{I} - \mathbf{B}^{-1})$. It is not difficult to show that both of these strain measures reduce to the small strain tensor $\boldsymbol{\varepsilon} = \frac{1}{2}(\nabla_X \mathbf{u} + (\nabla_X \mathbf{u})^T)$ if the displacements are sufficiently small.

Another finite strain measure that has gained attention in more recent years is the Hencky (logarithmic, or “true”) strain tensor $\mathbf{H} = \frac{1}{2} \log \mathbf{B}$. Because the Hencky strain tensor belongs to the Seth-Hill family of strain measures (as do the Green-Lagrangian and Eulerian-Almansi strain tensors), it likewise is seen to reduce to the small strain tensor in the limit of small displacements.

2.2 Conservation of Linear and Angular Momentum

For a given material body $\mathcal{B}_t \subset \mathbb{R}^d$, any open subset $\Omega_t \subset \mathcal{B}_t$ must satisfy Newton’s second law of motion, such that the net external force which acts upon Ω_t is equal to the total change in linear momentum of the system, i.e.

$$\frac{d}{dt} \int_{\Omega_t} \rho \mathbf{v} dv = \int_{\Omega_t} \rho \mathbf{b} dv + \int_{\partial\Omega_t} \mathbf{t} da \quad \forall \Omega_t \subset \mathcal{B}, \quad (2.8)$$

where ρ is the mass density of the material, \mathbf{v} is the velocity field, \mathbf{b} is an applied body force per unit of mass, and \mathbf{t} is the traction vector – a force per unit of area – which acts on $\partial\Omega_t$ (the boundary of Ω_t). Via the Cauchy tetrahedron argument, it is possible to express the traction vector $\mathbf{t}(\mathbf{n})$ as a linear function of the unit vector \mathbf{n} , which is normal to the surface upon which the traction acts:

$$\mathbf{t} = \mathbf{n} \cdot \boldsymbol{\sigma}, \quad (2.9)$$

where $\boldsymbol{\sigma}$ is referred to as the Cauchy stress tensor. Invoking the divergence theorem, we may utilize the above relation to convert the traction boundary integral into a volume integral over Ω_t :

$$\int_{\partial\Omega_t} \mathbf{t} da = \int_{\partial\Omega_t} \mathbf{n} \cdot \boldsymbol{\sigma} da = \int_{\Omega_t} \nabla_x \cdot \boldsymbol{\sigma} dv. \quad (2.10)$$

Moreover, utilizing Reynolds' transport theorem, conservation of mass, and a change of variables in \mathbf{x} and \mathbf{X} , it is possible to show that

$$\frac{d}{dt} \int_{\Omega_t} \rho \mathbf{v} dv = \int_{\Omega_t} \rho \frac{d\mathbf{v}}{dt} dv, \quad (2.11)$$

which ultimately yields

$$\int_{\Omega_t} [\rho(\mathbf{b} - \dot{\mathbf{v}}) + \nabla_x \cdot \boldsymbol{\sigma}] dv = \mathbf{0} \quad \forall \Omega_t \subset \mathcal{B}. \quad (2.12)$$

Since we have imposed no limitations on the choice of subset Ω_t , we may invoke the localization theorem to determine a point-wise statement of equilibrium in the body \mathcal{B}_t :

$$\rho(\mathbf{b} - \dot{\mathbf{v}}) + \nabla_x \cdot \boldsymbol{\sigma} = \mathbf{0} \quad \forall \mathbf{x} \in \mathcal{B}_t. \quad (2.13)$$

Similarly, by formulating an expression for the conservation of angular momentum, we obtain an additional point-wise requirement on the symmetry of the Cauchy stress tensor:

$$\boldsymbol{\sigma} = \boldsymbol{\sigma}^T \quad \forall \mathbf{x} \in \mathcal{B}_t. \quad (2.14)$$

Measures of Stress

As expressed earlier, the Cauchy stress tensor $\boldsymbol{\sigma}$ relates the normal \mathbf{n} of a given surface area element $d\mathbf{a} = \mathbf{n} da$ to the corresponding force per unit of area \mathbf{t} which acts on that surface, where the surface element $d\mathbf{a}$ is defined in the current configuration of the body (at some time $t > 0$). The total force which acts on a given surface $d\mathbf{a}$ is then

$$d\mathbf{f} = \mathbf{t} da = \boldsymbol{\sigma}^T d\mathbf{a}. \quad (2.15)$$

Utilizing Nanson's formula for area transformations:

$$d\mathbf{a} = J \mathbf{F}^{-T} d\mathbf{A}, \quad (2.16)$$

we may consider an equivalent representation of $d\mathbf{f}$, such that

$$d\mathbf{f} = J \boldsymbol{\sigma}^T \mathbf{F}^{-T} d\mathbf{A} = \mathbf{P} d\mathbf{A} = \mathbf{p} dA, \quad (2.17)$$

where \mathbf{P} is defined as the first Piola-Kirchhoff stress tensor (which in general is not symmetric.), and where $\mathbf{p} = \mathbf{N} \cdot \mathbf{P}^T$ is the corresponding Piola traction vector, characterizing

the distributed force which acts over a surface defined in the reference configuration with area dA and normal \mathbf{N} .

Another stress measure (related to the first Piola-Kirchhoff stress) is the second Piola-Kirchhoff stress tensor \mathbf{S} , and is commonly defined as the pull-back of the Kirchhoff stress tensor $\boldsymbol{\tau} = J\boldsymbol{\sigma}$:

$$\mathbf{S} = \mathbf{F}^{-1}\boldsymbol{\tau}\mathbf{F}^{-T}. \quad (2.18)$$

2.3 Constitutive Relations

Fundamentally, we require there to be some relationship between the forces applied to a given body, and its observed deformation. Such relationships are generally referred to as constitutive models, which characterize a macroscopic connection between stress and strain in a continuum.

Models of Elasticity

Constitutive models have variable forms, mostly notably as they relate to notions of elasticity: the tendency of a material to revert to its original undeformed configuration if the applied forces are removed. Models for elastic material behavior fall into three primary categories: hyperelasticity, Cauchy-elasticity, and hypoelasticity.

Hyperelasticity is concerned with the description of a material's state through an elastic potential function, which expresses the total stored elastic strain energy $W(\mathbf{F})$ in the material as a function of the total deformation measured from some (nominally undeformed) reference configuration. Differentiation of this potential with respect to a given deformation measure will yield an expression for the corresponding work-conjugate measure of stress, e.g.

$$\mathbf{P} = \frac{\partial W}{\partial \mathbf{F}}, \quad \mathbf{S} = \frac{\partial W}{\partial \mathbf{E}}. \quad (2.19)$$

Some common examples of hyperelastic models include the St. Venant-Kirchhoff material model:

$$W(\mathbf{E}) = \frac{\lambda}{2}\text{tr}(\mathbf{E})^2 + \mu\text{tr}(\mathbf{E}^2), \quad (2.20)$$

the Hencky elasticity model:

$$W(\mathbf{H}) = \frac{\lambda}{2} \text{tr}(\mathbf{H})^2 + \mu \text{tr}(\mathbf{H}^2), \quad (2.21)$$

the compressible Mooney-Rivlin solid:

$$W(I_1, I_2, J) = C_{01}(J^{-4/3}I_2 - 3) + C_{10}(J^{-2/3}I_1 - 3) + D_1(J - 1)^2, \quad (2.22)$$

$$I_1 = \text{tr}(\mathbf{B}), \quad I_2 = \frac{1}{2} [\text{tr}(\mathbf{B})^2 - \text{tr}(\mathbf{B}^2)], \quad J = \det(\mathbf{F}), \quad (2.23)$$

$$D_1 = \frac{\kappa}{2}, \quad (C_{01} + C_{10}) = \frac{\mu}{2}, \quad (2.24)$$

and the compressible Neo-Hookean solid (a special case of the Mooney-Rivlin solid where $C_{01} = 0$, and $C_1 = C_{10}$):

$$W(I_1, J) = C_1(J^{-2/3}I_1 - 3) + D_1(J - 1)^2 \quad (2.25)$$

Cauchy-elasticity (as a terminology to describe a particular sub-class of material models) differs from hyperelasticity in the sense that the relations between particular stress and strain measures are defined directly, and do not necessarily arise from an elastic potential function. The models of linear elasticity, in particular, are generalizations of Hooke's law, namely:

$$\boldsymbol{\sigma} = \mathbf{C} : \boldsymbol{\varepsilon}, \quad (2.26)$$

and are suitable for small deformations, but are typically not applicable in the context of finite deformations. By comparison, Cauchy-elastic models are defined in terms of the deformation gradient \mathbf{F} , i.e.

$$\boldsymbol{\sigma} = f(\mathbf{F}), \quad (2.27)$$

and are suitable in the context of finite deformations. For such models to be considered objective under a superposed rigid rotation corresponding to \mathbf{R} , they must satisfy the following condition:

$$\mathbf{R}\boldsymbol{\sigma}\mathbf{R}^T = f(\mathbf{RF}). \quad (2.28)$$

Nonetheless, such models may still suffer from being non-conservative, in the sense that the total work done by the stresses acting on a body moving through an arbitrary closed

cycle of deformation does not necessarily sum to zero. For these reasons, models of hyperelasticity are generally preferred where the use of such models is deemed appropriate. Nonetheless elasticity models are still useful, particularly in the context of small deformations.

In contrast, hypoelasticity models define an evolution (rate) equation in terms of the current stress and the velocity gradient at a given material point, i.e.

$$\dot{\boldsymbol{\sigma}} = g(\boldsymbol{\sigma}, \mathbf{L}). \quad (2.29)$$

Hypoelasticity models are in general non-conservative, and moreover may not necessarily return to a state of zero stress following a closed cycle of deformation. Hypoelasticity is generally less appropriate where hyperelastic or other elastic models may be used instead. The value of hypoelasticity lies in its ability to accommodate models for plastic flow and dissipation in the material, giving rise to the common models of hypoelasto-plasticity.

One of the primary challenges of working with hypoelastic models concerns the manner in which the rate of stress transforms under superposed rigid-body rotations. These considerations have led to the formulation of co-rotational (or objective) stress rates. A multitude of such rates exist, though only a few are found to be in common usage. Most notably, the Jaumann rate of stress $\dot{\boldsymbol{\sigma}}$ is defined as

$$\dot{\boldsymbol{\sigma}} = g(\boldsymbol{\sigma}, \mathbf{D}) = \dot{\boldsymbol{\sigma}} + \boldsymbol{\sigma} \mathbf{W} - \mathbf{W} \boldsymbol{\sigma}, \quad (2.30)$$

where \mathbf{D} and \mathbf{W} specify the rate of deformation and spin at a given material point, respectively.

2.4 Model Boundary Value Problem

Up to this point, we have discussed only the essential relationships which exist between physical quantities of interest in the context of solid mechanics. Ultimately, however, we should like to determine the anticipated motion and deformation of a particular body under the action of pre-determined externally applied forces. To this end, we must turn our attention to the definition – and solution – of boundary value problems (BVPs). Such problems must be well-posed, in the sense that there exists a unique solution to the stated problem, thereby imposing certain restrictions on the choice of boundary conditions.

The Strong Form Statement of Equilibrium

In the context of solid mechanics, the solution of a given boundary value problem usually refers to a complete description of the primary field variable(s) of interest, namely the displacement field $\mathbf{u}(\mathbf{X})$ at all locations $\mathbf{X} \in \mathcal{B}_0$ within the body \mathcal{B}_0 in its reference configuration. Under the requirements of compatibility, we presume that the displacement field is a continuous function, whose derivatives up to second order are defined everywhere, i.e. $\mathbf{u} \in [C^2(\mathcal{B}_0)]^d$.

Now, let us examine a quasi-static solid mechanics model problem of the following form: consider an open domain $\mathcal{B}_0 \subset \mathbb{R}^d$ whose boundary $\partial\mathcal{B}_0$ consists of the partition $\{\Gamma_0^D, \Gamma_0^N\}$. Let $\mathbf{u} = \bar{\mathbf{u}} \forall \mathbf{X} \in \Gamma_0^D$ constitute a prescribed Dirichlet boundary condition imposed upon the displacement field, and $\mathbf{n} \cdot \boldsymbol{\sigma} = \bar{\mathbf{t}} \forall \mathbf{X} \in \Gamma_0^N$ be a Neumann boundary condition imposed upon the surface traction. Additionally, let us suppose that an applied body force \mathbf{b} acts upon all points $\mathbf{X} \in \mathcal{B}_0$. Given these conditions, we should like to determine the displacement field $\mathbf{u} \in \mathcal{S} = \left\{ \mathbf{u} \in [C^2(\mathcal{B}_0)]^d : \mathbf{u} = \bar{\mathbf{u}} \forall \mathbf{x} \in \Gamma_0^D \right\}$ which satisfies the equations of equilibrium in a point-wise sense:

$$\rho \mathbf{b} + \nabla_x \cdot \boldsymbol{\sigma} = \mathbf{0} \quad \forall \mathbf{x} \in \mathcal{B}_t, \quad (2.31)$$

and where we suppose that a constitutive model has been defined in order to relate some measure of the deformation (e.g. $\mathbf{F} = \mathbf{1} + \nabla_X \mathbf{u}$) to the stress (e.g. $\boldsymbol{\sigma} = f(\mathbf{F})$). Equivalently, we may write the equations of equilibrium in terms of quantities related to the reference configuration of the body:

$$\rho_0 \mathbf{b} + \nabla_X \cdot \mathbf{P}^T = \mathbf{0} \quad \forall \mathbf{X} \in \mathcal{B}_0, \quad (2.32)$$

where $\rho_0 = J\rho$ is the mass density of the material at time $t = 0$. The above statement is commonly referred to as the “strong form” of the model problem, given that it requires a point-wise satisfaction of equilibrium.

It should be emphasized that the Dirichlet boundary conditions and the requirements of compatibility are satisfied implicitly, as a consequence of the deliberate choice of function space \mathcal{S} for the displacement field. Such functions $\mathbf{u} \in \mathcal{S}$ are termed “admissible,” as potential solutions to the boundary value problem at hand.

The Equivalent Weak Form Statement of Equilibrium

In general, solutions to the strong form problem are not easily obtained. For this reason, it proves to be much more convenient to work with the (equivalent) “weak form” statement of the boundary value problem:

Find $\mathbf{u} \in \mathcal{S} = \left\{ \mathbf{u} \in [H^1(\mathcal{B}_0)]^d : \mathbf{u} = \bar{\mathbf{u}} \forall \mathbf{X} \in \Gamma_0^D \right\}$ such that

$$\mathcal{R}(\mathbf{u}, \mathbf{v}) = \int_{\mathcal{B}_t} \rho \mathbf{b} \cdot \mathbf{v} dv + \int_{\Gamma_t^N} \bar{\mathbf{t}} \cdot \mathbf{v} da - \int_{\mathcal{B}_t} \boldsymbol{\sigma} : \nabla_x \mathbf{v} dv = 0 \quad \forall \mathbf{v} \in \mathcal{V}, \quad (2.33)$$

or equivalently

$$\mathcal{R}(\mathbf{u}, \mathbf{v}) = \int_{\mathcal{B}_0} \rho_0 \mathbf{b} \cdot \mathbf{v} dV + \int_{\Gamma_0^N} \bar{\mathbf{p}} \cdot \mathbf{v} dA - \int_{\mathcal{B}_0} \mathbf{P} : \nabla_X \mathbf{v} dV = 0 \quad \forall \mathbf{v} \in \mathcal{V}, \quad (2.34)$$

where $\mathcal{V} = \left\{ \mathbf{v} \in [H^1(\mathcal{B}_0)]^d : \mathbf{v} = \mathbf{0} \forall \mathbf{X} \in \Gamma_0^D \right\}$, and

$$H^1(\mathcal{B}_0) = \left\{ u \in L^2(\mathcal{B}_0), D^\alpha u \in L^2(\mathcal{B}_0) \forall |\alpha| \leq 1 \right\}. \quad (2.35)$$

It should be remarked that the space \mathcal{S} of admissible solutions to the weak form now consists of much more general functions than those considered for the strong form. In other words, the requirements on the differentiability of functions in \mathcal{S} have been “weakened.”

In (2.34), the traction boundary condition has been replaced by $\mathbf{p} = \bar{\mathbf{p}} \forall \mathbf{X} \in \Gamma_0^N$ – i.e. a condition on the Piola (rather than Cauchy) surface traction. The function space \mathcal{S} is commonly referred to as the space of admissible “trial solutions,” whereas \mathcal{V} is called the space of “test functions,” and consists of all admissible variations such that $\mathcal{V} = T_{\mathbf{u}}\mathcal{S}$ is the tangent space to \mathcal{S} (i.e. $\mathbf{u} + \mathbf{v} \in \mathcal{S} \forall \mathbf{u} \in \mathcal{S}, \mathbf{v} \in \mathcal{V}$). In words, our goal is determine the solution \mathbf{u} from among all admissible trial solutions contained in \mathcal{S} which satisfies equation (2.33) or (2.34) for all admissible variations $\mathbf{v} \in \mathcal{V}$.

Under the assumptions of small displacements and linear elasticity, equations (2.33) and (2.34) are equivalent, and may be more succinctly expressed in terms of a bilinear form $a: \mathcal{S} \times \mathcal{V} \mapsto \mathbb{R}$ and a linear form $\ell: \mathcal{V} \mapsto \mathbb{R}$ such that

$$a(\mathbf{u}, \mathbf{v}) + \ell(\mathbf{v}) = 0 \quad \forall \mathbf{v} \in \mathcal{V}. \quad (2.36)$$

2.5 Galerkin Approximations to the Weak Form

In the weak form problem statement, the trial and test spaces \mathcal{S} and \mathcal{V} are taken to be infinite dimensional function spaces. In a practical computational setting, however, this renders the solution of such problems infeasible. Instead, most variational methods consider approximate solutions to the weak form, where $\mathbf{u} \in \mathcal{S}$ and $\mathbf{v} \in \mathcal{V}$ are replaced by $\mathbf{u}^h \in \mathcal{S}^h \subset \mathcal{S}$ and $\mathbf{v}^h \in \mathcal{V}^h \subset \mathcal{V}$, respectively. In this context, $\{\varphi_a\}_{a=1}^N$ and $\{\phi_a\}_{a=1}^M$ denote finite dimensional bases for the sub-spaces \mathcal{S}^h and \mathcal{V}^h , such that

$$\mathbf{u}^h(\mathbf{X}) = \sum_{a=1}^N \varphi_a(\mathbf{X}) \mathbf{u}_a, \quad \mathbf{v}^h(\mathbf{X}) = \sum_{a=1}^M \phi_a(\mathbf{X}) \mathbf{v}_a. \quad (2.37)$$

This yields the Galerkin approximation to the weak form: *Find $\mathbf{u}^h \in \mathcal{S}^h$ such that*

$$\mathcal{R}(\mathbf{u}^h, \mathbf{v}^h) = 0 \quad \forall \mathbf{v}^h \in \mathcal{V}^h, \quad (2.38)$$

yielding the (in general, nonlinear) residual equations, in index notation:

$$R_{ia}(\mathbf{u}^h) = \int_{\mathcal{B}_0} \rho_0 b_i \phi_a \, dV + \int_{\Gamma_0^N} \bar{p}_i \phi_a \, dA - \int_{\mathcal{B}_0} P_{ij} \phi_{a,j} \, dV = 0 \quad \forall i, a. \quad (2.39)$$

Without loss of generality, if we suppose that $\mathcal{S} = \mathcal{V}$ (provided $\mathbf{u} = \mathbf{0} \ \forall \mathbf{X} \in \Gamma_0^D$), then we may select identical sub-spaces $\mathcal{S}^h = \mathcal{V}^h$ ($\{\varphi_a\}_{a=1}^N = \{\phi_a\}_{a=1}^M$), resulting in a symmetric (or Bubnov-) Galerkin method. Traditional finite element methods fall into this category. Such methods are advantageous in the sense that (for linear problems) they result in stable, symmetric bilinear forms satisfying the Galerkin orthogonality (or “best approximation”) property – the property that the solution error $\mathbf{e} = \mathbf{u}^h - \mathbf{u}$ is orthogonal to the chosen sub-space \mathcal{S}^h .

Petrov-Galerkin methods consider the more general case where $\mathcal{V}^h \neq \mathcal{S}^h$, resulting in differing trial and test function spaces. Such methods must guarantee satisfaction of the LBB (inf-sup) conditions to achieve convergence. Consequently, the selection of appropriate trial and test function spaces which result in stable discretizations is not trivial. Nonetheless, Petrov-Galerkin methods allow for greater flexibility in the construction of numerical approximation schemes.

Finite Element Methods

Finite element methods (FEM) are predicated on the idea that a problem domain \mathcal{B}_0 can be discretized into a finite number of simpler sub-domains $\Omega_e \subset \mathcal{B}_0$, individually called elements, and collectively referred to as a “mesh.” The basis functions are assumed to be low-order polynomials within each element, and are compactly supported over a given patch of elements. The traditional finite element method assumes these basis functions to be C^0 continuous at element boundaries, yielding a priori satisfaction of compatibility.

Individual FE basis functions φ_a are typically associated with the “nodes” \mathbf{X}_a of the mesh (located at element vertices, along element edges, etc.), such that the Kronecker delta property is satisfied, i.e. $\varphi_a(\mathbf{X}_b) = \delta_{ab}$. Consequently, the basis functions comprise a set of interpolants for discrete values of the solution defined at the nodes.

Elements consisting of regular shapes (tetrahedra, hexahedra) also provide a natural means of effecting numerical integration of the weak form through the use of the isoparametric transformation and product Gaussian quadrature rules.

Consistent Linearization of the Weak Form

In order to determine the solution $\mathbf{u}^h \in \mathcal{S}^h$ satisfying the weak form equations, we will choose to employ a Newton-Raphson algorithm:

```

Compute initial guess  $u_{jb}^{(0)}$  ;
while  $\|R_{ia}\| < \epsilon$  do
    Assemble  $K_{iajb} = \partial R_{ia} / \partial u_{jb}$  ;
    Update  $u_{jb}^{(k+1)} \leftarrow u_{jb}^{(k)} - K_{jbia}^{-1} R_{ia}$  ;
end
```

Algorithm 1: Newton-Raphson Iteration

Here, R_{ia} denotes the residual (vector), and K_{iajb} denotes the stiffness matrix – the Jacobian of the residual with respect to the independent unknowns u_{jb} (the nodal displacements). The above iteration procedure is repeated until the stopping criterion $\|R_{ia}\| < \epsilon$ is reached, for some specified residual measure $\|\cdot\|$, and tolerance ϵ .

Given the residual equations $R_{ia}(\mathbf{u}^h) = 0 \forall i, a$, we may express their first partial

derivatives $\partial R_{ia}/\partial u_{jb}$ with respect to the independent unknowns u_{jb} as

$$\frac{\partial R_{ia}}{\partial u_{jb}} = \int_{\Gamma_0^N} \frac{\partial \bar{p}_i}{\partial u_{jb}} \phi_a dA - \int_{B_0} \frac{\partial P_{ik}}{\partial u_{jb}} \phi_{a,k} dV, \quad (2.40)$$

indicating two primary terms ($\bar{\mathbf{p}}$ and \mathbf{P}) which must be linearized. Subsequent discussions will focus on the linearization of the first Piola-Kirchhoff stress.

Nonlinear Deformation and Incremental Kinematics

Let us contemplate the linearization of $\partial P_{ik}/\partial u_{jb}$ by applying the chain-rule:

$$\frac{\partial P_{ik}}{\partial u_{jb}} = \frac{\partial P_{ik}}{\partial F_{lm}} \frac{\partial F_{lm}}{\partial u_{jb}}, \quad (2.41)$$

revealing the deformation “gradient operator:”

$$\frac{\partial F_{lm}}{\partial u_{jb}} = \delta_{jl} \varphi_{b,m}. \quad (2.42)$$

If an enhanced strain formulation is employed, only the gradient operator would need to be modified; the subsequent expressions pertaining to $\partial P_{ik}/\partial F_{lm}$ would remain unchanged.

Through further application of the chain-rule, and use of the following identities:

$$\frac{\partial J}{\partial F_{lm}} = J F_{ml}^{-1}, \quad \frac{\partial F_{kj}^{-1}}{\partial F_{lm}} = F_{kl}^{-1} F_{mj}^{-1}, \quad (2.43)$$

one can derive the following result:

$$\frac{\partial P_{ik}}{\partial F_{lm}} = J \sigma_{ij} (F_{ml}^{-1} F_{kj}^{-1} + F_{kl}^{-1} F_{mj}^{-1}) + J \frac{\partial \sigma_{ij}}{\partial F_{lm}} F_{kj}^{-1}. \quad (2.44)$$

If the material model allows for the Cauchy stress to be written directly as a function of the deformation gradient (i.e. $\boldsymbol{\sigma} = f(\mathbf{F})$, as is the case for Cauchy-elastic material models), then a consistent linearization for $\partial \sigma_{ij}/\partial F_{lm}$ may be obtained by direct differentiation.

Otherwise (for hypoelastic material models of the form $\dot{\boldsymbol{\sigma}} = g(\boldsymbol{\sigma}, \mathbf{L})$), we must consider the integral of the stress rate over some finite time interval $\Delta t = t_{k+1} - t_k$:

$$\boldsymbol{\sigma}_{k+1} = \boldsymbol{\sigma}_k + \int_{t_k}^{t_{k+1}} \dot{\boldsymbol{\sigma}} dt. \quad (2.45)$$

The corresponding increment of motion is characterized by $\hat{\mathbf{F}} = \mathbf{F}_{k+1} \mathbf{F}_k^{-1} = \hat{\mathbf{R}} \hat{\mathbf{U}}$, which is used to update the stress via the following incremental algorithm (proposed in [60]):

$$\boldsymbol{\sigma}_{k+1} = \hat{\mathbf{R}} \left[\boldsymbol{\sigma}_k + \int_{t_k}^{t_{k+1}} \dot{\boldsymbol{\sigma}}(\mathbf{D}) dt \right] \hat{\mathbf{R}}^T, \quad (2.46)$$

where $\mathbf{D} = \frac{1}{\Delta t} \log \hat{\mathbf{U}}$ denotes the time-averaged rate of deformation over the time step. The resulting algorithmically consistent tangent $\partial \sigma_{ij} / \partial F_{lm}$ is computed as

$$\frac{\partial \sigma_{ij}}{\partial F_{lm}} = \frac{\partial \hat{R}_{ik}}{\partial F_{lm}} \hat{R}_{nk} \sigma_{nj} + \sigma_{in} \hat{R}_{nk} \frac{\partial \hat{R}_{jk}}{\partial F_{lm}} + \hat{R}_{ik} C_{kn}{}_{pq} \hat{R}_{jn} \frac{\partial D_{pq}}{\partial F_{lm}} \Delta t, \quad (2.47)$$

where $C_{kn}{}_{pq} \equiv \partial \dot{\sigma}_{kn} / \partial D_{pq}$ (the material tangent modulus) is supplied by the constitutive model. The computation of $\partial \hat{R}_{ik} / \partial F_{lm}$ and $\partial D_{pq} / \partial F_{lm}$ may be accurately carried out with the aid of the following expressions:

$$\frac{\partial \hat{D}_{pq}}{\partial \hat{U}_{ij}} = \frac{1}{\Delta t} \sum_{r,s} \hat{Q}_{qr} \hat{Q}_{jr} \mathcal{H}(f, \hat{\lambda}_r, \hat{\lambda}_s) \hat{Q}_{ps} \hat{Q}_{is}; \quad f(\lambda) = \log(\lambda), \quad (2.48)$$

$$\frac{\partial \hat{U}_{ij}}{\partial \hat{B}_{kl}} = \sum_{r,s} \hat{Q}_{jr} \hat{Q}_{lr} \mathcal{H}(g, \hat{\lambda}_r^2, \hat{\lambda}_s^2) \hat{Q}_{is} \hat{Q}_{ks}; \quad g(\lambda) = \sqrt{\lambda}, \quad (2.49)$$

$$\frac{\partial \hat{B}_{kj}}{\partial F_{lm}} = F_{mi}^{-1} (\hat{F}_{ik} \hat{F}_{lj} + \hat{F}_{ij} \hat{F}_{lk}), \quad (2.50)$$

$$\frac{\partial \hat{R}_{ik}}{\partial F_{lm}} = \delta_{il} \hat{R}_{mj} F_{jk}^{-1} - \hat{R}_{in} \frac{\partial \hat{U}_{nj}}{\partial F_{lm}} \hat{U}_{jk}^{-1}, \quad (2.51)$$

where we define

$$\mathcal{H}(f, x, y) \equiv \begin{cases} f'(x), & x = y \\ \frac{f(x) - f(y)}{x - y} & x \neq y \end{cases}, \quad (2.52)$$

and $\hat{\mathbf{U}} = \hat{\mathbf{Q}} \hat{\Lambda} \hat{\mathbf{Q}}^T$ represents the eigendecomposition of $\hat{\mathbf{U}}$, and $\hat{\lambda}_i$ denote the corresponding eigenvalues of $\hat{\mathbf{U}}$.

2.6 Requirements for Convergence of an Approximation Method

Because variational methods utilize finite dimensional spaces \mathcal{S}^h and \mathcal{V}^h , they inherently incur some error $\mathbf{e} = \mathbf{u}^h - \mathbf{u}$ in approximating the exact solution to the original boundary value problem. The approximation power of a given method is typically characterized by the rate at which a specified error measure $\|\mathbf{u}^h - \mathbf{u}\|$ (defined on \mathcal{S}) decreases as the dimension N of the approximation space \mathcal{S}^h is systematically increased. For finite element methods, increasing the dimension N of the approximation space is synonymous with refining the discretization, to the extent that a specified mesh parameter h (the

diameter of the largest element in the mesh) is decreased. An approximation method will therefore yield solutions \mathbf{u}^h which converge to the exact solution \mathbf{u} , provided

$$\lim_{N \rightarrow \infty} \|\mathbf{u}^h - \mathbf{u}\| = \lim_{h \rightarrow 0} \|\mathbf{u}^h - \mathbf{u}\| = 0. \quad (2.53)$$

Further, a method whose solution error can be bounded by an estimate

$$\|\mathbf{u}^h - \mathbf{u}\| \leq Ch^\alpha \|\mathbf{u}\|, \quad (2.54)$$

will converge at a rate of order α .

For an approximation method to achieve convergence, several conditions must be satisfied, namely: approximability, compatibility, stability, and quadrature consistency. These conditions are summarized in the following sections.

Approximability

To achieve α^{th} -order convergence, the approximation space \mathcal{S}^h must contain $[P^k(\mathcal{B}_0)]^d$ (the space of vector-valued polynomial functions of maximal degree $k = \alpha + 1$) as a subset $\mathcal{S}^h \supset [P^k(\mathcal{B}_0)]^d$.

This property is sometimes referred to as *approximability*, reflecting a given method's ability to well-approximate the solution locally as a low-order polynomial. Alternatively, this condition is known as polynomial *reproducibility*, or *completeness*. This condition can be rationalized by the Weierstrass approximation theorem, which asserts that any smooth function can be approximated by polynomials to arbitrary precision.

Compatibility

Compatibility, in an abstract sense, imposes requirements upon the continuity of trial solutions $\mathbf{u}^h \in \mathcal{S}^h$. For conforming finite element methods, this condition is automatically satisfied, as the trial solution space consists of sufficiently continuous functions, such that $\mathcal{S}^h \subset C^0$.

By comparison, non-conforming finite element methods admit more general functions $\mathbf{u}^h \in \mathcal{S}^h \not\subset C^0$. Such spaces of functions must satisfy additional weak compatibility requirements. Namely, Stummel has proposed in [72] the necessary and sufficient conditions

for convergence of a non-conforming finite element method, necessitating passage of the *generalized patch test*:

For a given patch $\mathcal{P} \subset \bar{\mathcal{B}}_0$ and an approximating sequence of functions $u^h \in H^k(\mathcal{B}_0)$: for every $\mathbf{X} \in \mathcal{P}$ there exists an open neighborhood O in \mathbb{R}^d such that

$$\lim_{h \rightarrow 0} \sum_{\forall \Omega_e} \int_{\partial \Omega_e} v D^\alpha u^h|_{\Omega_e} \mathbf{n} da = \mathbf{0} \quad (2.55)$$

for all test functions $v \in C_0^\infty(O)$, and $|\alpha| \leq k - 1$.

Shi later proposed the F-E-M test in [19] as an alternative, sufficient condition for convergence, with a corresponding interface requirement (the F-test):

$$\left| \int_{\Omega_a \cap \Omega_b} [\![u^h]\!] da \right| \leq O(h^{d/2}) \|u^h\|_{\Omega_a \cup \Omega_b} \quad \forall \Omega_a \cap \Omega_b \neq \emptyset. \quad (2.56)$$

Stability

The LBB (inf-sup) conditions (introduced in [5], [13]) pertain to potentially differing choices for \mathcal{S}^h and \mathcal{V}^h with appropriately defined norms. For the model problem with bilinear form $a: \mathcal{S} \times \mathcal{V} \rightarrow \mathbb{R}$, *uniqueness* of a given solution is contingent upon the inf-sup condition:

$$\inf_{\mathbf{u}^h \in \mathcal{S}^h} \sup_{\mathbf{v}^h \in \mathcal{V}^h} \frac{a(\mathbf{u}^h, \mathbf{v}^h)}{\|\mathbf{u}^h\| \|\mathbf{v}^h\|} > 0. \quad (2.57)$$

If a is symmetric and $\mathcal{S}^h = \mathcal{V}^h$, this condition is equivalent to the requirement that a be elliptic (coercive):

$$a(\mathbf{u}^h, \mathbf{u}^h) \geq C_c \|\mathbf{u}^h\|^2 \quad \forall \mathbf{u}^h \in \mathcal{S}^h. \quad (2.58)$$

Existence of a solution further depends upon the condition that a be bounded:

$$a(\mathbf{u}^h, \mathbf{v}^h) \leq C_b \|\mathbf{u}^h\| \|\mathbf{v}^h\| \quad \forall \mathbf{u}^h \in \mathcal{S}^h, \mathbf{v}^h \in \mathcal{V}^h, \quad (2.59)$$

and surjective:

$$\sup_{\mathbf{u}^h \in \mathcal{S}^h} a(\mathbf{u}^h, \mathbf{v}^h) > 0 \quad \forall \mathbf{v}^h \in \mathcal{V}^h. \quad (2.60)$$

Heuristically, these conditions require that individual element stiffness matrices be of full rank, excluding rigid body modes of deformation. This necessitates both: the specification of a stable discretization, and sufficiently accurate evaluation (numerical integration) of the weak form.

Quadrature Consistency

Considering the variational formulation of the model boundary value problem in (2.34), if the exact solution $\mathbf{u} \in \mathcal{S}$ to the weak form is contained within the chosen approximation space (i.e. if $\mathbf{u} \in \mathcal{S}^h$), we require that \mathbf{u} be identified as the unique solution to the Galerkin approximation in (2.38), namely:

$$\mathcal{R}(\mathbf{u}, \mathbf{v}^h) = 0 \quad \forall \mathbf{v}^h \in \mathcal{V}^h. \quad (2.61)$$

This property is referred to as *Galerkin exactness*, and is particularly relevant to the satisfaction of finite element patch tests, which demonstrate Galerkin exactness when the exact solution is a low-order polynomial.

In particular, given a stress field $P_{ij}(\mathbf{u})$ arising from the exact solution $\mathbf{u} \in \mathcal{S}^h$, and for the given boundary conditions $\bar{p}_i = P_{ij}N_j$ and $\rho_0 b_i = -P_{ij,j}$, we may express the residual equations as

$$R_{ia} = \int_{\mathcal{B}_0} P_{ij}\phi_{a,j} dV + \int_{\mathcal{B}_0} P_{ij,j}\phi_a dV - \int_{\partial\mathcal{B}_0} P_{ij}N_j\phi_a dA = 0 \quad \forall i, a. \quad (2.62)$$

If we suppose that the exact solution is well-approximated by low-order polynomials, i.e.

$$u_i(\mathbf{X}) = \sum_{|\alpha|=0}^k a_{i\alpha} \mathbf{X}^\alpha, \quad P_{ij}(\mathbf{X}) = \sum_{|\alpha|=0}^{k-1} b_{ij\alpha} \mathbf{X}^\alpha, \quad (2.63)$$

then the resulting conditions for Galerkin exactness are:

$$\int_{\mathcal{B}_0} \mathbf{X}^\alpha \phi_{a,i} dV + \int_{\mathcal{B}_0} \mathbf{X}_{,i}^\alpha \phi_a dV = \int_{\partial\mathcal{B}_0} \mathbf{X}^\alpha N_i \phi_a dA \quad \forall i, a, |\alpha| \leq k-1. \quad (2.64)$$

The above consistency requirements are required to hold over the problem domain \mathcal{B}_0 as a whole, or equivalently over each individual element domain Ω_e :

$$\int_{\Omega_e} \mathbf{X}^\alpha \phi_{a,i} dV + \int_{\Omega_e} \mathbf{X}_{,i}^\alpha \phi_a dV = \int_{\partial\Omega_e} \mathbf{X}^\alpha N_i \phi_a dA \quad \forall i, a, |\alpha| \leq k-1, \Omega_e \subset \mathcal{B}_0. \quad (2.65)$$

The above conditions are necessary for satisfaction of the Irons patch test up to k^{th} order, provided $\mathcal{S}^h \supset [P^k(\mathcal{B}_0)]^d$. It should be emphasized that these conditions apply specifically to the test functions $\phi_a \in \mathcal{V}^h$.

In most practical situations, however, the integral expressions in (2.38) are evaluated only approximately; numerical quadrature rules are defined on the elements and on their boundaries, such that

$$\int_{\Omega_e} f(\mathbf{X}) dV \approx \sum_{q=1}^{N_{qp}} w_q f(\mathbf{X}_q), \quad \int_{\partial\Omega_e} f(\mathbf{X}) dA \approx \sum_{b=1}^{N_{bp}} w_b f(\mathbf{X}_b). \quad (2.66)$$

This yields a discrete form of (2.65), henceforth referred to as *quadrature consistency*:

$$\sum_{q=1}^{N_{qp}} w_q \left[\mathbf{X}_q^\alpha \phi_{a,i}^{(q)} + \mathbf{X}_{q,i}^\alpha \phi_a^{(q)} \right] = \sum_{b=1}^{N_{bp}} w_b \mathbf{X}_b^\alpha N_i^{(b)} \phi_a^{(b)} \quad \forall i, a, |\alpha| \leq k-1, \Omega_e \subset \mathcal{B}_0. \quad (2.67)$$

These conditions effectively impose a set constraints on the accuracy of the chosen quadrature rules, and/or on the choice of test functions. Failure to satisfy the above conditions results in issues of integration error, and correspondingly, loss of convergence.

Chapter 3

Partitioned Element Methods

This chapter defines a general class of polytopal element formulations referred to as partitioned element methods (PEM). The essential characteristics and mathematical requirements placed upon these methods are formally stated, giving rise to a family of different approaches, for which some formal investigations are conducted in subsequent chapters. Several specific formulations are summarized in detail, and a number of existing methods are herein classified as particular instances of partitioned element methods.

3.1 Overview

Partitioned element methods are finite-element-like methods which approach the task of constructing approximations to an arbitrary polytopal element's nodal shape functions by partitioning the element into sub-domains (quadrature cells). The element partition serves a dual purpose: it is used to establish a composite quadrature rule for the element, and to define a finite dimensional function space, from which the element's shape functions are selected as the solutions to corresponding boundary value problems, defined locally on the element.

Partitioned element methods are motivated by the idea that it is generally easier and more efficient to define complicated functions over arbitrary domains if the functions are defined in a piecewise polynomial fashion over simpler sub-domains. This is precisely the mentality which likewise motivates the finite element method and other related numerical approximation methods.

The PEM is driven by the need for establishing stable and efficient quadrature rules on arbitrary polytopes. Unlike virtual element methods which typically circumvent the use of quadrature altogether, partitioned element methods recognize the necessity of using domain quadrature rules to evaluate nonlinear residual and stiffness contributions. The use of sufficient quadrature also yields a stable integration of the weak form that does not rely upon unphysical stabilization parameters.

In contrast with traditional perspectives, which regard the shape functions as being continuously defined on element domains (i.e. generalized barycentric coordinates), the PEM exploits the fact that the shape functions and their gradients only need to be evaluated at a discrete number of quadrature points. With this in mind, PEM approximation spaces are deliberately constructed around the quadrature cell partition of the element, and consequently resemble finite element approximation spaces.

The resulting approximations to the element's shape functions are altogether subject to the conditions of approximability, compatibility, stability, and quadrature consistency, as discussed in chapter 2. Together, these conditions impose a number of unique requirements upon the element's partition, its corresponding quadrature rules, and the associated cell-based approximation spaces.

In the following sections, an abstract framework for the PEM is established, describing the shape-function boundary value problems defined on an element, and their corresponding approximations. We further enumerate several specific partitioned element methods, and provide an assessment of their potential strengths and weaknesses.

3.2 Definition of Polytopal Element Shape Functions

Consider the structure of an arbitrary polyhedral element $\Omega \subset \mathbb{R}^3$, as depicted in Figure 3.1. The element's boundary $\partial\Omega$ may be subdivided into polygonal faces $F \subset \partial\Omega$, such that each face F is shared entirely with a single adjacent element of the mesh, or with the mesh boundary. In turn, the boundary of each such face F may be subdivided into linear edges $E \subset \partial F$, such that each edge E is shared by exactly one other face of the element. The end-points of each edge are called nodes, denoted V , and may be shared by

multiple edges.

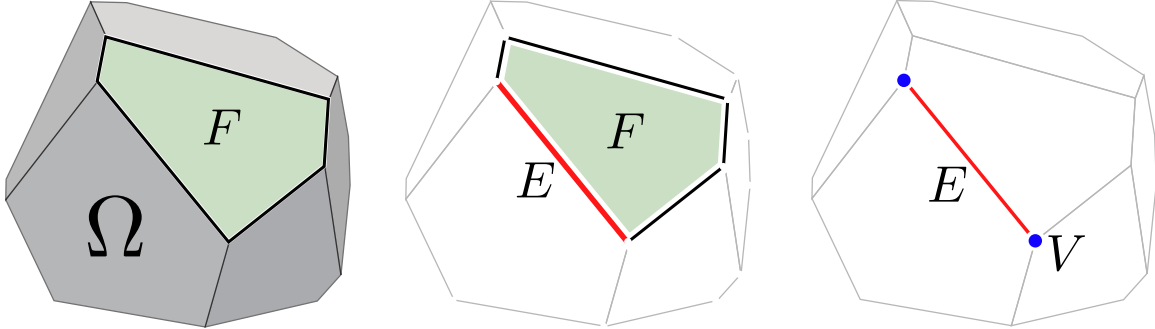


Figure 3.1: A representative polyhedral element $\Omega \subset \mathbb{R}^3$, a polygonal face $F \subset \partial\Omega$, a linear edge $E \subset \partial F$, and a node V .

The function spaces to which the element's shape functions belong are effectively broken Sobolev spaces, where a given shape function $\varphi \in \mathcal{W}_k(\bar{\Omega})$ is defined independently on the open interior of each polyhedral element $\Omega \subset \mathbb{R}^3$, and on its boundary $\partial\Omega$, such that

$$\mathcal{W}_k(\bar{\Omega}) = \left\{ \varphi|_{\Omega} \in H^k(\Omega) : \mathcal{L}_{\Omega}\varphi = f_{\Omega} \text{ in } \Omega, \varphi|_F \in \mathcal{W}_k(\bar{F}) \forall F \in \partial\Omega \right\}, \quad (3.1)$$

$$\mathcal{W}_k(\bar{F}) = \left\{ \varphi|_F \in H^k(F) : \mathcal{L}_F\varphi = f_F \text{ in } F, \varphi|_E \in \mathcal{W}_k(\bar{E}) \forall E \in \partial F \right\}, \quad (3.2)$$

$$\mathcal{W}_k(\bar{E}) = \left\{ \varphi|_E \in H^k(E) : \mathcal{L}_E\varphi = f_E \text{ in } E, \varphi|_V \in \mathbb{R} \forall V \in \partial E \right\}. \quad (3.3)$$

In essence, a given function $\varphi|_{\Omega} \in H^k(\Omega)$ defined on the element's interior is related to a corresponding boundary function $\varphi|_{\partial\Omega} \equiv \bar{\varphi}$ (which itself is a broken $H^k(\partial\Omega)$ function) via a well-posed Dirichlet boundary value problem:

$$\mathcal{L}_{\Omega}\varphi = f_{\Omega} \quad \forall \mathbf{X} \in \Omega \quad \text{s.t.} \quad \varphi = \bar{\varphi} \quad \forall \mathbf{X} \in \partial\Omega, \quad (3.4)$$

where \mathcal{L}_{Ω} denotes a linear differential operator, and $f_{\Omega} \in L^2(\Omega)$ is a generic forcing function. The element's degrees of freedom are collectively accounted for in the boundary function $\bar{\varphi}$, and in the forcing function f_{Ω} . Consequently, the interior function $\varphi|_{\Omega}$ is uniquely defined, provided there exists a unique solution to (3.4). In turn, we suppose that $\varphi|_F \in H^k(F)$ is the solution to a similar (2-dimensional) boundary value problem defined on each face F , and $\varphi|_E \in H^k(E)$ is the solution to a (1-dimensional) BVP on each edge E .

The advantage of defining shape functions in this manner is that it affords a great deal of flexibility in the construction of arbitrary order interpolants (or enhancement functions), while maintaining $C^0(\mathcal{B}_0)$ continuity at inter-element interfaces. Moreover, given that the shape functions are uniquely defined at every point $\mathbf{X} \in \bar{\Omega}$, they can be made amenable to post-processing and visualization-related tasks, if so desired.

Harmonic Shape Functions

The simplest choice of $\mathcal{L}_\Omega = -\nabla^2$ and $f_\Omega = 0$ corresponds to Laplace's equation:

$$\nabla^2 \varphi = 0 \quad \forall \mathbf{X} \in \Omega \quad \text{s.t.} \quad \varphi = \bar{\varphi} \quad \forall \mathbf{X} \in \partial\Omega, \quad (3.5)$$

whose solution φ is harmonic on Ω (and likewise on each face F and edge E – refer to Figure 3.2). Harmonic shape functions form a partition of unity, satisfy linear completeness, and arise from degrees of freedom borne only by the nodes of each element (i.e. the nodal values $\varphi|_V$); therefore, they satisfy the Kronecker delta property. As such, harmonic shape functions constitute a class of generalized barycentric coordinates.

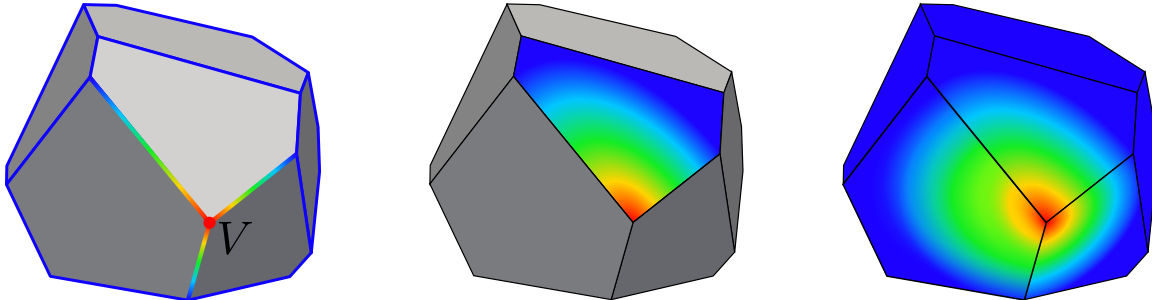


Figure 3.2: The harmonic shape function corresponding to the indicated node V , defined hierarchically on each edge, face, and the element.

If instead $f_\Omega \neq 0$ (corresponding to Poisson's equation), then

$$-\nabla^2 \varphi = f_\Omega \quad \forall \mathbf{X} \in \Omega \quad \text{s.t.} \quad \varphi = \bar{\varphi} \quad \forall \mathbf{X} \in \partial\Omega, \quad (3.6)$$

and we may introduce additional degrees of freedom through f_Ω belonging to the element (or its edges, faces). These degrees of freedom are effectively equivalent to bubble/enrichment functions; they are not directly associated with nodal evaluations of φ , but may be designed to exhibit certain desirable characteristics (e.g. to recover a particular order of polynomial completeness). The corresponding solution to (3.6) is not

harmonic; instead, we shall refer to functions which satisfy (3.6) as *generalized harmonic shape functions*.

Harmonic shape functions are not a new concept; Gordon and Wixom were among the first authors to propose the idea in [38], and Martin et al. later considered their application to polyhedral finite elements in [54]. However, obtaining exact solutions to (3.5) is generally infeasible for arbitrary polyhedra. In practice, approximate solutions must be considered.

In particular, Bishop has proposed a method for constructing FE approximations to harmonic shape functions in [11]. Additionally, the VETFEM ([61], [63]) and the original PEM presented in [62], may be viewed as techniques for obtaining discrete approximations to harmonic shape functions. Likewise, many virtual element methods ([16], [21], [22]) suppose that the element shape functions are harmonic over individual element domains, though they are never explicitly constructed or represented as such.

It herein becomes of interest to determine suitable approximations to harmonic shape functions on arbitrary polyhedra. A number of methods to achieve this end are subsequently discussed.

3.3 Shape Function Approximation Methods

The exact solution $\varphi \in \mathcal{U}(\Omega) = \{\varphi \in H^1(\Omega) : \varphi = \bar{\varphi} \forall \mathbf{X} \in \partial\Omega\}$ to Poisson's equation in (3.6) (or Laplace's equation in (3.5) when $f_\Omega \equiv 0$) also satisfies the equivalent weak form:

$$\int_{\Omega} (\nabla^2 \varphi + f_\Omega) \eta \, dV = 0 \quad \forall \eta \in \mathcal{U}_0(\Omega), \quad (3.7)$$

or

$$\int_{\Omega} \nabla \varphi \cdot \nabla \eta \, dV = \int_{\Omega} f_\Omega \eta \, dV \quad \forall \eta \in \mathcal{U}_0(\Omega), \quad (3.8)$$

where $\mathcal{U}_0(\Omega) = \{\eta \in H^1(\Omega) : \eta = 0 \forall \mathbf{X} \in \partial\Omega\}$ denotes an appropriately defined space of admissible variations.

A vast array of different variational methods may be employed to obtain an approximate solution $\varphi^h \in \mathcal{U}^h(\Omega)$ satisfying

$$\int_{\Omega} \nabla \varphi^h \cdot \nabla \eta^h \, dV = \int_{\Omega} f_\Omega \eta^h \, dV \quad \forall \eta^h \in \mathcal{U}_0^h(\Omega), \quad (3.9)$$

where $\mathcal{U}^h(\Omega)$ and $\mathcal{U}_0^h(\Omega)$ are taken to be finite-dimensional approximation spaces. Consequently, it is of interest to determine the essential requirements placed upon a given approximation φ^h for the purposes of evaluating weak form integrals.

Specifically, for a finite element approximation to the model problem given in (2.36), consider the evaluation of an element's local bilinear form $a_\Omega(\mathbf{u}, \mathbf{v})$, where $\mathbf{u} = \sum_{a=1}^N \varphi_a \mathbf{u}_a$ and $\mathbf{v} = \sum_{a=1}^N \varphi_a \mathbf{v}_a$ are written in terms of the element's shape functions $\{\varphi_a\}_{a=1}^N$. An approximate evaluation of $a_\Omega(\mathbf{u}, \mathbf{v})$ is obtained by making the substitution $a_\Omega(\mathbf{u}^h, \mathbf{v}^h)$, where $\mathbf{u}^h = \sum_{a=1}^N \varphi_a^h \mathbf{u}_a$ and $\mathbf{v}^h = \sum_{a=1}^N \varphi_a^h \mathbf{v}_a$ are instead represented in terms of the approximations $\{\varphi_a^h\}_{a=1}^N$ to the element's shape functions.

According to the virtual element decomposition proposed in [21], we may express a given function $\mathbf{u} = \Pi_k^\Omega \mathbf{u} + (\mathbf{u} - \Pi_k^\Omega \mathbf{u})$ in terms of a low-order polynomial part ($\Pi_k^\Omega \mathbf{u}$) (up to degree k) and a non-polynomial part ($\mathbf{u} - \Pi_k^\Omega \mathbf{u}$), where $\Pi_k^\Omega : L^2(\Omega) \mapsto P^k(\Omega)$ is a corresponding polynomial projection operator satisfying $a_\Omega(\Pi_k^\Omega \mathbf{u}, \mathbf{v} - \Pi_k^\Omega \mathbf{v}) = 0 \quad \forall \mathbf{u}, \mathbf{v}$, and thus

$$a_\Omega(\mathbf{u}, \mathbf{v}) = a_\Omega(\Pi_k^\Omega \mathbf{u}, \Pi_k^\Omega \mathbf{v}) + a_\Omega(\mathbf{u} - \Pi_k^\Omega \mathbf{u}, \mathbf{v} - \Pi_k^\Omega \mathbf{v}). \quad (3.10)$$

The first term appearing in the right-hand side of (3.10) accounts for the consistency of the finite element approximation, whereas the second term provides stability. To maintain consistency, the first term must be computed exactly, to the extent that

$$a_\Omega(\Pi_k^\Omega \mathbf{u}, \Pi_k^\Omega \mathbf{v}) = a_\Omega(\Pi_k^\Omega \mathbf{u}^h, \Pi_k^\Omega \mathbf{v}^h), \quad (3.11)$$

yielding the k -consistency property:

$$a_\Omega(\Pi_k^\Omega \mathbf{u}^h, \mathbf{v}^h) = a_\Omega(\Pi_k^\Omega \mathbf{u}, \mathbf{v}) \quad \forall \mathbf{v} \in \mathcal{V}^h(\Omega). \quad (3.12)$$

However, the second term need only be sufficiently well-approximated by

$$a_\Omega(\mathbf{u} - \Pi_k^\Omega \mathbf{u}, \mathbf{v} - \Pi_k^\Omega \mathbf{v}) \approx a_\Omega(\mathbf{u}^h - \Pi_k^\Omega \mathbf{u}^h, \mathbf{v}^h - \Pi_k^\Omega \mathbf{v}^h), \quad (3.13)$$

to the extent that the correct order of convergence is maintained, and the inf-sup condition is altogether satisfied. In [21], this is characterized by the assertion that there exist two positive constants a_* and a^* which are independent of the chosen discretization, such that

the following stability condition holds:

$$a_* a_\Omega(\mathbf{v}, \mathbf{v}) \leq a_\Omega(\mathbf{v}^h, \mathbf{v}^h) \leq a^* a_\Omega(\mathbf{v}, \mathbf{v}) \quad \forall \mathbf{v} \in \mathcal{V}^h(\Omega). \quad (3.14)$$

It is argued that these conditions are necessary and sufficient to guarantee convergence of the resulting method when the local approximations \mathbf{u}^h and \mathbf{v}^h are used in place of \mathbf{u} and \mathbf{v} .

It should be remarked that the evaluation of $a_\Omega(\mathbf{u}, \mathbf{v})$ will be further approximated through the use of numerical quadrature on Ω , herein denoted as $a_\Omega^h(\mathbf{u}, \mathbf{v})$. Alternatively, the use of low-order quadrature rules may be viewed as an exact integration of corresponding low-order approximations to \mathbf{u} and \mathbf{v} , i.e. $\exists \mathbf{u}^h, \mathbf{v}^h$ such that $a_\Omega^h(\mathbf{u}, \mathbf{v}) = a_\Omega(\mathbf{u}^h, \mathbf{v}^h)$. The use of a numerical quadrature scheme is therefore subject to the conditions previously described.

With the above considerations borne in mind, we propose a set of minimal requirements on the resulting approximations \mathbf{u}^h and \mathbf{v}^h , and their corresponding integration via an appropriately defined quadrature rule:

$$(I) \quad a_\Omega^h(\Pi_k^\Omega \mathbf{u}^h, \mathbf{v}^h) = a_\Omega(\Pi_k^\Omega \mathbf{u}, \mathbf{v}) \quad \forall \mathbf{v} \in \mathcal{V}^h(\Omega).$$

$$(II) \quad a_* a_\Omega(\mathbf{v}, \mathbf{v}) \leq a_\Omega^h(\mathbf{v}^h, \mathbf{v}^h) \leq a^* a_\Omega(\mathbf{v}, \mathbf{v}) \quad \forall \mathbf{v} \in \mathcal{V}^h(\Omega).$$

An important distinction should be made with regard to the requirements placed upon a given variational method used to construct approximations φ^h to (generalized) harmonic shape functions φ : it is not strictly necessary for the approximations to converge to φ as the dimension of $\mathcal{U}^h(\Omega)$ is systematically increased. Provided the above conditions are met, convergence of the overarching finite element method is altogether achieved, even if relatively coarse/low-order approximations to the shape functions are utilized. Moreover, relaxing the requirements placed upon the approximations (particularly with regard to continuity) can have advantageous side-effects: the resulting finite element solution is made less sensitive to the choice of discretization, and poor stiffness matrix conditioning for elements with non-convex or degenerate features can be partially ameliorated. These considerations are investigated further in chapter 5.

The above considerations have prompted an investigation into the use of (discontinuous) low-order polynomial approximations to harmonic shape functions. These approximations are discussed in the following section.

3.4 Non-conforming Galerkin Approximations to (Generalized) Harmonic Shape Functions

If the boundary conditions imposed upon a given shape function are relaxed to the extent that $\varphi^h \neq \bar{\varphi}$ on $\partial\Omega$, then clearly $\mathcal{U}^h(\Omega) \not\subset \mathcal{U}(\Omega)$, and one must resort to the use of non-conforming approximation methods to obtain suitable approximations φ^h . In such cases, the boundary conditions must be imposed in a weak sense, such that φ^h still yields satisfaction of conditions (I) and (II), as developed in the previous section.

A number of weak enforcement strategies for the Dirichlet boundary condition ($\varphi = \bar{\varphi}$ on $\partial\Omega$) are suggested in the following sections.

Weak Enforcement of Boundary Conditions via a Lagrange Multiplier Method

One approach to weakly enforce the boundary condition $\varphi = \bar{\varphi}$ on $\partial\Omega$ would be to consider a Lagrange multiplier method, wherein

$$\min_{\varphi, \lambda} \mathcal{L}(\varphi, \lambda), \quad (3.15)$$

$$\mathcal{L}(\varphi, \lambda) \equiv \frac{1}{2} \int_{\Omega} \nabla \varphi \cdot \nabla \varphi \, dV - \int_{\Omega} f_{\Omega} \varphi \, dV + \int_{\partial\Omega} [\varphi - \bar{\varphi}] \lambda \, dA, \quad (3.16)$$

involving the specification of a Lagrange multiplier field $\lambda \in \Lambda(\partial\Omega) = \{\lambda \in L^2(\partial\Omega)\}$, and its corresponding discrete approximation $\lambda^h \in \Lambda^h(\partial\Omega) \subset \Lambda(\partial\Omega)$. Differentiation of the Lagrangian yields two sets of equations in terms of the approximations $\varphi^h \in \mathcal{U}^h(\Omega)$ and $\lambda^h \in \Lambda^h(\partial\Omega)$:

$$\int_{\Omega} \nabla \varphi^h \cdot \nabla \eta^h \, dV - \int_{\Omega} f_{\Omega} \eta^h \, dV + \int_{\partial\Omega} \lambda^h \eta^h \, dA = 0 \quad \forall \eta^h \in \mathcal{U}^h(\Omega), \quad (3.17)$$

$$\int_{\partial\Omega} (\varphi^h - \bar{\varphi}) \mu^h \, dA = 0 \quad \forall \mu^h \in \Lambda^h(\partial\Omega). \quad (3.18)$$

Suppose finite-dimensional bases are established for $\mathcal{U}^h(\Omega)$ and $\Lambda^h(\partial\Omega)$, i.e.

$$\varphi^h(\mathbf{X}) = \sum_{a=1}^N \psi_a(\mathbf{X}) \varphi_a, \quad \lambda^h(\mathbf{X}) = \sum_{a=1}^M \chi_a(\mathbf{X}) \lambda_a, \quad (3.19)$$

such that

$$\sum_{a=1}^N \left[\int_{\Omega} \nabla \psi_a \cdot \nabla \psi_b dV \right] \varphi_a + \sum_{c=1}^M \left[\int_{\partial\Omega} \psi_b \chi_c dA \right] \lambda_c = \int_{\partial\Omega} f_{\Omega} \psi_b dA \quad \forall b, \quad (3.20)$$

$$\sum_{b=1}^N \left[\int_{\partial\Omega} \chi_c \psi_b dA \right] \varphi_b = \int_{\partial\Omega} \bar{\varphi} \chi_c dA \quad \forall c. \quad (3.21)$$

Given an appropriate selection for the indicated bases, the determination of the unknowns (φ_a and λ_a) entails the solution of a saddle-point system of equations, written in matrix-vector format:

$$\begin{bmatrix} \mathbf{A} & \mathbf{B} \\ \mathbf{B}^T & \mathbf{0} \end{bmatrix} \begin{Bmatrix} \boldsymbol{\varphi} \\ \boldsymbol{\lambda} \end{Bmatrix} = \begin{Bmatrix} \mathbf{f} \\ \bar{\boldsymbol{\varphi}} \end{Bmatrix}, \quad (3.22)$$

where

$$A_{ab} = \int_{\Omega} \nabla \psi_a \cdot \nabla \psi_b dV, \quad B_{bc} = \int_{\partial\Omega} \psi_b \chi_c dA, \quad (3.23)$$

$$f_b = \int_{\partial\Omega} f_{\Omega} \psi_b dA, \quad \bar{\varphi}_c = \int_{\partial\Omega} \bar{\varphi} \chi_c dA. \quad (3.24)$$

The main advantage of this approach is that virtually any space of functions may be selected for $\mathcal{U}^h(\Omega)$, such that the resulting approximations $\varphi^h \in \mathcal{U}^h(\Omega)$ can be made less sensitive to degenerate geometric features of the element (namely, short edges).

Arguably the simplest (and most efficient) choice is $\mathcal{U}^h(\Omega) = P^m(\Omega)$ where $m \geq k$, resembling certain formulations of the VETFEM ([61], [63]), where the basis functions for the Lagrange multiplier field are Dirac delta functions $\chi_c(\mathbf{X}) = \delta(\mathbf{X} - \mathbf{X}_c) \forall c = 1, \dots, N_v$ associated with the individual nodes of the element. A potential shortcoming of this particular choice for χ_c is that the resulting shape functions may nonetheless possess sharp gradients in the vicinity of short element edges, leading to undesirable behavior – poor numerical conditioning of the element's local stiffness matrix.

Various other choices for the Lagrange multiplier basis are possible which may yield less spurious approximations (for instance $\Lambda^h(\partial\Omega) = P^m(\partial\Omega)$). However, careful attention

must be paid to the selection of $\mathcal{U}^h(\Omega)$ and $\Lambda^h(\partial\Omega)$, as poorly chosen bases can lead to ill-posedness of the saddle-point problem. More sophisticated linear solution methodologies may be required in these cases.

Weak Enforcement of Boundary Conditions via Nitsche's Method

As a viable alternative to the Lagrange multiplier method presented in the previous section, the boundary conditions may be enforced weakly via Nitsche's method:

$$\begin{aligned} & \int_{\Omega} \nabla \varphi^h \cdot \nabla \eta^h dV + \int_{\partial\Omega} \left[\epsilon \frac{\partial \eta^h}{\partial N} \varphi^h - \eta^h \frac{\partial \varphi^h}{\partial N} \right] dA + \frac{\alpha}{|\partial\Omega|^\beta} \int_{\partial\Omega} \varphi^h \eta^h dA \\ &= \int_{\Omega} f_\Omega \eta^h dV + \epsilon \int_{\partial\Omega} \frac{\partial \eta^h}{\partial N} \bar{\varphi} dA + \frac{\alpha}{|\partial\Omega|^\beta} \int_{\partial\Omega} \bar{\varphi} \eta^h dA \quad \forall \eta^h \in \mathcal{U}^h(\Omega), \end{aligned} \quad (3.25)$$

where $\alpha > 0$ is a stabilization parameter, $|\partial\Omega|$ denotes the surface area of $\partial\Omega$, and $\beta = (d-1)^{-1}$ for $\Omega \subset \mathbb{R}^d$, $d \geq 2$. The symmetric form of Nitsche's method [47] corresponds to the case where $\epsilon = -1$, whereas the nonsymmetric form ([34], [14]) corresponds to $\epsilon = +1$.

Provided the stabilization parameter α is specified appropriately, the Galerkin approximation φ^h can be obtained as the solution to a positive-definite system of equations: $\mathbf{A}\varphi = \mathbf{f}$, where

$$A_{ab} = \int_{\Omega} \nabla \psi_a \cdot \nabla \psi_b dV + \int_{\partial\Omega} \left[\epsilon \frac{\partial \psi_b}{\partial N} \psi_a - \psi_b \frac{\partial \psi_a}{\partial N} \right] dA + \frac{\alpha}{|\partial\Omega|^\beta} \int_{\partial\Omega} \psi_a \psi_b dA, \quad (3.26)$$

$$f_b = \int_{\Omega} f_\Omega \psi_b dV + \epsilon \int_{\partial\Omega} \frac{\partial \psi_b}{\partial N} \bar{\varphi} dA + \frac{\alpha}{|\partial\Omega|^\beta} \int_{\partial\Omega} \bar{\varphi} \psi_b dA. \quad (3.27)$$

As discussed in the previous section, a rather natural choice for the space of approximating functions is $\mathcal{U}^h(\Omega) = P^m(\Omega)$ with $m \geq k$. The resulting method yields reasonably well-conditioned stiffness matrices for convex shapes, even when the elements possess degenerate edges. However, experimental evidence suggests that for non-convex shapes, the resulting shape function approximations may succumb to Runge's phenomenon, yielding highly oscillatory approximations. A more thorough investigation of this behavior is presented in chapter 5.

These observations have led to the conclusion that approximations consisting of piecewise polynomials may yield more well-behaved (less oscillatory) solutions for φ^h . The remainder of our discussion will focus upon such methods.

3.5 Piecewise Polynomial Approximations to (Generalized) Harmonic Shape Functions

Partitioned element methods consider the approximation to a given element's shape functions via piecewise polynomials defined over a partition of the element's domain. In this regard, the approach proposed by Bishop in [11] is properly regarded as a partitioned element method which utilizes C^0 FE approximations to harmonic shape functions. In like fashion, the eponymous partitioned element method introduced in [62] utilizes weakly continuous piecewise polynomial approximations to harmonic shape functions. Herein we propose a novel alternative approach based upon the interior penalty discontinuous Galerkin finite element method (henceforth, the DG-PEM).

A few preliminary definitions regarding the element's partition are given, followed by a more thorough discussion of several partition-based approximation methods.

The Element Partition

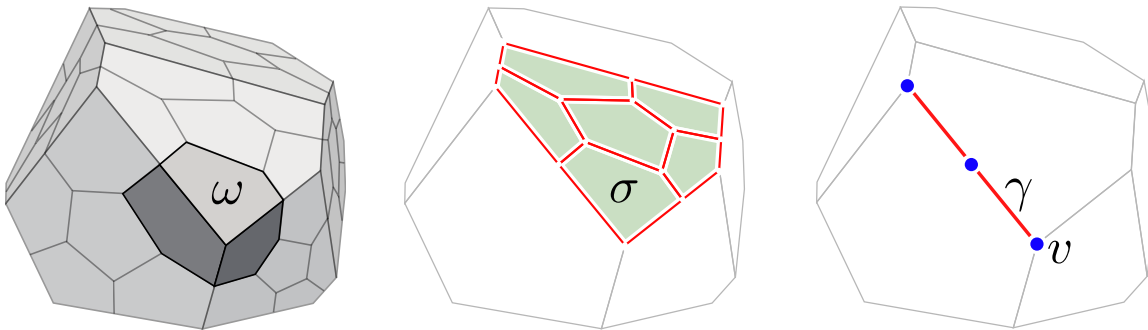


Figure 3.3: A representative polyhedral element $\Omega \subset \mathbb{R}^3$, and its hierarchical partition into cells, facets, segments, and vertices.

Consider a partition $\mathcal{T}_\omega(\Omega)$ of a given polyhedral element Ω into polyhedral cells $\omega \subset \Omega$. The boundary of each cell consists of polygonal facets $\sigma \subset \partial\omega$. Further, denote by Γ_ω the set of all interior cell interfaces (facets) shared by two adjacent cells, such that a given polygonal facet σ belongs either to Γ_ω , or to the boundary of the element $\partial\Omega$.

In turn, let $\mathcal{T}_\sigma(F)$ denote the partition of a given face $F \subset \partial\Omega$ into polygonal facets $\sigma \subset F$. The boundary of each facet consists of linear segments $\gamma \subset \partial\sigma$. For a given face F , let Γ_σ denote the set of all interior facet interfaces (segments) shared by two facets

belonging to F , such that a given linear segment γ belongs either to Γ_σ or ∂F .

Finally, $\mathcal{T}_\gamma(E)$ denotes the partition of a given edge $E \subset \partial F$ into linear segments $\gamma \subset E$. The endpoints of each segment are called vertices, denoted v . For a given edge E , denote by Γ_γ the set of all interior segment interfaces (vertices) shared by two segments belonging to E , such that a given vertex v belongs either to Γ_γ or ∂E . As well, each node V corresponds to a single vertex v , though not all vertices coincide with a node.

A number of simple partitioning schemes are proposed, and illustrated in Figure 3.4:

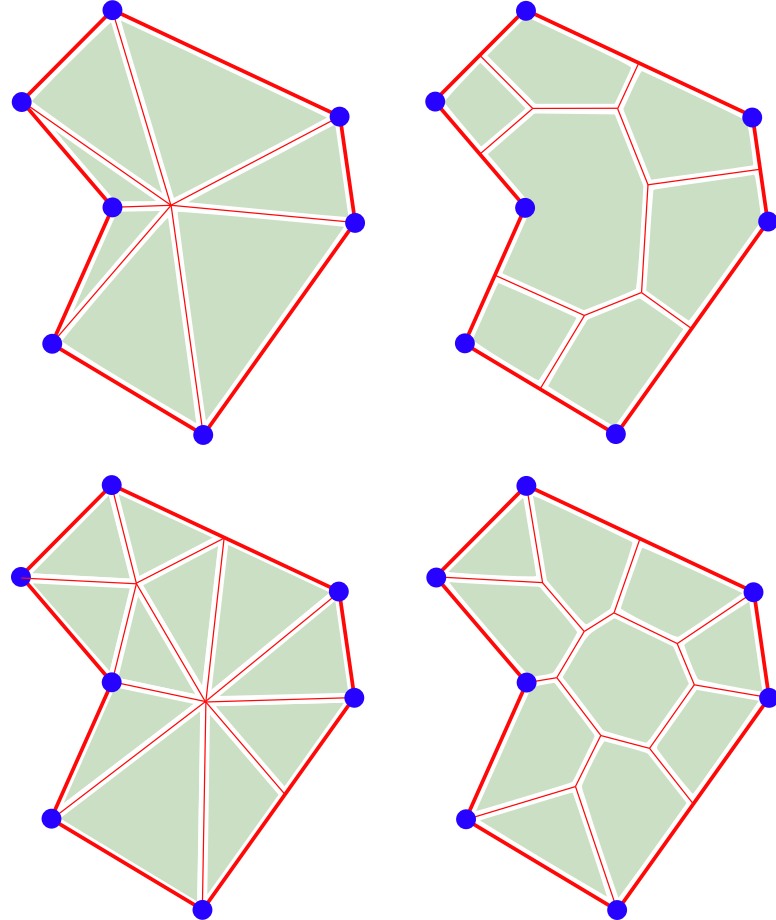


Figure 3.4: Polygonal element partitioning schemes: (top-left) edge-based partition, (top-right) node-based partition, (bottom-left) random Delaunay partition, (bottom-right) random Voronoi partition.

- **Edge-based:** For star-convex shapes – the vertex-averaged centroid is used to subdivide the element into triangles (in 2D) or tetrahedra (in 3D) associated with each linear edge of the element.

- **Node-based:** For arbitrary shapes – the element is sub-divided into quadrature cells corresponding to tributary regions surrounding each node.
- **Random Delaunay:** For arbitrary shapes – the element is sub-divided into a Delaunay triangulation (in 2D) or tetrahedralization (in 3D), whose corresponding vertices are generated via a random point sampling process.
- **Random Voronoi:** For arbitrary shapes – the element is sub-divided into Voronoi cells, whose corresponding voronoi sites are generated via a constrained maximal Poisson-disk sampling process, as described in [27].

We denote the volume of a given cell as $|\omega|$, the area of a facet as $|\sigma|$, and the length of a segment as $|\gamma|$. Each facet likewise possesses an associated normal direction \mathbf{N}_σ , whose orientation is outward from Ω for all $\sigma \in \partial\Omega$. For all $\sigma \in \Gamma_\omega$ shared by two cells (ω_1 and ω_2), the orientation of \mathbf{N}_σ is outward with respect to ω_1 .

Continuous Galerkin Approximations to (Generalized) Harmonic Shape Functions

Consider finite dimensional sub-spaces $\mathcal{U}^h(\Omega) \subset \mathcal{U}(\Omega)$ and $\mathcal{U}_0^h(\Omega) \subset \mathcal{U}_0(\Omega)$. The continuous Galerkin approximation $\varphi^h \in \mathcal{U}^h(\Omega)$ to a given (generalized) harmonic shape function $\varphi \in \mathcal{U}(\Omega)$ satisfies

$$\int_{\Omega} \nabla \varphi^h \cdot \nabla \eta^h dV = \int_{\Omega} f_{\Omega} \eta^h dV \quad \forall \eta^h \in \mathcal{U}_0^h(\Omega). \quad (3.28)$$

Bishop has already explored such an approach in [11] for constructing approximations to harmonic shape functions using a partition of a given polyhedral element into sub-dividing tetrahedra. The approximation space $\mathcal{U}^h(\Omega)$ is spanned by $C^0(\Omega)$ finite element basis functions defined on the tetrahedral partition of Ω . The corresponding shape function approximations $\varphi^h \in \mathcal{U}^h(\Omega)$ are obtained as the solutions to a set of local finite element problems defined on Ω (and its faces, edges – refer to Figure 3.5). This approach will be distinguished as the *continuous Galerkin partitioned element method* (CG-PEM).

It was demonstrated in [11] that the resulting approximations φ^h preserve low-order polynomial completeness – a direct consequence of $\mathcal{U}^h(\Omega) \supset P^1(\Omega)$. If the elements are

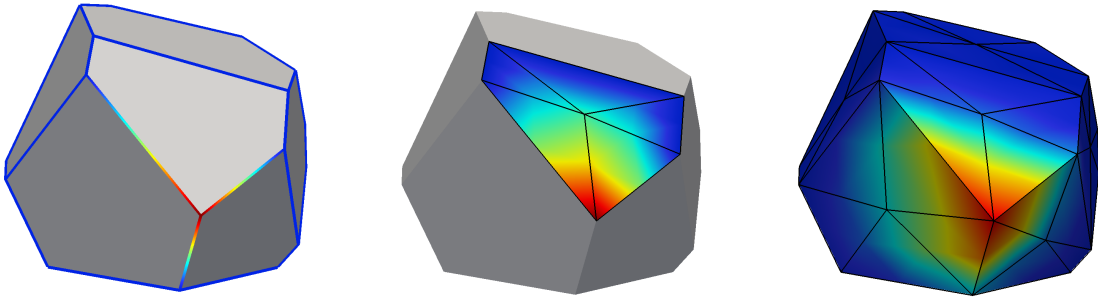


Figure 3.5: The CG-PEM approximation to a given harmonic shape function, defined hierarchically on the element’s faces and edges.

discretized into a sufficient number of tetrahedra, the method is observed to be stable. If sufficiently accurate quadrature rules are specified on Ω and $\partial\Omega$, the CG-PEM also yields a consistent integration of the weak form.

For coarse tetrahedral sub-divisions, the local FE problems that must be solved on each element are relatively small, in some cases entailing only a single degree of freedom. However, the approach can become computationally expensive if the elements are subdivided into an excessively large number of tetrahedra (in the event that more accurate/refined approximations to the shape functions are desired). Initial numerical investigations conducted by Bishop have suggested that relatively coarse tetrahedral sub-divisions of the elements provide sufficiently accurate results; further subdivision (tetrahedral h -refinement) does little to improve the overall accuracy of the method.

A natural extension of the method to higher-order serendipity elements would be to consider p -refinement of an element’s tetrahedral subdivision to recover higher-order polynomial completeness, i.e. to guarantee $\mathcal{U}^h(\Omega) \supset P^k(\Omega)$ for some desired polynomial order k . The construction of shape functions on a given element would likely bear a much higher computational cost with increasing polynomial degree, owing to the increased size of the local FE problems on Ω . Moreover, the specification of efficient yet stable and accurate numerical quadratures would present an additional challenge.

The notion of subdividing the elements into conforming finite elements presents an obvious complication, however. The primary obstacle for traditional finite element methods is the process of obtaining a mesh. Requiring that the elements be partitioned into

canonical finite elements does not obviate the meshing problem; it only defers the problem to the element formulation. Moreover, obtaining an FE partition for an arbitrary polyhedral element presents similar challenges to meshing a complicated problem domain. A separate generalization would be to consider subdividing the elements into arbitrary polyhedra, solving (3.28) by means of the virtual element method. This would allow for a more natural collocation of quadrature cells with the specified subdivision, resembling the partitioned element method proposed in [62].

As will be discussed in chapter 5, a particular complication arises for harmonic shape functions and their corresponding $C^0(\Omega)$ approximations on irregularly shaped elements: the solution to Laplace's equation may possess extremely sharp gradients if the geometry of the element contains reflex corners or nearly degenerate features (i.e. short edges). A consequence of this is poor conditioning of the element's local stiffness matrix, leading to excessively stiff modes of deformation (locking), and issues of numerical conditioning in the linear solution process.

Integration Consistency of the CG-PEM

Consider the case when (3.7) is integrated against an arbitrary polynomial test function $\eta \in P^k(\Omega)$. Integrating by parts yields:

$$\int_{\Omega} \nabla \varphi \cdot \nabla \eta \, dV = \int_{\Omega} f_{\Omega} \eta \, dV + \int_{\Omega} \nabla \cdot (\eta \nabla \varphi) \, dV \quad \forall \eta \in P^k(\Omega). \quad (3.29)$$

Note that

$$\int_{\Omega} \nabla \varphi \cdot \nabla \eta \, dV = \int_{\Omega} [\nabla \cdot (\varphi \nabla \eta) - \varphi \nabla^2 \eta] \, dV \quad \forall \eta \in P^k(\Omega), \quad (3.30)$$

and

$$\int_{\partial\Omega} (\mathbf{N} \cdot \nabla \eta) \bar{\varphi} \, dA = \int_{\Omega} [\nabla^2 \eta \varphi + f_{\Omega} \eta] \, dV + \int_{\Omega} \nabla \cdot (\eta \nabla \varphi) \, dV \quad \forall \eta \in P^k(\Omega). \quad (3.31)$$

For the case where $\eta \in P^1(\Omega)$, we have $\nabla^2 \eta = 0 \quad \forall \eta \in P^1(\Omega)$. Additionally, noting that $\nabla \cdot (\eta \nabla \varphi) = \nabla \eta \cdot \nabla \varphi + \eta \nabla^2 \varphi$, we observe:

$$\int_{\Omega} \nabla \eta \cdot \nabla \varphi \, dV - \int_{\partial\Omega} (\mathbf{N} \cdot \nabla \eta) \bar{\varphi} \, dA = \int_{\Omega} (\nabla^2 \varphi + f_{\Omega}) \eta \, dV = 0 \quad \forall \eta \in P^1(\Omega). \quad (3.32)$$

Further, consider a low-order finite element approximation space $\mathcal{U}^h(\Omega) \supset P^1(\Omega)$ defined on a corresponding partition $\mathcal{T}_\omega(\Omega)$ of Ω . If $\varphi^h \in \mathcal{U}^h(\Omega) \subset \mathcal{U}(\Omega)$ consists of piecewise linear polynomials in each cell $\omega \in \mathcal{T}_\omega(\Omega)$, then $\nabla^2 \varphi^h|_\omega = 0$. Provided $f_\Omega \equiv 0$, the above expression implies that the approximate solution $\varphi^h \in \mathcal{U}^h(\Omega) \subset \mathcal{U}(\Omega)$ to (3.28) will satisfy the first-order integration consistency conditions:

$$\int_{\Omega} \nabla \varphi^h dV = \int_{\partial\Omega} \mathbf{N} \bar{\varphi} dA. \quad (3.33)$$

If (3.33) is integrated exactly by the element's quadrature rules, the resulting CG-PEM elements will pass linear finite element patch tests. If the element's partition consists of linear triangles and tetrahedra, a composite mid-point quadrature scheme proves to be sufficient to this end.

Discontinuous Galerkin Approximations to (Generalized) Harmonic Shape Functions

Consider the broken Sobolev space $\mathcal{D}_k^h(\Omega) = \{\varphi \in L^2(\Omega) : \varphi|_\omega \in P^k(\omega) \forall \omega \in \mathcal{T}_\omega(\Omega)\}$ consisting of (discontinuous) piecewise polynomials defined over the partition of the element. Herein, the family of interior penalty discontinuous Galerkin methods described in [65] are applied to (3.8). In doing so, one obtains piecewise discontinuous approximations to generalized harmonic shape functions $\varphi^h \in \mathcal{D}_k^h(\Omega) \not\subset \mathcal{U}(\Omega)$. The reader is cautioned against several apparent errors in the presentation of interior penalty DG methods found in [65]. The following weak form is consistent with [66]:

$$\begin{aligned} & \sum_{\omega \in \mathcal{T}_\omega(\Omega)} \int_{\omega} \nabla \varphi^h \cdot \nabla \eta^h dV + \sum_{\sigma \in \Gamma_\omega \cup \partial\Omega} \int_{\sigma} \left(\epsilon \left\{ \frac{\partial \eta^h}{\partial N_\sigma} \right\} [\![\varphi^h]\!] - [\![\eta^h]\!] \left\{ \frac{\partial \varphi^h}{\partial N_\sigma} \right\} \right) dA \\ & + J_0(\varphi^h, \eta^h) + J_1(\varphi^h, \eta^h) = \int_{\Omega} f_\Omega \eta^h dV + \sum_{\sigma \in \partial\Omega} \int_{\sigma} \left(\frac{\alpha_{\sigma 0}}{|\sigma|^{\beta_0}} \eta^h + \epsilon \frac{\partial \eta^h}{\partial N_\sigma} \right) \bar{\varphi} dA \end{aligned} \quad (3.34)$$

for all $\eta^h \in \mathcal{D}_k^h(\Omega)$, where

$$\{\varphi\} = \frac{1}{2}(\varphi|_{\omega_1} + \varphi|_{\omega_2}), \quad [\![\varphi]\!] = (\varphi|_{\omega_1} - \varphi|_{\omega_2}) \quad \forall \sigma = \partial\omega_1 \cap \partial\omega_2, \quad (3.35)$$

$$\{\varphi\} = [\![\varphi]\!] = \varphi|_\omega \quad \forall \sigma = \partial\omega \cap \partial\Omega, \quad (3.36)$$

The supplementary bilinear forms $J_0(\varphi^h, \eta^h)$ and $J_1(\varphi^h, \eta^h)$ are defined as:

$$J_0(\varphi^h, \eta^h) = \sum_{\sigma \in \Gamma_\omega \cup \partial\Omega} \frac{\alpha_{\sigma 0}}{|\sigma|^{\beta_0}} \int_{\sigma} [\![\varphi^h]\!] [\!\![\eta^h]\!] dA, \quad (3.37)$$

$$J_1(\varphi^h, \eta^h) = \sum_{\sigma \in \Gamma_\omega} \frac{\alpha_{\sigma 1}}{|\sigma|^{\beta_1}} \int_{\sigma} \left[\left[\frac{\partial \varphi^h}{\partial N_\sigma} \right] \right] \left[\left[\frac{\partial \eta^h}{\partial N_\sigma} \right] \right] dA. \quad (3.38)$$

These two terms penalize jumps in the indicated functions' values and their normal derivatives at cell boundaries, respectively. The parameters $\alpha_{\sigma 0}$, β_0 , must be appropriately specified such that $\alpha_{\sigma 0} > 0$ is sufficiently large, and $\beta_0(d - 1) \geq 1$ where $\Omega \subset \mathbb{R}^d$, $d \geq 2$; the specification of $\alpha_{\sigma 1}$, β_1 is less strict, allowing for $\alpha_{\sigma 1} \geq 0 \forall \sigma$. The parameter $\epsilon \in \{-1, 0, +1\}$ determines which interior penalty method is employed:

$\epsilon = -1$: The symmetric interior penalty Galerkin (SIPG) method.

$\epsilon = 0$: The incomplete interior penalty Galerkin (IIPG) method.

$\epsilon = +1$: The nonsymmetric interior penalty Galerkin (NIPG) method. The NIPG method also encompasses the special case where $\alpha_{\sigma 0} = \alpha_{\sigma 1} = 0$, corresponding to the OBB method [58].

Henceforth, the above methods will collectively be referred to as *discontinuous Galerkin partitioned element methods* (DG-PEM).

If one considers a non-dimensional analysis where $\mathbf{X} = h_\Omega \mathbf{X}'$, and h_Ω denotes a characteristic length scale corresponding to the diameter of the element Ω , the following quantities may be expressed in terms of their non-dimensional counterparts:

$$dV = h_\Omega^d dV', \quad dA = h_\Omega^{d-1} dA', \quad \nabla = h_\Omega^{-1} \nabla', \quad |\sigma| = h_\Omega^{d-1} |\sigma'|, \quad f_\Omega = h_\Omega^{-2} f_{\Omega'}. \quad (3.39)$$

It is presumed that $\alpha_{\sigma 0}$, $\alpha_{\sigma 1}$ are defined independently of h_Ω . Consequently,

$$\begin{aligned}
& h_\Omega^{d-2} \left[\sum_{\omega' \in \mathcal{T}_{\omega'}(\Omega')} \int_{\omega'} \nabla' \varphi^h \cdot \nabla' \eta^h dV' - \int_{\Omega'} f_{\Omega'} \eta^h dV' - \sum_{\sigma' \in \partial\Omega'} \int_{\sigma'} \epsilon \frac{\partial \eta^h}{\partial N_{\sigma'}} \bar{\varphi} dA' \right. \\
& \quad \left. + \sum_{\sigma' \in \Gamma_{\omega'} \cup \partial\Omega'} \int_{\sigma'} \left(\epsilon \left\{ \frac{\partial \eta^h}{\partial N_{\sigma'}} \right\} [\![\varphi^h]\!] - [\![\eta^h]\!] \left\{ \frac{\partial \varphi^h}{\partial N_{\sigma'}} \right\} \right) dA' \right] \\
& + h_\Omega^{(d-1)(1-\beta_0)} \left[\sum_{\sigma' \in \Gamma_{\omega'} \cup \partial\Omega'} \frac{\alpha_{\sigma 0}}{|\sigma'|^{\beta_0}} \int_{\sigma'} [\![\varphi^h]\!] [\![\eta^h]\!] dA' - \sum_{\sigma' \in \partial\Omega'} \frac{\alpha_{\sigma 0}}{|\sigma'|^{\beta_0}} \int_{\sigma'} \eta^h \bar{\varphi} dA' \right] \\
& + h_\Omega^{(d-1)(1-\beta_1)-2} \left[\sum_{\sigma' \in \Gamma_{\omega'}} \frac{\alpha_{\sigma 1}}{|\sigma'|^{\beta_1}} \int_{\sigma'} \left[\left[\frac{\partial \varphi^h}{\partial N_{\sigma'}} \right] \right] \left[\left[\frac{\partial \eta^h}{\partial N_{\sigma'}} \right] \right] dA' \right] = 0 \quad \forall \eta^h \in \mathcal{D}_k^h(\Omega). \quad (3.40)
\end{aligned}$$

To maintain dimensional consistency, it is suggested that β_0 and β_1 be chosen such that

$$\beta_0 = (d-1)^{-1}, \quad \beta_1 = -(d-1)^{-1}. \quad (3.41)$$

To ensure that the resulting linear system of equations is reasonably well-conditioned, the penalty parameters $\alpha_{\sigma 0}$, $\alpha_{\sigma 1}$ should not be made excessively large. Nonetheless, an interesting limiting case occurs when $\alpha_{\sigma 0}, \alpha_{\sigma 1} \rightarrow \infty$ proportionally:

$$J_0(\varphi^h, \eta^h) + J_1(\varphi^h, \eta^h) = \sum_{\sigma \in \partial\Omega} \frac{\alpha_{\sigma 0}}{|\sigma|^{\beta_0}} \int_{\sigma} \eta^h \bar{\varphi} dA \quad \forall \eta^h \in \mathcal{D}_k^h(\Omega). \quad (3.42)$$

The above is henceforth referred to as the *pure penalty* DG-PEM. Under certain conditions (for particular choices of $\mathcal{T}_\omega(\Omega)$ and $\mathcal{D}_k^h(\Omega)$), the pure penalty variant of the DG-PEM may in fact yield unique solutions φ^h which altogether satisfy the conditions of consistency and stability detailed in section 3.3. However, the bilinear form arising from the penalty terms J_0 and J_1 alone is not guaranteed to be elliptic, in general. Additional penalty terms may be necessary, i.e.

$$J_s(\varphi^h, \eta^h) = \sum_{\sigma \in \Gamma_\omega} \frac{\alpha_{\sigma s}}{|\sigma|^{\beta_s}} \int_{\sigma} \left[\left[\frac{\partial^s \varphi^h}{\partial N_{\sigma}^s} \right] \right] \left[\left[\frac{\partial^s \eta^h}{\partial N_{\sigma}^s} \right] \right] dA \quad (3.43)$$

for $s \leq k$, $\alpha_{\sigma s} > 0$, and $\beta_s = (1-2s)/(d-1)$. These may be used to supplement the stability of the pure penalty approach, particularly when $k > 1$.

Integration Consistency of the DG-PEM

Consider the variational form of the DG-PEM in (3.34), specifically for the case when $\eta \in P^k(\Omega) \subset \mathcal{D}_k^h(\Omega)$:

$$\begin{aligned} & \sum_{\omega \in \mathcal{T}_\omega(\Omega)} \int_\omega \nabla \varphi^h \cdot \nabla \eta \, dV + \sum_{\sigma \in \Gamma_\omega \cup \partial\Omega} \int_\sigma \epsilon \frac{\partial \eta}{\partial N_\sigma} [\varphi^h] \, dA + \sum_{\sigma \in \partial\Omega} \frac{\alpha_{\sigma 0}}{|\sigma|^{\beta_0}} \int_\sigma \eta (\varphi^h - \bar{\varphi}) \, dA \\ &= \int_\Omega f_\Omega \eta \, dV + \sum_{\sigma \in \partial\Omega} \int_\sigma \left(\epsilon \frac{\partial \eta}{\partial N_\sigma} \bar{\varphi} + \eta \frac{\partial \varphi^h}{\partial N_\sigma} \right) \, dA \quad \forall \eta \in P^k(\Omega). \end{aligned} \quad (3.44)$$

Note that

$$\int_{\partial\omega} \frac{\partial \eta}{\partial N_\sigma} \varphi^h \, dA = \int_\omega [\varphi^h \nabla^2 \eta + \nabla \varphi^h \cdot \nabla \eta] \, dV, \quad (3.45)$$

and

$$\int_{\partial\omega} \eta \frac{\partial \varphi^h}{\partial N_\sigma} \, dA = \int_\omega [\eta \nabla^2 \varphi^h + \nabla \varphi^h \cdot \nabla \eta] \, dA \quad (3.46)$$

for all $\omega \in \mathcal{T}_\omega(\Omega)$. For the case where $\eta \in P^1(\Omega)$, we have $\nabla^2 \eta = 0 \ \forall \eta \in P^1(\Omega)$.

Consequently,

$$\sum_{\sigma \in \Gamma_\omega \cup \partial\Omega} \int_\sigma \frac{\partial \eta}{\partial N_\sigma} [\varphi^h] \, dA = \sum_{\omega \in \mathcal{T}_\omega(\Omega)} \int_\omega \nabla \varphi^h \cdot \nabla \eta \, dV, \quad (3.47)$$

$$\sum_{\sigma \in \partial\Omega} \int_\sigma \eta \frac{\partial \varphi^h}{\partial N_\sigma} \, dA = \sum_{\omega \in \mathcal{T}_\omega(\Omega)} \int_\omega [\nabla \varphi^h \cdot \nabla \eta + \eta \nabla^2 \varphi^h] \, dV, \quad (3.48)$$

and (3.44) reduces to

$$\begin{aligned} & \left(\sum_{\omega \in \mathcal{T}_\omega(\Omega)} \int_\omega \nabla \varphi^h \cdot \nabla \eta \, dV - \sum_{\sigma \in \partial\Omega} \int_\sigma \frac{\partial \eta}{\partial N_\sigma} \bar{\varphi} \, dA \right) \epsilon \\ &= \sum_{\sigma \in \partial\Omega} \frac{\alpha_{\sigma 0}}{|\sigma|^{\beta_0}} \int_\sigma \eta (\bar{\varphi} - \varphi^h) \, dA + \sum_{\omega \in \mathcal{T}_\omega(\Omega)} \int_\omega (\nabla^2 \varphi^h + f_\Omega) \eta \, dV \quad \forall \eta \in P^1(\Omega). \end{aligned} \quad (3.49)$$

If $\varphi^h \in \mathcal{D}_1^h(\Omega)$, then $\nabla^2 \varphi^h|_\omega = 0 \ \forall \omega \in \mathcal{T}_\omega(\Omega)$. Provided $f_\Omega \equiv 0$, the above expression implies that the approximate solution $\varphi^h \in \mathcal{U}^h(\Omega) \subset \mathcal{U}(\Omega)$ to (3.34) will obey:

$$\begin{aligned} & \left(\sum_{\omega \in \mathcal{T}_\omega(\Omega)} \int_\omega \nabla \varphi^h \cdot \nabla \eta \, dV - \sum_{\sigma \in \partial\Omega} \int_\sigma \frac{\partial \eta}{\partial N_\sigma} \bar{\varphi} \, dA \right) \epsilon \\ &= \sum_{\sigma \in \partial\Omega} \frac{\alpha_{\sigma 0}}{|\sigma|^{\beta_0}} \int_\sigma \eta (\bar{\varphi} - \varphi^h) \, dA \quad \forall \eta \in P^1(\Omega). \end{aligned} \quad (3.50)$$

For any $\epsilon \neq 0$, (3.50) implies that φ^h will satisfy the first-order integration consistency conditions:

$$\sum_{\omega \in \mathcal{T}_\omega(\Omega)} \int_\omega \nabla \varphi^h dV = \sum_{\sigma \in \partial\Omega} \int_\sigma \mathbf{N}_\sigma \bar{\varphi} dA, \quad (3.51)$$

provided

$$\sum_{\sigma \in \partial\Omega} \frac{\alpha_{\sigma 0}}{|\sigma|^{\beta_0}} \int_\sigma \eta (\bar{\varphi} - \varphi^h) dA = 0 \quad \forall \eta \in P^1(\Omega). \quad (3.52)$$

This occurs primarily under two circumstances: either as $\alpha_{\sigma 0} \rightarrow \infty$ (thereby enforcing the boundary condition $\bar{\varphi} = \varphi^h$), or in the limit as $\alpha_{\sigma 0} \rightarrow 0$. For $\varphi^h \in \mathcal{D}_1^h(\Omega)$, the case of $\alpha_{\sigma 0} = 0$ is precluded by the stability condition $\alpha_{\sigma 0} > 0$.

Satisfaction of (3.52) yields a negation of the consistency errors incurred by the discontinuities in $\varphi^h \in \mathcal{D}_1^h(\Omega)$. Consequently, the errors for first order patch tests can be effectively reduced by an appropriate specification of $\alpha_{\sigma 0}$. The same cannot be said of higher order patch tests, however.

It is emphasized that only the boundary penalty terms $\alpha_{\sigma 0} \forall \sigma \in \partial\Omega$ influence the behavior of (3.52). This observation has motivated an exploration of the 3-parameter family of methods arising from:

$$\alpha_{\sigma 0} = \alpha_0|_{\partial\Omega} \quad \forall \sigma \in \partial\Omega, \quad \alpha_{\sigma 0} = \alpha_0|_{\Gamma_\omega} \quad \forall \sigma \in \Gamma_\omega, \quad \alpha_{\sigma 1} = \alpha_1|_{\Gamma_\omega} \quad \forall \sigma \in \Gamma_\omega. \quad (3.53)$$

3.6 Partition-Based Quadrature Rules

If arbitrary polytopal shapes are to be used as elements in the PEM, then there arises a need for devising a means of integrating contributions to the weak form, ostensibly through the use of domain quadrature rules. Such rules must be sufficiently stable (utilizing a sufficient number of well-positioned quadrature points) and accurate (capable of exactly integrating low-order polynomials up to some specified degree).

Partitioned element methods approach this task by subdividing the elements (and their boundaries) into a sufficient number of polytopal sub-domains which are used as integration cells. For the sake of simplicity, the element's cell partition $\mathcal{T}_\omega(\Omega)$ (which is used to construct the element's shape functions) is collocated with the integration cells. Low-order (i.e. 1-point) quadrature rules are defined on each of these sub-domains, and

a composite quadrature rule for the element is constructed from the set of all quadrature points defined in this manner. In general, such rules are straightforward to define, but will have limited accuracy. Consequently, appropriate modifications must be made to satisfy Galerkin exactness for certain low-order polynomial solutions.

Methods for partitioning the elements into sub-domains which yield stable and efficient composite quadrature rules are addressed in the following section. A discussion is given later on to the correction of these quadratures for the sake of satisfying Galerkin exactness (quadrature consistency).

Composite Quadrature Rules

Given a partition of an element into polytopal sub-domains (quadrature cells), one may utilize low order quadrature rules over each sub-domain, thereby yielding a composite quadrature rule over the element as a whole, whose overall accuracy is determined by the order of accuracy used within each sub-domain, and the distribution of quadrature cells within the element.

The simplest quadrature rule of this form is the composite mid-point scheme, where the quadrature points are located at the centroids of each sub-domain. Such a rule exactly integrates polynomials up to first order, and provides reasonable accuracy when integrating polynomials of higher-order ([62] provides a numerical assessment of the accuracy of composite mid-point quadratures.) Moreover, the integration points are guaranteed to be interior to each sub-domain (and the element as a whole), provided each cell is convex.

For simple sub-divisions (consisting of triangles or tetrahedra), composite quadrature rules may be extended rather naturally to obtain higher-order accuracy. For generic sub-divisions (consisting of arbitrary polytopes), the extension to higher-order composite rules is not as straight-forward. For this reason, subsequent discussions will be concerned almost exclusively with composite mid-point rules.

The weights and locations of a composite mid-point quadrature rule correspond to the volumes and geometric centroids of each cell. In general, a given quadrature cell ω may be an arbitrary polyhedron, whose volume $|\omega|$ and centroid $\bar{\mathbf{X}}$ may be computed using

the 0-th and 1-st order moments of ω , i.e.

$$|\omega| = \int_{\omega} dV, \quad \bar{\mathbf{X}} = \frac{\int_{\omega} \mathbf{X} dV}{\int_{\omega} dV}. \quad (3.54)$$

Using the method proposed by Chin et al. in [18], the computation of monomial moments of arbitrary degree $|\alpha|$ may be effected via an integral over $\partial\omega$:

$$\int_{\omega} \mathbf{X}^{\alpha} dV = \frac{1}{d+|\alpha|} \int_{\partial\omega} (\mathbf{X} \cdot \mathbf{N}) \mathbf{X}^{\alpha} dA, \quad (3.55)$$

for any arbitrary polytope $\omega \subset \mathbb{R}^d$. If $\partial\omega$ may be partitioned into a collection of $d-1$ dimensional facets $\sigma \subset \partial\omega$, then

$$\int_{\omega} \mathbf{X}^{\alpha} dV = \frac{1}{d+|\alpha|} \sum_{\sigma \in \partial\omega} \int_{\sigma} (\mathbf{X} \cdot \mathbf{N}_{\sigma}) \mathbf{X}^{\alpha} dA, \quad (3.56)$$

where \mathbf{N}_{σ} is the outward (with respect to ω) unit normal associated with facet σ . We remark that any location \mathbf{X} positioned on a given facet σ may be expressed as

$$\mathbf{X} = \mathbf{X}_{\sigma} + \sum_{i=1}^{d-1} X_i \hat{\mathbf{X}}_i, \quad (3.57)$$

where \mathbf{X}_{σ} is any reference location positioned on the plane which contains σ , and the orthonormal set $\{\hat{\mathbf{X}}_i\}_{i=1}^{d-1}$ defines a parameterization of the in-plane coordinates on σ .

This leads to the observation $\mathbf{X} \cdot \mathbf{N}_{\sigma} = \mathbf{X}_{\sigma} \cdot \mathbf{N}_{\sigma} \forall \mathbf{X} \in \sigma$, and thus

$$\int_{\omega} \mathbf{X}^{\alpha} dV = \frac{1}{d+|\alpha|} \sum_{\sigma \in \partial\omega} (\mathbf{X}_{\sigma} \cdot \mathbf{N}_{\sigma}) \int_{\sigma} \mathbf{X}^{\alpha} dA. \quad (3.58)$$

The integral of \mathbf{X}^{α} over each facet may in turn be carried out via

$$\int_{\sigma} \mathbf{X}^{\alpha} dA = \frac{1}{d-1+|\alpha|} \left[\sum_{\gamma \in \partial\sigma} ((\mathbf{X}_{\gamma} - \mathbf{X}_{\sigma}) \cdot \mathbf{N}_{\gamma}) \int_{\gamma} \mathbf{X}^{\alpha} dS + \mathbf{X}_{\sigma} \cdot \int_{\sigma} \nabla \mathbf{X}^{\alpha} dA \right], \quad (3.59)$$

and the integral over each segment is

$$\int_{\gamma} \mathbf{X}^{\alpha} dS = \frac{1}{d-2+|\alpha|} \left[\sum_{v \in \partial\gamma} ((\mathbf{X}_v - \mathbf{X}_{\gamma}) \cdot \mathbf{N}_v) \mathbf{X}_v^{\alpha} + \mathbf{X}_{\gamma} \cdot \int_{\gamma} \nabla \mathbf{X}^{\alpha} dS \right]. \quad (3.60)$$

Similarly defined composite rules may be defined on each polygonal face of a given polyhedral element, or on each edge of a polygonal element. However, while composite mid-point quadrature rules are able to provide reasonable accuracy, they will not necessarily lead to quadrature consistency, as expressed in (2.67). For this reason, a gradient correction scheme (such as the one proposed by Bishop in [11], or by Talischi in [79]) must be employed, as discussed in the following section.

Gradient Correction Scheme

Consider an element $\Omega \subset \mathbb{R}^d$ upon which is specified a domain quadrature rule $\{\mathbf{X}_q, w_q\}_{q=1}^{N_{qp}}$ such that the integral of a scalar function $f \in L^2(\Omega)$ over Ω is approximated by

$$\int_{\Omega} f dV \approx \sum_{q=1}^{N_{qp}} w_q f(\mathbf{X}_q). \quad (3.61)$$

Additionally, suppose that each face $F \subset \partial\Omega$ possesses a quadrature rule $\{\mathbf{X}_b, w_b, \mathbf{N}^{(b)}\}_{b=1}^{N_{bp}^F}$ where $\mathbf{N}^{(b)}$ denotes the unit normal to the face F evaluated at $\mathbf{X}_b \in F$. The integral of a scalar function $f \in L^2(\partial\Omega)$ (or of a vector-valued function $f \mathbf{N}$) over $\partial\Omega$ is approximated by

$$\int_{\partial\Omega} f dA \approx \sum_{F \in \partial\Omega} \sum_{b=1}^{N_{bp}^F} w_b f(\mathbf{X}_b), \quad \int_{\partial\Omega} f \mathbf{N} dA \approx \sum_{F \in \partial\Omega} \sum_{b=1}^{N_{bp}^F} w_b f(\mathbf{X}_b) \mathbf{N}^{(b)}. \quad (3.62)$$

Suppose that the aforementioned quadrature rules (on a given polyhedral element Ω and on each of its polygonal faces $F \subset \partial\Omega$) are constructed using the composite midpoint quadrature scheme discussed in the previous section. A simple gradient correction scheme is obtained by introducing an auxiliary field $\boldsymbol{\xi} = \nabla\phi - \nabla\varphi$, such that a given trial function φ and its corresponding test function ϕ differ (minimally), to the extent that the quadrature consistency conditions hold:

$$\sum_{q=1}^{N_{qp}} w_q [\mathbf{X}_q^\alpha \nabla\phi(\mathbf{X}_q) + \nabla\mathbf{X}_q^\alpha \phi(\mathbf{X}_q)] = \sum_{F \in \partial\Omega} \sum_{b=1}^{N_{bp}^F} w_b \mathbf{X}_b^\alpha \phi(\mathbf{X}_b) \mathbf{N}^{(b)} \quad \forall |\alpha| \leq k-1, \quad (3.63)$$

for every test function ϕ , where k represents the degree of polynomial completeness exhibited by the space of trial solutions. Given the discrete conditions:

$$\phi(\mathbf{X}_b) = \varphi(\mathbf{X}_b) \quad \forall \mathbf{X}_b \in \partial\Omega, \quad (3.64)$$

$$\phi(\mathbf{X}_q) = \varphi(\mathbf{X}_q) \quad \forall \mathbf{X}_q \in \Omega, \quad \nabla\phi(\mathbf{X}_q) = \nabla\varphi(\mathbf{X}_q) + \boldsymbol{\xi}(\mathbf{X}_q) \quad \forall \mathbf{X}_q \in \Omega, \quad (3.65)$$

we obtain $\boldsymbol{\xi}(\mathbf{X}_q)$ as the solution to the quadratic minimization problem:

$$\min_{\boldsymbol{\xi}} \frac{1}{2} \|\boldsymbol{\xi}\|_{\Omega}^2, \quad (3.66)$$

subject to (3.63), where $\|\boldsymbol{\xi}\|_\Omega$ is deliberately approximated using the element's quadrature rule, i.e.

$$\|\boldsymbol{\xi}\|_\Omega \approx \left[\sum_{q=1}^{N_{qp}} w_q [\xi_i(\mathbf{X}_q) \xi_i(\mathbf{X}_q)] \right]^{1/2}. \quad (3.67)$$

Suppose two adjacent elements Ω_L and Ω_R share a given face $F = \partial\Omega_L \cap \partial\Omega_R$. If the shape functions and quadrature rules defined on $F_L \subset \partial\Omega_L$ and $F_R \subset \partial\Omega_R$ (where $F_L = F_R$) are identical, then the aforementioned gradient correction scheme will automatically lead to satisfaction of finite element patch tests. However, if Ω_L and Ω_R provide separate quadrature rules on F_L and F_R (arising from different partitions of the shared face), or if the elements' shape functions are not defined identically on F_L and F_R , then we require that an additional condition be met:

$$\sum_{l=1}^{N_{bp}^{FL}} w_l \mathbf{X}_l^\alpha \phi_l \mathbf{N}^{(l)} = - \sum_{r=1}^{N_{bp}^{FR}} w_r \mathbf{X}_r^\alpha \phi_r \mathbf{N}^{(r)} \quad \forall |\alpha| \leq k-1, \quad (3.68)$$

for every shared face $\partial\Omega_L \subset F_L = F_R \subset \partial\Omega_R$.

Chapter 4

An Implementational Framework for the DG-PEM

The implementation of any partitioned element method must address two primary challenges: the subdivision of an element into cells, and the solution of shape function-specific boundary value problems by way of the chosen PEM formulation. The first of these two tasks may be accomplished by various means. However, careful attention must be paid to the stability requirements of the PEM, such that the resulting quadrature cell partition yields stable approximations to harmonic shape functions, and an equally stable integration rule for the element. Specifying such a discretization is not trivial for arbitrary shapes. For this reason, we will confine our attention to strictly star-convex elements, for which we propose a relatively simple (edge-based) element partitioning algorithm.

The present implementational framework is directed at obtaining DG-PEM approximations to harmonic shape functions on arbitrary polytopes – i.e. solving (3.34) on an appropriately defined partition of the element. A discussion of the pertinent data structures and solution methods is provided, and a number of concluding remarks are given with regard to numerical robustness of the proposed methodology.

4.1 Arbitrary Polytopal Meshes

Traditional finite element methods typically permit the elements to only take the form of certain canonical shapes with fixed topology (most commonly tetrahedra or hexahedra).

This yields several benefits with regard to the data and storage requirements necessary to represent a given element in a computational setting. Frequently, it suffices to describe the geometry of a canonical shape (such as a hexahedron) by providing a list of the element's nodal coordinates, along with an ordered sequence of the element's nodal IDs, which fully determines its resulting topology according to some conventional node numbering scheme (refer to Figure 4.1 as a representative example.)

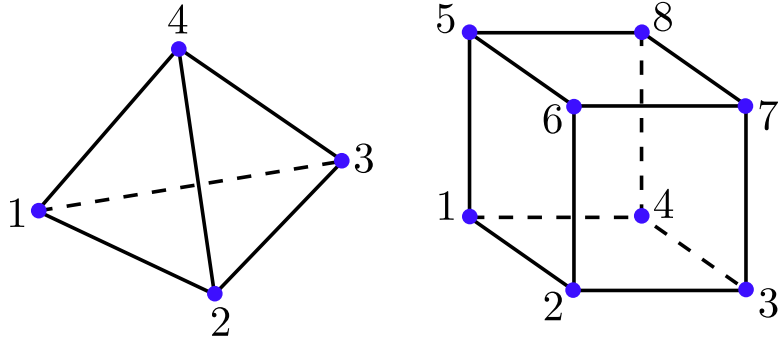


Figure 4.1: Canonical node numbering schemes for a linear tetrahedral element (left) and a linear hexahedral element (right). Each of these standard orderings induce corresponding nodal orderings for each triangular or quadrilateral face of the element, as well.

Polytopal elements with arbitrary topology (with a variable number of nodes, edges, and faces) cannot be represented in this fashion. As a consequence, more descriptive data structures are necessary to fully determine a polytopal element's nodal connectivity. A particular scheme to represent an arbitrary polyhedron within a finite element mesh is described in the following section.

Geometric Data Structures for Arbitrary Polytopes

There are multiple ways in which the geometry of a given polyhedral element Ω may be represented within a finite element code. Ideally, however, the chosen data structure should be made as compact as possible, for the sake of minimizing the storage requirements of a single element. This section describes a few basic data structures for storing arbitrary polygonal and polyhedral shapes within an unstructured finite element mesh.

The geometric data used to describe a typical finite element mesh consists of the following:

- A list of the spatial coordinates $\{\mathbf{X}_a\}_{a=1}^{N_V^{\mathcal{B}_0}}$ for all nodes in the mesh. The sub-index $a \in 1, \dots, N_V^{\mathcal{B}_0}$ induces a *global node ID* ascribed to each node.
- A list of all elements $\{\Omega_e\}_{e=1}^{N_{\Omega}^{\mathcal{B}_0}}$ where $\Omega_e \subset \mathcal{B}_0$. The sub-index $e \in 1, \dots, N_{\Omega}^{\mathcal{B}_0}$ induces an associated *element ID*.
- A list of all faces $\{F_b\}_{b=1}^{N_F^{\Gamma_0^N}}$ where $F_b \subset \Gamma_0^N$ to which traction boundary conditions are assigned. Likewise, the sub-index $b \in 1, \dots, N_F^{\Gamma_0^N}$ induces a *boundary face ID*.

In a finite element mesh consisting of arbitrary polyhedral elements, it is suggested that each element Ω_e be represented by the following data:

- A list of the global node IDs $\{a_i\}_{i=1}^{N_V^{\Omega_e}}$ comprising the set of nodes belonging to Ω_e . The sub-index $i \in 1, \dots, N_V^{\Omega_e}$ induces a *local node ID*, particular to the element Ω_e .
- A list of the polygonal faces $\{F_j\}_{j=1}^{N_F^{\Omega_e}}$ which belong to $\partial\Omega_e$; each polygonal face F_j is in turn represented by a cycle of local node IDs denoted $\{n_i\}_{i=1}^{N_V^{F_j}}$, which further determine each face's outward orientation with respect to the element Ω_e .

An illustration of this collection of data for a given polyhedron Ω_e is provided in Figure 4.2.

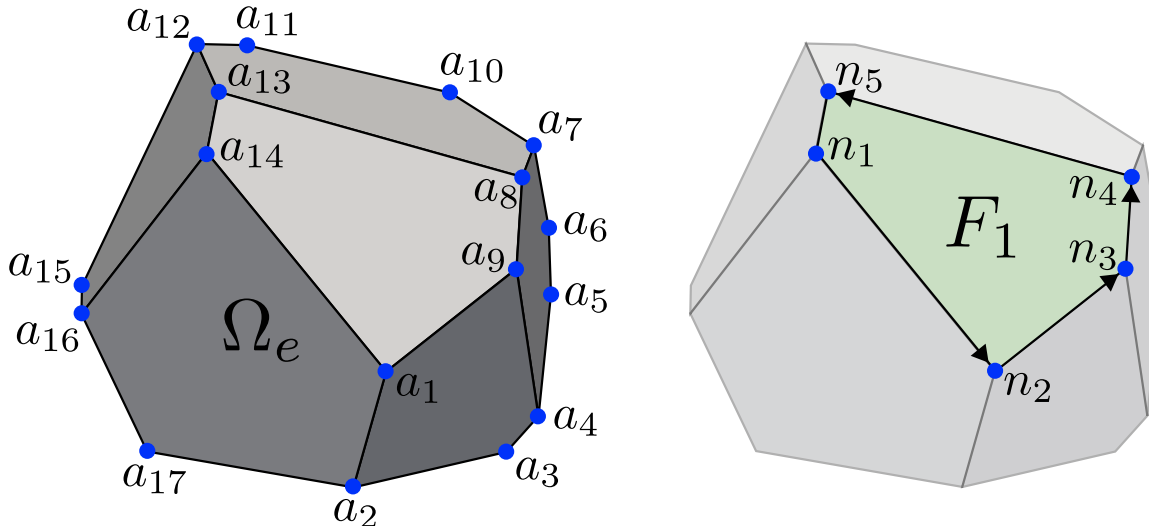


Figure 4.2: Illustration of the data necessary to describe an arbitrary polyhedral element Ω_e . The local node ID ordering for the face F_1 shown would be $\{n_i\}_{i=1}^5 = \{14, 1, 9, 8, 13\}$.

A given polygonal face $F_b \subset \Gamma_0^N$ will similarly be represented by:

- A list of the global node IDs $\{a_i\}_{i=1}^{N_V^{F_b}}$ which belong to F_b .
- A list of the linear edges $\{E_c\}_{c=1}^{N_E^{F_b}}$ which belong to ∂F_b ; each linear edge E_c is in turn represented as an ordered list of local node IDs $\{n_i\}_{i=1}^{N_V^{E_c}}$.

Unlike canonical finite element shapes, the ordering of the element's nodal IDs is effectively arbitrary, and does not induce a topology. Rather, the element's topology is determined by virtue of its polygonal faces, and their respective (conventionally clockwise) local node orderings. Consequently, each edge of a given polyhedron is defined implicitly as the intersection of two adjacent faces' ordered node sets. Such a scheme may be easily generalized to accommodate serendipity elements containing additional nodes along element edges, as illustrated in Figure 4.3.

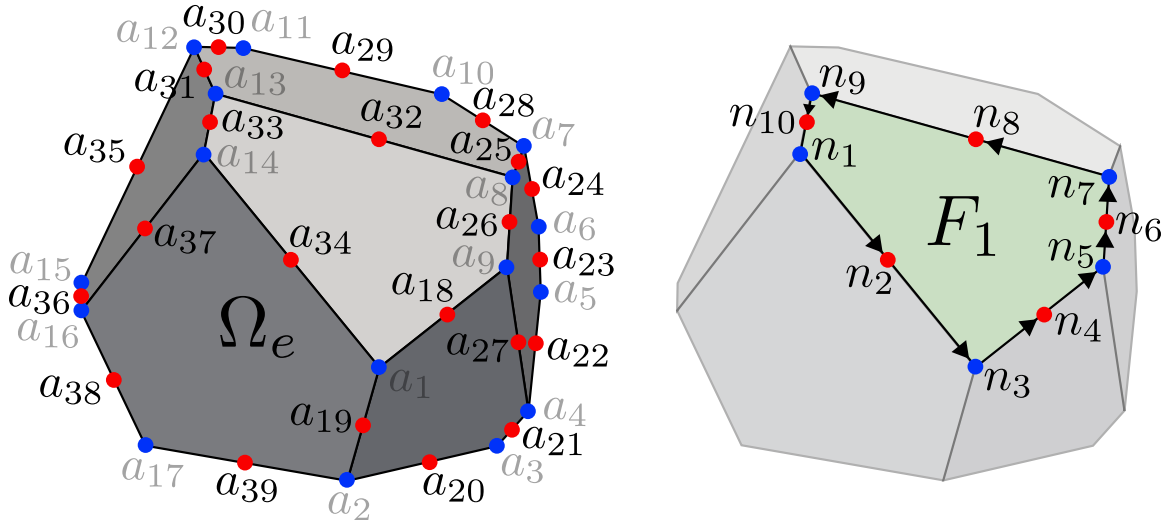


Figure 4.3: Illustration of the data necessary to describe a quadratic serendipity polyhedral element Ω_e . The local node ID ordering for the face F_1 shown would be $\{n_i\}_{i=1}^{10} = \{14, 34, 1, 18, 9, 26, 8, 32, 13, 33\}$.

Finite Element Data for Arbitrary Polytopes

Traditional Lagrangian finite element methods require each element $\Omega_e \subset \mathcal{B}_0$ to carry the following data (at a minimum) for the purposes of evaluating weak form integrals:

- A list of quadrature weights $\{w_q\}_{q=1}^{N_{qp}^{\Omega_e}}$ associated with the quadrature points of the element. The sub-index q induces a local *quadrature point ID*.

- Evaluations of the element's nodal shape functions $\{\varphi_a(\mathbf{X}_q)\}_{q=1}^{N_{qp}^{\Omega_e}} \forall a = 1, \dots, N_V^{\Omega_e}$ at each quadrature point location \mathbf{X}_q .
- Gradients (with respect to the element's reference coordinates \mathbf{X} at time $t = 0$) of the element's nodal shape functions $\{\nabla_X \varphi_a(\mathbf{X}_q)\}_{q=1}^{N_{qp}^{\Omega_e}} \forall a = 1, \dots, N_V^{\Omega_e}$.
- (Optionally) if the element relies upon some form of gradient correction scheme (or more generally, if a Petrov-Galerkin method is employed): evaluations and/or gradients of the element's test functions $\{\phi_a(\mathbf{X}_q), \nabla_X \phi_a(\mathbf{X}_q)\}_{q=1}^{N_{qp}^{\Omega_e}} \forall a = 1, \dots, N_V^{\Omega_e}$ must be stored, as well.

For solid mechanics applications, material state data (e.g. material properties, internal variables, Cauchy stress) would also need to be stored at each quadrature point location.

Similarly, each boundary face $F_b \subset \Gamma_0^N$ must carry:

- A list of quadrature weights $\{w_q\}_{q=1}^{N_{qp}^{F_b}}$ for each quadrature point of the face.
- Evaluations of the face's nodal shape functions $\{\varphi_a(\mathbf{X}_q)\}_{q=1}^{N_{qp}^{F_b}} \forall a = 1, \dots, N_V^{F_b}$ at each quadrature point location \mathbf{X}_q .
- Gradients (with respect to the face's in-plane reference coordinates \mathbf{X} at $t = 0$) of the face's nodal shape functions $\{\nabla_X \varphi_a(\mathbf{X}_q)\}_{q=1}^{N_{qp}^{F_b}} \forall a = 1, \dots, N_V^{F_b}$.
- If a Petrov-Galerkin method is employed: evaluations and/or gradients of the face's test functions $\{\phi_a(\mathbf{X}_q), \nabla_X \phi_a(\mathbf{X}_q)\}_{q=1}^{N_{qp}^{F_b}} \forall a = 1, \dots, N_V^{F_b}$.
- Outward unit normals $\{\mathbf{N}_q\}_{q=1}^{N_{qp}^{F_b}}$ to the face F_b at each quadrature point.

The data enumerated above must be determined via a specified *element formulation*: the method by which the element's shape functions and quadrature rule are constructed. Partitioned element methods address precisely this task. Given an abstract representation for the geometry of a given polyhedral element Ω (as discussed in the previous section), a PEM formulation proceeds in a number of distinct steps:

- 1.) The element (and its faces, edges) are appropriately partitioned into cells (facets, segments, vertices).

- 2a.) Individual nodal shape functions are constructed along each edge E of the element.
- 2b.) Individual nodal shape functions are constructed on each face F of the element.
- 2c.) Individual nodal shape functions are constructed on the interior of the element Ω .
- 3.) The discrete finite element data (including quadrature point evaluations of the shape functions and their gradients) are computed and stored by the element.
- 4.) Any auxiliary data (regarding the element's partitioned geometry, etc.) is discarded.

Depending on how the chosen PEM is carried out, the above process can amount to a relatively large computational expense. However, if a total Lagrangian approach is employed within the associated finite element analysis, then the above methodology would only need to be carried out once for each element, at the beginning of the simulation (prior to the first time step). Consequently, the cost of constructing element shape functions in this manner is amortized over the duration of the analysis.

The subsequent sections of this chapter are dedicated to a more detailed discussion of the aforementioned steps taken to construct a given element's partition, and its shape functions.

4.2 Element Partitioning Schemes

The process of obtaining a suitable partition for a given element constitutes the greatest challenge facing partitioned element methods – an issue of computational geometry, primarily. The secondary complication arises from the conditions of stability that the element must satisfy: the shape function approximations, and the corresponding quadrature rules defined on the element's partition must guarantee a sufficiently stable integration of the weak form. For relatively simple shapes, a number of stable partitioning schemes exist. However, for arbitrary shapes, it becomes difficult – if not impossible – for a heuristically-driven discretization scheme to guarantee that the resulting partition will satisfy the aforementioned stability requirements.

For this reason, we will limit our subsequent discussion to *star-convex* element geometries. For such shapes, a relatively simple partitioning scheme is suggested, resembling the

decomposition used in the edge-based smoothed finite element method. In the absence of degenerate features, the resulting partition is verified to provide sufficiently stable shape function approximations and quadrature rules.

Edge-Based Partitioning for Star-Convex Elements

A star-convex shape Ω is one for which there exists some interior point $\mathbf{X}_0^\Omega \in \Omega$ such that the line segment connecting any point $\mathbf{X} \in \Omega$ to \mathbf{X}_0^Ω is entirely contained within Ω . If $\Omega \subset \mathbb{R}^3$ refers to a polyhedron which is star-convex, this further implies that each polygonal face $F \subset \partial\Omega$ is also star-convex with respect to some point $\mathbf{X}_0^F \in F$. Any linear edge $E \subset \partial F$ is star-convex with respect to any point $\mathbf{X} \in E$.

A simple and efficient partitioning scheme is described for polyhedral elements Ω (and their polygonal faces F_j) which are star-convex with respect to their vertex-averaged centroids $\bar{\mathbf{X}}_0^\Omega$ (or $\bar{\mathbf{X}}_0^{F_j}$), i.e.

$$\bar{\mathbf{X}}_0^\Omega = \frac{1}{N_V^\Omega} \sum_{i=1}^{N_V^\Omega} \mathbf{X}_i, \quad \text{and} \quad \bar{\mathbf{X}}_0^{F_j} = \frac{1}{N_V^{F_j}} \sum_{i=1}^{N_V^{F_j}} \mathbf{X}_i. \quad (4.1)$$

For a given polyhedral element Ω , the algorithm proceeds in several steps:

- 1.) Identify all edges of the polyhedron, and subdivide them into linear segments; each segment should join two adjacent nodes of a given edge.
- 2.) For each face, compute its vertex-averaged centroid $\bar{\mathbf{X}}_0^{F_j}$, and subdivide the face into triangular facets which emanate from $\bar{\mathbf{X}}_0^{F_j}$; each facet should share at most two segments (at least one segment) with ∂F_j .
- 3a.) Compute the element's vertex-averaged centroid $\bar{\mathbf{X}}_0^\Omega$, and subdivide the element into tetrahedra which emanate from $\bar{\mathbf{X}}_0^\Omega$; each tetrahedron should share a single facet with $\partial\Omega$.
- 3b.) Lump into cells any tetrahedra which share a segment belonging to an edge of Ω ; each cell should consist of exactly two tetrahedra.

An illustration of this process is depicted in Figure 4.4. A similar algorithm may be applied to each boundary face $F_b \subset \Gamma_0^N$, entailing only the first two steps described above.

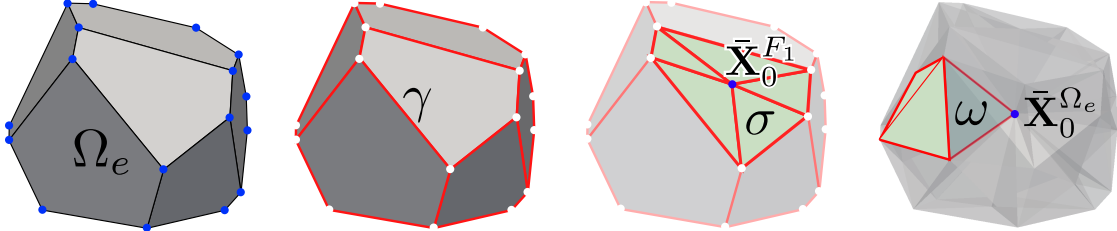


Figure 4.4: The resulting segment, facet, and cell decomposition for the proposed edge-based partitioning algorithm.

The algorithm can also be naturally extended to accommodate serendipity polyhedral elements, with additional nodes belonging to element edges, as depicted in Figure 4.5.

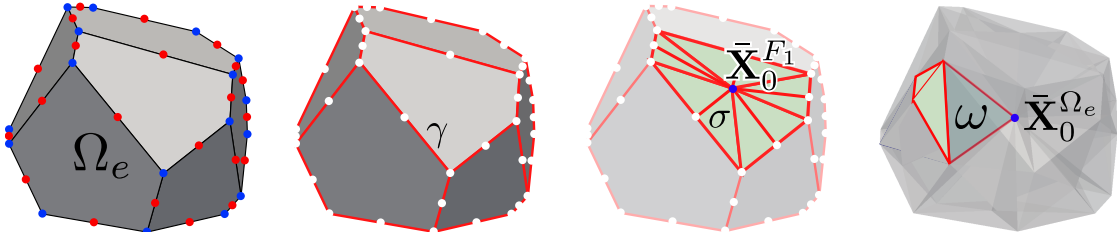


Figure 4.5: The resulting segment, facet, and cell decomposition for the proposed edge-based partitioning algorithm, applied to a quadratic serendipity polyhedral element.

A crucial advantage of this approach is that the partition deterministically obtained for each edge (face) will be identical between all elements that share that edge (face), leading to direct satisfaction of (3.68). As such, the gradient correction schemes discussed in section 3.6 may be applied independently to each element. Moreover, because each element may be partitioned in an autonomous fashion (without knowledge of any neighboring elements), the computations required to construct each element's shape functions can be directly parallelized.

4.3 Abstract Geometric Data Structures

Because partitioned element methods consist of solving a set of 1D, 2D, and 3D problems on each edge, face, and element, there arise a number of similarities between these

problems of variable dimension. Namely, the geometric data describing each cell, facet, segment and vertex may be abstracted through the use of generic parent-child (tree-based) data structures. Instead of requiring a separate implementation for the solution of each 1D, 2D, 3D problem, generic programming paradigms are exploited to facilitate a single, unified implementation which is agnostic to the dimensionality of the problem being solved. The proposed organization shares many similarities with the generic programming approaches presented in [20]. A number of definitions for the abstract data structures used henceforth are given in the following sections.

Geometric Entities

Geometric entities (or simply *entities*) are defined as the atomic units of the element’s geometric partition. An entity may be: a polyhedral cell, a polygonal facet, a linear segment, or a vertex. Entities are defined in terms of their relationship to other geometric entities. Specifically, a 3–dimensional entity (a polyhedral cell ω) is uniquely defined in terms of its 2-dimensional facets $\sigma \subset \partial\omega$ (termed the “children” of ω). Each facet σ is in turn considered a 2-dimensional entity, defined in terms of its 1-dimensional children (its bounding segments $\gamma \subset \partial\sigma$). An entity of dimension 0 (a vertex) is identified as having no children.

Each geometric entity may be viewed as a “node” in a corresponding tree diagram, as illustrated in Figure 4.6, where the height of a given entity within the tree structure indicates its dimensionality d .

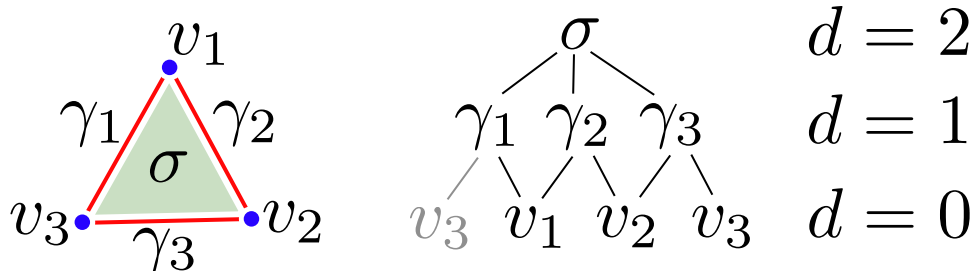


Figure 4.6: A representative entity tree diagram for a 2-dimensional facet σ and its children.

Henceforth, we denote by ε any generic d -dimensional entity, and by ζ any $(d - 1)$ -dimensional child of ε (such that $\zeta \subset \partial\varepsilon$). The data stored on a given entity ε consists

of:

- Information (pointers or entity IDs) referring to the $(d - 1)$ -dimensional children of ε , and/or information (pointers or entity IDs) referring to the $(d + 1)$ -dimensional parents of ε .
- An (optional) orientation/unit direction \mathbf{N}_ε .
- A quadrature rule $\{\mathbf{X}_q, w_q\}_{q=1}^{N_{qp}^\varepsilon}$ defined on ε , or pre-computed monomial integrals $\int_\varepsilon \mathbf{X}^\alpha d\varepsilon$ for all $|\alpha| \leq k$ (alternatively, the shifted monomial moments $\int_\varepsilon (\mathbf{X} - \mathbf{X}_\varepsilon)^\alpha d\varepsilon$ may be computed and stored, instead.)
- A list of the DG-PEM basis function IDs which possess compact support over ε .

If quadrature rules are to be defined on each geometric entity, we may exploit the particular choice made regarding the element's edge-based partition, noting that every polygonal facet will be a triangle, and every polyhedral cell will consist of two adjoining tetrahedra, allowing for the use of standard Dunavant [25] and Grundmann-Möller [39] quadrature rules for triangles and tetrahedra, respectively. Standard Gaussian quadrature rules may be specified on each linear segment.

The advantage of defining entities in this fashion is that it affords greater flexibility in solving the DG-PEM problem (3.34) on elements with arbitrary dimensionality.

Sub-Elements

Herein, a *sub-element* (generically denoted as \mathcal{E}) is defined as a d -dimensional polytope (a polyhedral element, a polygonal face, a linear edge, or a node) upon which nodal shape functions are locally constructed and defined as the solution to a d -dimensional boundary value problem. Sub-elements consist of a partition $\mathcal{T}_\varepsilon(\mathcal{E})$ of \mathcal{E} into d -dimensional entities ε . The boundary of each sub-element \mathcal{E} is comprised of $(d - 1)$ -dimensional sub-elements, denoted $e \subset \partial\mathcal{E}$ (called the “children” of \mathcal{E} , in analog to the terminology used for geometric entities). A sub-element of dimension 0 (a node) refers to a single vertex, and possesses no children.

As a representative example, consider the face $F \subset \partial\Omega$ shown in Figure 4.7, which is classified as a 2-dimensional sub-element, whose partition $\mathcal{T}_\sigma(F)$ consists of 2-dimensional facets $\sigma \subset F$. The children of F are comprised of 1-dimensional sub-elements – edges $E \subset \partial F$; in turn, the children of each edge E are the nodes of the element. As with geometric entities, the parent-child relationships between different sub-elements induces a tree-like data structure, where the height of a given sub-element within the tree corresponds to its dimensionality d .

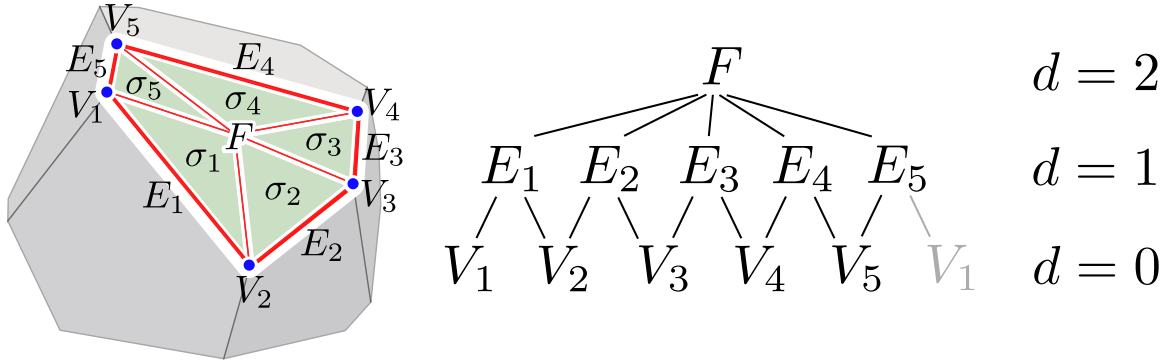


Figure 4.7: A representative 2-dimensional sub-element $F \subset \partial\Omega$ (a polygonal face), and its corresponding sub-element tree diagram. The partition of F consists of polygonal facets $\sigma_i \in \mathcal{T}_\sigma(F) \forall i = 1, \dots, 5$.

The data stored for a given sub-element \mathcal{E} consists of:

- Information (pointers or entity IDs) referring to the d -dimensional entities $\varepsilon \in \mathcal{T}_\varepsilon(\mathcal{E})$ belonging to the partition of \mathcal{E} .
- Information (pointers or sub-element IDs) referring to the $(d - 1)$ -dimensional children of \mathcal{E} (the sub-elements $e \subset \partial\mathcal{E}$ which constitute the boundary of \mathcal{E}).
- A list of the DG-PEM basis function IDs which are defined on $\mathcal{T}_\varepsilon(\mathcal{E})$.

A more thorough discussion is dedicated to the subject of DG-PEM basis functions in the following section.

4.4 Partition-Based Approximation Spaces

As discussed in chapter 3, partitioned element methods consider a weak formulation of a given PDE (e.g. Laplace's equation), whose solution is approximated through the spec-

ification of a finite dimensional function space $\mathcal{U}^h(\mathcal{E})$ defined on the partition $\mathcal{T}_\varepsilon(\mathcal{E})$ of a given sub-element \mathcal{E} . The (sub-)element's shape functions are selected as the “best approximations” to (harmonic) functions which are contained within the chosen approximation space $\mathcal{U}^h(\mathcal{E})$.

Herein, we consider $\mathcal{U}^h(\mathcal{E}) = \mathcal{D}_k^h(\mathcal{E}) = \{\varphi \in L^2(\mathcal{E}) : \varphi|_\varepsilon \in P^k(\varepsilon) \forall \varepsilon \in \mathcal{T}_\varepsilon(\mathcal{E})\}$ to be spanned by a set of basis functions $\{\psi_A\}_{A=1}^{N_{bf}^\varepsilon}$, such that each basis function $\psi \in \mathcal{U}^h(\mathcal{E})$ is compactly supported over a given geometric entity $\varepsilon \in \mathcal{T}_\varepsilon(\mathcal{E})$ (or patch of entities).

Any function $\varphi^h \in \mathcal{U}^h(\mathcal{E})$ may be written as a linear combination of the basis functions which span $\mathcal{U}^h(\mathcal{E})$, i.e.

$$\varphi^h(\mathbf{X}) = \sum_{A=1}^{N_{bf}^\varepsilon} \psi_A(\mathbf{X}) \varphi_A \quad \forall \mathbf{X} \in \mathcal{E}. \quad (4.2)$$

The restriction of φ^h to a given geometric entity ε may be written in terms of only those basis functions $\{\psi_a^\varepsilon\}_{a=1}^{N_{bf}^\varepsilon} \subset \mathcal{U}^h(\Omega)$ which possess compact support over ε , such that

$$\varphi^h|_\varepsilon(\mathbf{X}) = \sum_{a=1}^{N_{bf}^\varepsilon} \psi_a^\varepsilon(\mathbf{X}) \varphi_a \quad \forall \mathbf{X} \in \varepsilon. \quad (4.3)$$

To guarantee $P^k(\mathcal{E}) \subset \mathcal{U}^h(\mathcal{E})$ for some desired degree of polynomial completeness k , it is necessary for a given entity's local basis $\{\psi_a^\varepsilon\}_{a=1}^{N_{bf}^\varepsilon}$ to span $P^k(\varepsilon)$. Arguably the simplest such basis consists of the monomials through order k defined on each entity $\varepsilon \in \mathcal{T}_\varepsilon(\mathcal{E})$. However, the use of (unscaled) monomial bases can lead to ill-conditioning of the DG-PEM problem, particularly as the maximal polynomial degree k is increased. This fact has been well-established in the literature pertaining to discontinuous Galerkin methods (see for example [41].) For this reason, other (well-scaled) polynomial bases are recommended, such as the Lagrange polynomials defined on each entity (for linear segments and triangular facets), or the orthogonal polynomials obtained via the methodology proposed in [9]. An exploration of the condition number for the resulting DG-PEM systems of equations is presented at the end of this chapter.

Irrespective of the chosen basis, each basis function $\psi(\mathbf{X})$ may be expressed as a low-order polynomial (of maximal degree k) via a linear combination of (possibly shifted)

monomials:

$$\psi(\mathbf{X}) = \sum_{|\alpha| \leq k} c_\alpha (\mathbf{X} - \mathbf{X}_0)^\alpha, \quad (4.4)$$

where $\alpha = \alpha_1, \dots, \alpha_d$ is a multi-index, such that $|\alpha| = \alpha_1 + \dots + \alpha_d$ and $\mathbf{X}^\alpha = X_1^{\alpha_1} \cdots X_d^{\alpha_d}$. Consequently, a given basis function is uniquely defined in terms of its shifted coordinate \mathbf{X}_0 , and its monomial coefficients c_α . The gradient of a given basis function $\nabla\psi(\mathbf{X})$ may in turn be computed via

$$\frac{\partial \psi(\mathbf{X})}{\partial X_i} = \sum_{|\alpha| \leq k} \alpha_i c_\alpha (\mathbf{X} - \mathbf{X}_0)^{\alpha_1, \dots, (\alpha_i-1), \dots, \alpha_d}. \quad (4.5)$$

4.5 Linearization and Assembly of the DG-PEM Systems of Equations

The DG-PEM problem of (3.34) may be written in terms of the chosen basis $\{\psi_A\}_{A=1}^{N_{bf}^\varepsilon}$ for $\mathcal{D}_k^h(\mathcal{E})$, such that the basis function coefficients $\varphi_A \forall A = 1, \dots, N_{bf}^\varepsilon$ representing a given shape function $\varphi^h(\mathbf{X}) = \sum_{A=1}^{N_{bf}^\varepsilon} \psi_A(\mathbf{X}) \varphi_A$ may be determined as the solution to a linear system of equations:

$$\sum_{A=1}^{N_{bf}^\varepsilon} J_{AB} \varphi_A = F_B \quad \forall B = 1, \dots, N_{bf}^\varepsilon, \quad (4.6)$$

where J_{AB} and F_B are computed via an entity-wise assembly process following to the methodology described in [65]. In addition to assembling local contributions J_{ab}^ε and F_b^ε to J_{AB} and F_B from all d -dimensional entities $\varepsilon \in \mathcal{T}_\varepsilon(\mathcal{E})$, it is also necessary to assemble appropriate contributions from all $(d-1)$ -dimensional interfaces $\zeta \in \Gamma_\varepsilon \cup \partial\mathcal{E}$, as well.

Specifically, each d -dimensional entity $\varepsilon \in \mathcal{T}_\varepsilon(\mathcal{E})$ contributes the following local arrays:

$$J_{ab}^\varepsilon = \int_\varepsilon \nabla \psi_a^\varepsilon \cdot \nabla \psi_b^\varepsilon d\varepsilon, \quad \forall a, b = 1, \dots, N_{bf}^\varepsilon, \quad (4.7)$$

$$F_b^\varepsilon = \int_\varepsilon f_\varepsilon \psi_b^\varepsilon d\varepsilon \quad \forall b = 1, \dots, N_{bf}^\varepsilon. \quad (4.8)$$

Each $\zeta \in \partial\mathcal{E}$ (which borders a single d -dimensional entity ε) contributes:

$$J_{ab}^\varepsilon = \int_\zeta \left(\epsilon (\mathbf{N}_\zeta \cdot \nabla \psi_b^\varepsilon) \psi_a^\varepsilon - \psi_b^\varepsilon (\mathbf{N}_\zeta \cdot \nabla \psi_a^\varepsilon) \right) d\zeta + \frac{\alpha_{\zeta 0}}{|\zeta|^{\beta_0}} \int_\zeta \psi_a^\varepsilon \psi_b^\varepsilon d\zeta \quad \forall a, b = 1, \dots, N_{bf}^\varepsilon, \quad (4.9)$$

$$F_b^\varepsilon = \int_\zeta \epsilon (\mathbf{N}_\zeta \cdot \nabla \psi_b^\varepsilon) \bar{\varphi} d\zeta + \frac{\alpha_{\zeta 0}}{|\zeta|^{\beta_0}} \int_\zeta \bar{\varphi} \psi_b^\varepsilon d\zeta \quad \forall b = 1, \dots, N_{bf}^\varepsilon, \quad (4.10)$$

and each $\zeta \in \Gamma_\varepsilon$ (which borders two d -dimensional entities, ε_1 and ε_2) contributes:

$$J_{ab}^{\varepsilon_i \varepsilon_j} = -\frac{1}{2} \int_\zeta \left((-1)^i \epsilon (\mathbf{N}_\zeta \cdot \nabla \psi_b^{\varepsilon_j}) \psi_a^{\varepsilon_i} - (-1)^j \psi_b^{\varepsilon_j} (\mathbf{N}_\zeta \cdot \nabla \psi_a^{\varepsilon_i}) \right) d\zeta \quad (4.11)$$

$$+ (-1)^{(i+j)} \frac{\alpha_{\zeta 0}}{|\zeta|^{\beta_0}} \int_\zeta \psi_a^{\varepsilon_i} \psi_b^{\varepsilon_j} d\zeta \quad (4.12)$$

$$+ (-1)^{(i+j)} \frac{\alpha_{\zeta 1}}{|\zeta|^{\beta_1}} \int_\zeta \nabla \psi_a^{\varepsilon_i} \cdot (\mathbf{N}_\zeta \otimes \mathbf{N}_\zeta) \cdot \nabla \psi_b^{\varepsilon_j} d\zeta \quad (4.13)$$

for all $i, j = 1, 2$, and $a = 1, \dots, N_{bf}^{\varepsilon_i}$, $b = 1, \dots, N_{bf}^{\varepsilon_j}$. For the remainder of our discussions, we will consider only the case where $f_{\mathcal{E}} \equiv 0$ for all sub-elements $\mathcal{E} \subset \Omega$.

For a given d -dimensional sub-element \mathcal{E} , the assembly of the above terms entails an entity-wise integration of products between basis functions (and their gradients) over d -dimensional entities $\varepsilon \in \mathcal{T}_\varepsilon(\mathcal{E})$ and their $(d-1)$ -dimensional children $\zeta \in \Gamma_\varepsilon \cup \partial\mathcal{E}$. This may be effected through the use of appropriately defined quadrature rules on each entity, or by pre-computing the monomial integrals over each entity up to some sufficiently high degree (nominally $2k$).

Additionally, it is remarked that the boundary condition $\bar{\varphi}$ is defined independently on every $(d-1)$ -dimensional sub-element $e \subset \partial\mathcal{E}$, such that its restriction $\bar{\varphi}|_\zeta$ may be written in terms of the local basis functions $\{\psi_c^\zeta\}_{c=1}^{N_{bf}^\zeta}$ belonging to a given boundary entity $\zeta \in \mathcal{T}_\zeta(e)$, i.e.

$$\bar{\varphi}|_\zeta(\mathbf{X}) = \sum_{c=1}^{N_{bf}^\zeta} \psi_c^\zeta(\mathbf{X}) \bar{\varphi}_c. \quad (4.14)$$

For a given $\zeta \in \partial\mathcal{E}$, this yields:

$$F_b^\varepsilon = \sum_{c=1}^{N_{bf}^\zeta} \bar{J}_{bc}^\varepsilon \bar{\varphi}_c \quad \forall b = 1, \dots, N_{bf}^\varepsilon, \quad (4.15)$$

which may be used in lieu of (4.10), where

$$\bar{J}_{bc}^\varepsilon = \int_\zeta \epsilon (\mathbf{N}_\zeta \cdot \nabla \psi_b^\varepsilon) \psi_c^\zeta d\zeta + \frac{\alpha_{\zeta 0}}{|\zeta|^{\beta_0}} \int_\zeta \psi_c^\zeta \psi_b^\varepsilon d\zeta \quad \forall b = 1, \dots, N_{bf}^\varepsilon, c = 1, \dots, N_{bf}^\zeta. \quad (4.16)$$

Consequently, we may re-write the right-hand side of (4.6) as a linear mapping from the basis coefficients $\bar{\varphi}_C$ which determine the boundary function $\bar{\varphi}(\mathbf{X}) = \sum_{C=1}^{N_{bf}^{\partial\mathcal{E}}} \psi_C(\mathbf{X}) \bar{\varphi}_C$:

$$\sum_{A=1}^{N_{bf}^{\mathcal{E}}} J_{AB} \varphi_A = \sum_{C=1}^{N_{bf}^{\partial\mathcal{E}}} \bar{J}_{BC} \bar{\varphi}_C \quad \forall B = 1, \dots, N_{bf}^{\mathcal{E}}. \quad (4.17)$$

Alternatively, in matrix-vector format:

$$\mathbf{J} \boldsymbol{\varphi} = \bar{\mathbf{J}} \bar{\boldsymbol{\varphi}}. \quad (4.18)$$

The above system of equations can be solved to obtain a linear mapping from $\bar{\boldsymbol{\varphi}}$ to $\boldsymbol{\varphi}$, denoted $\mathbf{M}^{\partial\mathcal{E} \mapsto \mathcal{E}} = \mathbf{J}^{-1} \bar{\mathbf{J}} : \mathbb{R}^{N_{bf}^{\partial\mathcal{E}}} \mapsto \mathbb{R}^{N_{bf}^{\mathcal{E}}}$. This mapping may be utilized to define the shape functions in a recursive fashion (over the children of each sub-element, in succession), ultimately yielding a representation for the shape functions on \mathcal{E} in terms of only nodal evaluations $\varphi|_V$. This process is discussed in greater detail in the following section.

Hierarchical Construction of Shape Functions

For a given polyhedral element $\Omega \subset \mathbb{R}^d$, we presume that each shape function φ_A is associated with a particular node V_A of the element, such that

$$\varphi_A|_{V_B} = \delta_{AB} \quad \forall A, B = 1, \dots, N_V^\Omega. \quad (4.19)$$

Additionally, for the sake of simplicity (and computational efficiency), it is suggested that the shape functions along each linear edge E be constructed from the standard Lagrange polynomials which interpolate the nodal values of that edge.

For each polygonal face F , linear mappings $\mathbf{M}^{\partial F \mapsto F} : \mathbb{R}^{N_V^F} \mapsto \mathbb{R}^{N_{bf}^F}$ may be constructed according to the process described in the previous section, yielding

$$\varphi_A|_F(\mathbf{X}) = \sum_{b=1}^{N_{bf}^F} \sum_{c=1}^{N_V^F} \psi_b(\mathbf{X}) M_{bc}^{\partial F \mapsto F} \varphi_A|_{V_c}. \quad (4.20)$$

Subsequently, a mapping $\mathbf{M}^{\partial\Omega \mapsto \Omega} : \mathbb{R}^{N_{bf}^{\partial\Omega}} \mapsto \mathbb{R}^{N_{bf}^\Omega}$ is constructed to determine the representation for the shape functions on the interior of the element, which may be composed with the mappings $\mathbf{M}^{\partial F \mapsto F}$ for each face to determine a final mapping $\mathbf{M}^{V \mapsto \Omega} : \mathbb{R}^{N_V^\Omega} \mapsto \mathbb{R}^{N_{bf}^\Omega}$ which yields

$$\varphi_A|_\Omega(\mathbf{X}) = \sum_{b=1}^{N_{bf}^\Omega} \sum_{c=1}^{N_V^\Omega} \psi_b(\mathbf{X}) M_{bc}^{V \mapsto \Omega} \varphi_A|_{V_c}. \quad (4.21)$$

Once the above representations for the element's shape function have been obtained, the discrete data required of the element (evaluations of the shape functions and their gradients at a discrete number of quadrature points $\{\mathbf{X}_q\}_{q=1}^{N_{qp}}$) can be obtained through direct evaluation of (4.21), i.e.

$$\varphi_A|_\Omega(\mathbf{X}_q) = \sum_{b=1}^{N_{bf}^\Omega} \sum_{c=1}^{N_V^\Omega} \psi_b(\mathbf{X}_q) M_{bc}^{V \rightarrow \Omega} \varphi_A|_{V_c}, \quad (4.22)$$

and

$$\nabla \varphi_A|_\Omega(\mathbf{X}_q) = \sum_{b=1}^{N_{bf}^\Omega} \sum_{c=1}^{N_V^\Omega} \nabla \psi_b(\mathbf{X}_q) M_{bc}^{V \rightarrow \Omega} \varphi_A|_{V_c}. \quad (4.23)$$

Once the discrete quadrature point evaluations for the shape functions have been obtained, there is no need to retain any information regarding the DG-PEM basis functions, or the transitional mappings; these artifacts and their corresponding data structures may therefore be discarded.

The specification of the element's quadrature rule is discussed in the following section.

Construction of Quadrature Rules

The quadrature rule for an element $\{\mathbf{X}_q, w_q\}_{q=1}^{N_{qp}}$ nominally consists of quadrature points \mathbf{X}_q located at the centroids of each cell $\omega \in \mathcal{T}_\omega(\Omega)$, whose corresponding quadrature weights w_q are equal to the volumes of each respective cell $|\omega|$. This results in the composite mid-point rule discussed in chapter 3.

As previously discussed, the volumes $|\omega|$ and centroids $\bar{\mathbf{X}}_\omega$ of each cell may be obtained via the exact integration formulas provided by Chin et al. in [18]. Alternatively, we may exploit the geometric simplicity of the chosen edge-based partitioning scheme to compute these quantities more easily, by considering the fact that each edge-centered cell ω consists of two tetrahedral sub-domains (i.e. $T_1 \cup T_2 = \omega$). Volumes and centroids for each tetrahedron can be easily computed using standard formulas, and the resulting quantities of interest may be expressed as

$$|\omega| = |T_1| + |T_2|, \quad \bar{\mathbf{X}}_\omega = \frac{|T_1|\bar{\mathbf{X}}_{T_1} + |T_2|\bar{\mathbf{X}}_{T_2}}{|\omega|}. \quad (4.24)$$

Straightforward integration rules $\{\mathbf{X}_q, w_q\}_{q=1}^{N_{qp}^F}$ for each face $F \subset \partial\Omega$ are more easily obtained by considering the corresponding areas $|\sigma|$ and centroids $\bar{\mathbf{X}}_\sigma$ of each (strictly

triangular) facet $\sigma \in \mathcal{T}_\sigma(F)$. Outward unit normals \mathbf{N}_σ to each facet may also be readily computed and stored, as needed.

With these quantities in hand, the element's shape functions (and their gradients) may be evaluated at the quadrature points of the element, as described in the previous section. Subsequently, a consistent integration scheme (as discussed in 3) may be constructed from the discrete data stored at the element's quadrature points. If a gradient correction scheme is adopted, the corrected test function gradients $\nabla\phi_A(\mathbf{X}_q)$ at all quadrature points may be computed and stored, as needed.

4.6 Numerical Conditioning of the DG-PEM Systems of Equations

As a representative example, consider a given sub-element $\mathcal{E} \subset \mathbb{R}^d$ and its corresponding partition into d -dimensional entities $\varepsilon \subset \mathcal{T}_\varepsilon(\mathcal{E})$. Recall that the representation of a given shape function $\varphi \in \mathcal{D}_k^h(\mathcal{E})$ is piecewise polynomial in each entity, i.e. $\varphi|_\varepsilon \in P^k(\varepsilon)$.

A reasonable estimate for the condition number $\kappa(\mathbf{J})$ of the SPD matrix \mathbf{J} appearing in (4.18) may be obtained via

$$\frac{\max_a |J_{aa}^\varepsilon|}{\min_a |J_{aa}^\varepsilon|} \leq \kappa(\mathbf{J}), \quad (4.25)$$

where

$$\begin{aligned} J_{aa}^\varepsilon &= \int_\varepsilon \nabla\psi_a^\varepsilon \cdot \nabla\psi_a^\varepsilon d\varepsilon + (\epsilon - 1) \sum_{\zeta \in \partial\varepsilon \cap \partial\mathcal{E}} \int_\zeta (\psi_a^\varepsilon) (\mathbf{N}_\zeta \cdot \nabla\psi_a^\varepsilon) d\zeta \\ &\quad + \frac{1}{2}(\epsilon - 1) \sum_{\zeta \in \partial\varepsilon \cap \Gamma_\varepsilon} \int_\zeta (\psi_a^\varepsilon) (\mathbf{N}_\zeta \cdot \nabla\psi_a^\varepsilon) d\zeta \\ &\quad + \sum_{\zeta \in \partial\varepsilon} \frac{\alpha_{\zeta 0}}{|\zeta|^{\beta_0}} \int_\zeta (\psi_a^\varepsilon)^2 d\zeta + \sum_{\zeta \in \partial\varepsilon \cap \Gamma_\varepsilon} \frac{\alpha_{\zeta 1}}{|\zeta|^{\beta_1}} \int_\zeta (\mathbf{N}_\zeta \cdot \nabla\psi_a^\varepsilon)^2 d\zeta. \end{aligned} \quad (4.26)$$

A brief remark should be made regarding the positivity of J_{aa}^ε , and its relation to the particular choice of DG method (i.e. whether the SIPG, NIPG, or IIPG is chosen). As discussed in [65], the NIPG method with $\epsilon = +1$ will yield strictly positive diagonal entries provided $\alpha_{\zeta 0} > 0$, resulting in the coercivity of \mathbf{J} . If the SIPG ($\epsilon = -1$) or IIPG ($\epsilon = 0$) methods are employed, then the penalty parameters must be made sufficiently large enough to guarantee coercivity, stability.

The subsequent discussion examines the case where $\epsilon = +1$, yielding strictly positive diagonal entries:

$$J_{aa}^\epsilon = \int_\epsilon \nabla \psi_a^\epsilon \cdot \nabla \psi_a^\epsilon d\epsilon + \sum_{\zeta \in \partial\epsilon} \frac{\alpha_{\zeta 0}}{|\zeta|^{\beta_0}} \int_\zeta (\psi_a^\epsilon)^2 d\zeta + \sum_{\zeta \in \partial\epsilon \cap \Gamma_\epsilon} \frac{\alpha_{\zeta 1}}{|\zeta|^{\beta_1}} \int_\zeta (\mathbf{N}_\zeta \cdot \nabla \psi_a^\epsilon)^2 d\zeta. \quad (4.27)$$

Let h_ϵ denote the diameter of ϵ , such that

$$h_\epsilon = \sup_{\mathbf{X}_1, \mathbf{X}_2 \in \epsilon} \|\mathbf{X}_1 - \mathbf{X}_2\|_2. \quad (4.28)$$

Using the following trace inequalities:

$$\int_\zeta (\psi_a^\epsilon)^2 d\zeta \leq Ch_\epsilon^{-1/2} \int_\epsilon (\psi_a^\epsilon)^2 d\epsilon \quad \forall \zeta \subset \partial\epsilon, \quad (4.29)$$

$$\int_\zeta (\mathbf{N}_\zeta \cdot \nabla \psi_a^\epsilon)^2 d\zeta \leq Ch_\epsilon^{-1/2} \int_\epsilon \nabla \psi_a^\epsilon \cdot \nabla \psi_a^\epsilon d\epsilon \quad \forall \zeta \subset \partial\epsilon, \quad (4.30)$$

and observing that $|\zeta|^{\beta_0} \leq h_\epsilon$, $|\zeta|^{\beta_1} \geq h_\epsilon^{-1}$ if $\beta_0 = (d-1)^{-1}$, $\beta_1 = -(d-1)^{-1}$ (assuming $h_\epsilon \geq 1$, without loss of generality), then

$$J_{aa}^\epsilon \leq (1 + C_1 h_\epsilon^{1/2}) \int_\epsilon \nabla \psi_a^\epsilon \cdot \nabla \psi_a^\epsilon d\epsilon + C_2 h_\epsilon^{-3/2} \int_\epsilon (\psi_a^\epsilon)^2 d\epsilon, \quad (4.31)$$

for some $C_1, C_2 \in \mathbb{R}$.

If $\varphi|_\epsilon$ is represented in terms of the (unshifted and unscaled) monomial basis (i.e. $\{\varphi_a^\epsilon\}_{a=1}^{N_{bf}^\epsilon} = \{\mathbf{X}^\alpha\}_{|\alpha| \leq k}$), then by application of the max-min inequality:

$$\int_\epsilon \mathbf{X}^{2\alpha} d\epsilon \leq h_\epsilon^d \max_{\mathbf{X} \in \epsilon} \{\mathbf{X}^{2\alpha}\} \leq h_\epsilon^d R_\epsilon^{2|\alpha|}, \quad (4.32)$$

$$\int_\epsilon \nabla \mathbf{X}^\alpha \cdot \nabla \mathbf{X}^\alpha d\epsilon \leq h_\epsilon^d \max_{\mathbf{X} \in \epsilon} \{\nabla \mathbf{X}^\alpha \cdot \nabla \mathbf{X}^\alpha\} \leq h_\epsilon^d R_\epsilon^{2\langle |\alpha|-1 \rangle}, \quad (4.33)$$

where it is assumed that

$$R_\epsilon = \max_{\mathbf{X} \in \epsilon} \|\mathbf{X}\|_2, \quad (4.34)$$

and $R_\epsilon \geq 1$, without loss of generality. Under these conditions, it suffices to assert that $\exists C > 0$ which may be used to establish a uniform lower bound on J_{aa}^ϵ , such that

$$C [(h_\epsilon^d + C_1 h_\epsilon^{d+1/2}) + C_2 h_\epsilon^{d-3/2}] \leq J_{aa}^\epsilon \leq (h_\epsilon^d + C_1 h_\epsilon^{d+1/2}) R_\epsilon^{2\langle k-1 \rangle} + C_2 h_\epsilon^{d-3/2} R_\epsilon^{2k}. \quad (4.35)$$

If the penalty parameter $\alpha_{\gamma 0}$ is sufficiently small, we obtain the estimate $\kappa(\mathbf{J}) \approx O(R_{\max}^{2(k-1)})$, where $R_{\max} = \max \{\max_{\varepsilon \in \mathcal{E}} R_\varepsilon, \max_{\varepsilon \in \mathcal{E}} R_\varepsilon^{-1}\}$. Otherwise, if $\alpha_{\gamma 0}$ is sufficiently large, then $\kappa(\mathbf{J}) \approx O(R_{\max}^{2k})$; a similar estimate may be obtained for the SIPG and IIPG methods. The latter estimate is also applicable to the pure penalty DG-PEM, provided sufficient stability is supplied by the inclusion of additional penalty terms (3.43).

Clearly, the condition number of \mathbf{J} under these circumstances may become unacceptably large for increasing values of k and R_{\max} , leading to numerical inaccuracies in the resulting shape functions. This can ultimately degrade the degree of precision achieved in finite element patch tests.

To mitigate this issue, the (sub-)element's shape functions may be computed with respect to a shifted and scaled coordinate system, e.g. $\mathbf{X}' = h_\varepsilon^{-1}(\mathbf{X} - \bar{\mathbf{X}}_0^\varepsilon)$, where

$$h_\varepsilon = \sup_{\mathbf{X}_1, \mathbf{X}_2 \in \varepsilon} \|\mathbf{X}_1 - \mathbf{X}_2\|_2. \quad (4.36)$$

This assists in limiting the worst-case value of R_{\max} appearing in the previous estimate, yielding a somewhat improved bound on the condition number: $\kappa(\mathbf{J}) \approx O(\rho^{2k})$. We define $\rho = h_\varepsilon/h_{\min}$, and

$$h_{\min} = \inf_{\varepsilon \in \mathcal{T}_\varepsilon(\mathcal{E})} \sup_{B_r(\mathbf{X}_B) \subset \varepsilon} |2r| \quad (4.37)$$

denotes the smallest diameter of the largest ball $B_r(\mathbf{X}_B) = \{\mathbf{X} \in \mathbb{R}^d : \|\mathbf{X} - \mathbf{X}_B\|_2 \leq r\}$ fully contained within any single entity $\varepsilon \in \mathcal{T}_\varepsilon(\mathcal{E})$. Nonetheless, the condition number of \mathbf{J} can become large if: a relatively refined partition of the element is utilized; if the aspect ratio of the element becomes large; or if the element's partition contains “sliver cells” (i.e. if an edge-based partition is employed on an element with nearly degenerate geometric features.) Some improvements in the conditioning of \mathbf{J} may be obtained by considering the DG basis described in [9]. The Lagrange polynomials (for triangles and tetrahedra) can also be used to obtain well-scaled bases for each entity.

Chapter 5

A Numerical Evaluation of the PEM

This chapter provides a detailed numerical assessment of several partitioned element methods, with specific emphasis placed upon the DG-PEM. A numerical measure of polynomial reproducibility is introduced and utilized to investigate the level of interpolation error incurred by different formulations of the PEM. Linear and quadratic finite element patch tests are conducted in both 2- and 3-dimensions, with comparisons drawn between the FEM and the PEM. The behavior of irregularly-shaped polygonal elements is investigated, and the effects of short element edges within 2-dimensional Voronoi meshes are examined further. Convergence studies are carried out to compare the accuracy of the PEM with that of the FEM. The chapter concludes with a number of demonstrative problems, illustrating the ability of the PEM to accommodate finite deformations and elasto-plastic material behavior.

5.1 Tests for Polynomial Reproducibility

Herein, an investigation is conducted to assess the degree to which polynomial reproducibility is achieved by a given partitioned element methodology. Reproducibility is assessed by an *interpolation error* metric, defined in the following section.

Interpolation Error

Consider an arbitrary polytopal element $\Omega \subset \mathbb{R}^d$. Let $u \in P^k(\Omega)$ denote a scalar polynomial field of maximal degree k , written in terms of the monomials:

$$u(\mathbf{X}) = \sum_{|\alpha| \leq k} c_\alpha \mathbf{X}^\alpha. \quad (5.1)$$

The $H^1(\Omega)$ norm of any scalar field $u \in H^1(\Omega)$ is denoted

$$\|u\|_{H^1} = [\langle u, u \rangle_{H^1}]^{1/2}, \quad (5.2)$$

where

$$\langle u, v \rangle_{H^1} = \int_{\Omega} (u v + u_{,i} v_{,i}) d\Omega \quad (5.3)$$

is the $H^1(\Omega)$ inner product of $u, v \in H^1(\Omega)$. Denote u^h as the approximate representation of u over Ω using the element's shape functions $\{\varphi_A\}_{A=1}^{N_V^\Omega}$:

$$u^h(\mathbf{X}) = \sum_{A=1}^{N_V^\Omega} \varphi_A(\mathbf{X}) u(\mathbf{X}_A). \quad (5.4)$$

Recall that the space of all polynomials of maximal degree k is denoted $P^k(\Omega)$. The sub-space $\bar{P}^k(\Omega) \subset P^k(\Omega)$ contains only those polynomials with unit $H^1(\Omega)$ norm:

$$\bar{P}^k(\Omega) = \{u : u \in P^k(\Omega), \|u\|_{H^1} = 1\}. \quad (5.5)$$

The *interpolation error* $E_k(\Omega)$ on the element Ω over the polynomials of maximal degree k is defined as

$$E_k(\Omega) \equiv \sup_{u \in \bar{P}^k(\Omega)} \|u(\mathbf{X}) - u^h(\mathbf{X})\|_{H^1} = \sup_{u \in P^k(\Omega)} \frac{\|u(\mathbf{X}) - u^h(\mathbf{X})\|_{H^1}}{\|u(\mathbf{X})\|_{H^1}}. \quad (5.6)$$

In the numerical computation of this error measure, the polynomial coefficients c_α of $u \in \bar{P}^k(\Omega)$ which yield the maximal error must be determined. Denote e_α as the error in the approximation of the monomial \mathbf{X}^α :

$$e_\alpha = \mathbf{X}^\alpha - \sum_{A=1}^{N_V^\Omega} \varphi_A(\mathbf{X}) \mathbf{X}_A^\alpha. \quad (5.7)$$

Consequently,

$$[E_k(\Omega)]^2 = \max_{c_\gamma} \sum_{|\alpha| \leq k} \sum_{|\beta| \leq k} c_\alpha c_\beta \langle e_\alpha, e_\beta \rangle_{H^1}, \quad (5.8)$$

subject to the constraint

$$g(c_\gamma) = 1 - \sum_{|\alpha| \leq k} \sum_{|\beta| \leq k} c_\alpha c_\beta \langle \mathbf{X}^\alpha, \mathbf{X}^\beta \rangle_{H^1} = 0. \quad (5.9)$$

Using the method of Lagrange multipliers, we may rewrite the above constrained optimization problem as

$$[E_k(\Omega)]^2 = \max_{c_\gamma, \lambda} \Lambda(c_\gamma, \lambda), \quad (5.10)$$

where $\Lambda(c_\gamma, \lambda)$ is the Lagrangian:

$$\Lambda(c_\gamma, \lambda) = \max_{c_\gamma} \sum_{|\alpha| \leq k} \sum_{|\beta| \leq k} c_\alpha c_\beta \langle e_\alpha, e_\beta \rangle_{H^1} + \lambda g(c_\gamma). \quad (5.11)$$

Observe that

$$\frac{\partial}{\partial \lambda} \Lambda(c_\gamma, \lambda) = g(c_\gamma) = 0, \quad (5.12)$$

and

$$\frac{\partial}{\partial c_\gamma} \Lambda(c_\gamma, \lambda) = \sum_{|\alpha| \leq k} \sum_{|\beta| \leq k} \frac{\partial}{\partial c_\gamma} (c_\alpha c_\beta) \langle e_\alpha, e_\beta \rangle_{H^1} + \lambda \frac{\partial}{\partial c_\gamma} g(c_\gamma) = 0. \quad (5.13)$$

This yields

$$\sum_{|\alpha| \leq k} c_\alpha [\langle e_\alpha, e_\gamma \rangle_{H^1} - \lambda \langle \mathbf{X}^\alpha, \mathbf{X}^\gamma \rangle_{H^1}] = 0 \quad \forall |\gamma| \leq k, \quad (5.14)$$

or, in matrix-vector notation:

$$(\mathbf{A} - \lambda \mathbf{B}) \mathbf{c} = \mathbf{0}, \quad (5.15)$$

corresponding to the generalized eigenvalue problem, where

$$A_{\alpha\beta} = \langle e_\alpha, e_\beta \rangle_{H^1}, \quad B_{\alpha\beta} = \langle \mathbf{X}^\alpha, \mathbf{X}^\beta \rangle_{H^1}, \quad (5.16)$$

are both real, symmetric matrices. Since \mathbf{B} is positive-definite, we determine that it is invertible, and therefore we may solve the equivalent eigenvalue problem:

$$(\mathbf{B}^{-1} \mathbf{A} - \lambda \mathbf{1}) \mathbf{c} = \mathbf{0}. \quad (5.17)$$

The square root of the maximum eigenvalue λ_{\max} of $\mathbf{B}^{-1}\mathbf{A}$ yields the interpolation error $E_k(\Omega) = \sqrt{\lambda_{\max}}$. This can be seen more directly if we view $[E_k(\Omega)]^2$ to be the generalized Rayleigh quotient of \mathbf{A} and \mathbf{B} :

$$E_k(\Omega) = \max_{\mathbf{c}} \sqrt{\frac{\mathbf{c}^T \mathbf{A} \mathbf{c}}{\mathbf{c}^T \mathbf{B} \mathbf{c}}} = \sqrt{\lambda_{\max}}. \quad (5.18)$$

For simplicity in the numerical computation of $E_k(\Omega)$, we assume that the entries of \mathbf{A} and \mathbf{B} will be computed approximately using the element's quadrature rules, i.e.

$$\langle e_\alpha, e_\beta \rangle_{H^1} \approx \sum_{q=1}^{N_{qp}^\Omega} w_q (e_\alpha^q e_\beta^q + e_{\alpha,i}^q e_{\beta,i}^q), \quad (5.19)$$

$$\langle \mathbf{X}^\alpha, \mathbf{X}^\beta \rangle_{H^1} \approx \sum_{q=1}^{N_{qp}^\Omega} w_q (\mathbf{X}_q^\alpha \mathbf{X}_q^\beta + \mathbf{X}_{q,i}^\alpha \mathbf{X}_{q,i}^\beta), \quad (5.20)$$

where

$$e_\alpha^q = \mathbf{X}_q^\alpha - \sum_{A=1}^{N_V^\Omega} \varphi_A(\mathbf{X}_q) \mathbf{X}_A^\alpha, \quad e_{\alpha,i}^q = \mathbf{X}_{q,i}^\alpha - \sum_{A=1}^{N_V^\Omega} \varphi_{A,i}(\mathbf{X}_q) \mathbf{X}_A^\alpha. \quad (5.21)$$

If a given element is capable of reproducing all polynomials up to degree k , then clearly $E_k(\Omega) = 0$. This property is used to verify that the shape function approximations obtained via a particular formulation of the PEM satisfy the requirements of polynomial reproducibility.

Verification of Polynomial Reproducibility for PEM Elements

Through a series of numerical experiments, it is confirmed that both the CG-PEM and the DG-PEM satisfy the requirements of polynomial reproducibility. Particular attention is paid to low-order PEM elements (i.e. $k = 1$), where satisfaction of the condition $E_1(\Omega) = 0$ is sufficient to demonstrate reproducibility for a given element Ω .

Consider the arbitrary polygonal element and its corresponding edge-based partition illustrated in Figure 5.1. The harmonic shape functions defined on this partitioned element were approximated using the CG-PEM and the DG-PEM. Unless otherwise noted, the NIPG version of the DG-PEM ($\epsilon = +1$) was utilized throughout.

For the partitioned element under consideration, the interpolation error of order $k = 1$ for the CG-PEM was computed as $E_1(\Omega) = 2.5465 \times 10^{-16}$ (on the order of machine

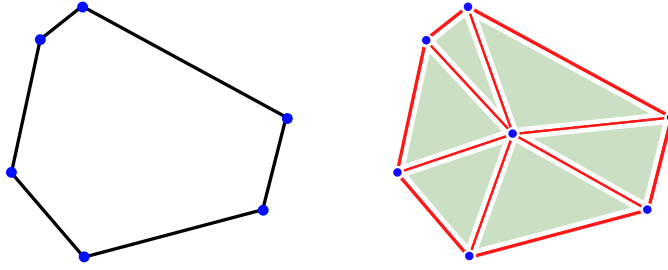


Figure 5.1: A representative polygonal element and its corresponding edge-based partition.

$E_1(\Omega)$	$\alpha_{\gamma 0} = 10^{-3}$	$\alpha_{\gamma 0} = 10^0$	$\alpha_{\gamma 0} = 10^3$	$\alpha_{\gamma 0} = 10^6$
$\alpha_{\gamma 1} = 0.0$	1.66E-013	7.48E-016	4.70E-014	1.79E-010
$\alpha_{\gamma 1} = 10^0$	1.65E-013	9.67E-016	8.73E-015	2.51E-011
$\alpha_{\gamma 1} = 10^3$	1.01E-012	2.66E-013	1.36E-015	4.49E-014
$\alpha_{\gamma 1} = 10^6$	1.13E-009	3.13E-010	7.10E-013	9.03E-016

(a) Interpolation error: $E_1(\Omega)$

$\kappa(\mathbf{J})$	$\alpha_{\gamma 0} = 10^{-3}$	$\alpha_{\gamma 0} = 10^0$	$\alpha_{\gamma 0} = 10^3$	$\alpha_{\gamma 0} = 10^6$
$\alpha_{\gamma 1} = 0.0$	5.44E+002	4.07E+000	5.94E+003	5.96E+006
$\alpha_{\gamma 1} = 10^0$	4.96E+003	2.01E+001	9.33E+002	9.29E+005
$\alpha_{\gamma 1} = 10^3$	1.58E+007	2.50E+004	6.96E+001	1.11E+003
$\alpha_{\gamma 1} = 10^6$	2.37E+010	2.50E+007	6.86E+004	6.98E+001

(b) DG-PEM linear system conditioning: $\kappa(\mathbf{J})$

Table 5.1: Computed values of $E_1(\Omega)$ and $\kappa(\mathbf{J})$ for the element in Figure 5.1, using various DG-PEM penalty parameter settings.

precision). For the DG-PEM, the interpolation error was observed to be dependent upon the accuracy of the computations performed in solving the linear system of equations in (4.18). The log of $\kappa(\mathbf{J})$ provides a useful indicator of the number of digits of precision lost in computing \mathbf{J}^{-1} . This loss of precision is reflected by a corresponding increase in the interpolation error measure. Table 5.1 illustrates the connection between $E_1(\Omega)$ and $\kappa(\mathbf{J})$ for various DG-PEM penalty parameter values.

The results in table 5.1 confirm that \mathbf{J} will become poorly conditioned if either of the two penalty parameters $\alpha_{\gamma 0}$ or $\alpha_{\gamma 1}$ are sufficiently large. This is true regardless of how the

$E_1(\Omega)$	$\alpha_{\gamma 0} = 10^{-3}$	$\alpha_{\gamma 0} = 10^0$	$\alpha_{\gamma 0} = 10^3$	$\alpha_{\gamma 0} = 10^6$
$\alpha_{\gamma 1} = 0.0$	3.02E-014	9.01E-015	5.22E-013	1.59E-009
$\alpha_{\gamma 1} = 10^0$	3.99E-014	1.37E-014	2.02E-013	3.12E-012
$\alpha_{\gamma 1} = 10^3$	2.44E-011	6.48E-012	1.89E-012	3.34E-013
$\alpha_{\gamma 1} = 10^6$	1.52E-007	4.97E-008	1.85E-009	3.69E-012

(a) Interpolation error: $E_1(\Omega)$

$\kappa(\mathbf{J})$	$\alpha_{\gamma 0} = 10^{-3}$	$\alpha_{\gamma 0} = 10^0$	$\alpha_{\gamma 0} = 10^3$	$\alpha_{\gamma 0} = 10^6$
$\alpha_{\gamma 1} = 0.0$	9.07E+003	1.39E+002	1.14E+005	1.33E+008
$\alpha_{\gamma 1} = 10^0$	3.52E+005	1.75E+003	1.97E+004	3.67E+005
$\alpha_{\gamma 1} = 10^3$	1.17E+009	2.46E+006	2.61E+005	2.32E+004
$\alpha_{\gamma 1} = 10^6$	1.77E+012	2.45E+009	2.52E+008	3.07E+005

(b) DG-PEM linear system conditioning: $\kappa(\mathbf{J})$ Table 5.2: Computed values of $E_1(\Omega)$ and $\kappa(\mathbf{J})$ for a comparatively thin element with an aspect ratio of 100:1, using various DG-PEM penalty parameter settings.

DG polynomial bases are specified for each geometric entity. Under certain circumstances, \mathbf{J} will remain well-conditioned if both $\alpha_{\gamma 0}$ and $\alpha_{\gamma 1}$ are kept roughly proportional to one another, for all values of $\alpha_{\gamma 0}, \alpha_{\gamma 1} > 0$. If $\alpha_{\gamma 0}$ and $\alpha_{\gamma 1}$ are increased proportionally to one another, one recovers the behavior of the pure penalty DG-PEM in (3.42).

Other factors which impact the condition number of \mathbf{J} (such as element shape) may therefore lead to increased interpolation errors. Specifically, consider the case where the element in Figure 5.1 is scaled anisotropically by a factor of 0.01 in the vertical direction, yielding a comparatively thin element with an aspect ratio of 100:1. For this element, the interpolation error using the CG-PEM increases only slightly, to $E_1(\Omega) = 6.9817 \times 10^{-15}$. The corresponding values of $E_1(\Omega)$ and $\kappa(\mathbf{J})$ for the DG-PEM are presented in table 5.2.

Careful selection of $\alpha_{\gamma 0}$ and $\alpha_{\gamma 1}$ is warranted for the sake of minimizing the resulting interpolation error. For general applications in which an edge-based partitioning scheme is employed, it is suggested that the parameter values be chosen such that $\alpha_{\gamma 0} = 10.0$ and $\alpha_{\gamma 1} = 0.0$. Nonetheless, a more thorough parameter sensitivity analysis is recommended.

5.2 Finite Element Patch Tests

Several finite element patch tests for CG-PEM and DG-PEM elements are investigated. The tests are similar to the ones introduced by Irons in the Appendix of [10]. Passage of such tests is argued to be a necessary and sufficient condition for convergence [80], though this claim has been disputed, namely by Stummel in [73]. Nonetheless, patch tests are useful indicators of the expected convergence properties for conforming finite elements. Linear and quadratic patch tests in both 2- and 3-dimensions are considered.

Patch test errors were measured in terms of the normalized $L^2(\Omega)$ error metrics for displacement and stress:

$$\frac{\|\mathbf{u}^h - \mathbf{u}\|}{\|\mathbf{u}\|} = \sqrt{\frac{\int_{\mathcal{B}_0} (\mathbf{u}^h - \mathbf{u}) \cdot (\mathbf{u}^h - \mathbf{u}) dV}{\int_{\mathcal{B}_0} \mathbf{u} \cdot \mathbf{u} dV}}, \quad (5.22)$$

$$\frac{\|\boldsymbol{\sigma}^h - \boldsymbol{\sigma}\|}{\|\boldsymbol{\sigma}\|} = \sqrt{\frac{\int_{\mathcal{B}_0} (\boldsymbol{\sigma}^h - \boldsymbol{\sigma}) : (\boldsymbol{\sigma}^h - \boldsymbol{\sigma}) dV}{\int_{\mathcal{B}_0} \boldsymbol{\sigma} : \boldsymbol{\sigma} dV}}, \quad (5.23)$$

where \mathbf{u} and $\boldsymbol{\sigma}$ denote the exact solutions for the displacement and stress fields, respectively.

For all of the tests considered, both the CG-PEM and DG-PEM utilized an edge-based partitioning scheme and composite mid-point quadrature rules for each element. Unless otherwise noted, the parameters for the DG-PEM were selected as $\epsilon = +1$, $\alpha_{\gamma 0} = 10.0$, and $\alpha_{\gamma 1} = 0.0$. Further, the DG-PEM was tested both with and without using the gradient correction scheme presented in [79]. These corrections were applied to the test function gradients alone (yielding a “nonsymmetric correction” scheme), or to both the trial and test function gradients (yielding a “symmetric correction” scheme).

Linear Patch Tests in 2D

The linear patch test consists of a square patch of elements with dimensions $L \times L$, as shown in Figure 5.2. The normal components of displacement on the $-X_1$ and $-X_2$ faces of the patch are constrained such that

$$u_1(X_1 = 0) = 0, \quad u_2(X_2 = 0) = 0. \quad (5.24)$$

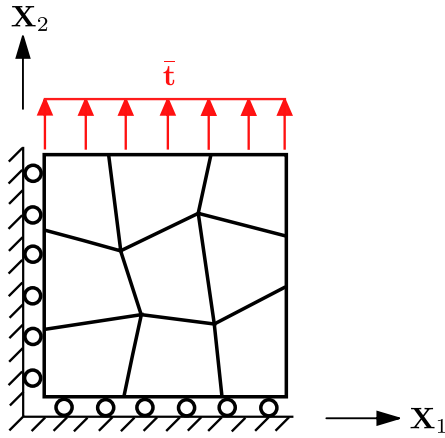


Figure 5.2: Depiction of the 2D linear patch test.

A constant vertical traction $\bar{\mathbf{t}} = (0, T)$ is prescribed on the $+X_2$ face of the patch. For a linear elastic body under plane strain conditions, an exact solution for the in-plane displacement and stress fields is easily obtained:

$$u_1(\mathbf{X}) = -\frac{\nu}{2\mu}TX_1, \quad u_2(\mathbf{X}) = \frac{(1-\nu)}{2\mu}TX_2, \quad (5.25)$$

$$\sigma_{11}(\mathbf{X}) = \sigma_{12}(\mathbf{X}) = 0, \quad \sigma_{22}(\mathbf{X}) = T. \quad (5.26)$$

The two meshes depicted in Figure 5.3 are considered. The PEM was used on the polygonal mesh, whereas the FEM with standard 4-nodes isoparametric elements was used on the quadrilateral mesh.

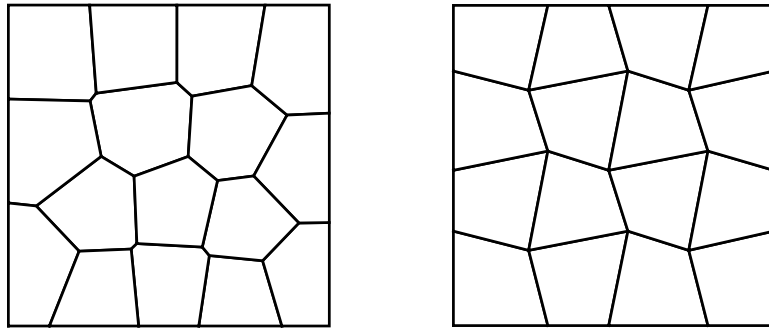


Figure 5.3: Meshes used for the linear patch test: (left) polygonal mesh, (right) distorted quadrilateral mesh.

Linear patch test errors for the FEM, CG-PEM, and DG-PEM are explored. The results of these tests may be found in table 5.3.

	$\ \mathbf{u}^h - \mathbf{u}\ /\ \mathbf{u}\ $	$\ \boldsymbol{\sigma}^h - \boldsymbol{\sigma}\ /\ \boldsymbol{\sigma}\ $
FEM (4-node quadrilaterals)	5.1568E-015	7.7395E-016
CG-PEM (no gradient correction)	5.9125E-012	5.1637E-012
DG-PEM (no gradient correction)	2.7721E-005	3.0904E-004
DG-PEM (symmetric correction)	6.2750E-012	5.3521E-012
DG-PEM (nonsymmetric correction)	6.2673E-012	5.3494E-012

Table 5.3: Linear patch test results comparison for FEM, CG-PEM, and DG-PEM.

The classical FEM produces errors on the order of machine precision. The CG-PEM produces results that are only slightly less accurate. As confirmed by (3.33), the integration errors for the CG-PEM are negligible, and the resulting patch test errors are unaffected by the use (or disuse) of a gradient correction scheme. In contrast, the DG-PEM produces noticeable errors if no gradient correction scheme is employed. Using either of the symmetric or nonsymmetric gradient correction schemes with the DG-PEM yields comparable accuracy to the CG-PEM.

These observations help to illuminate an important point regarding integration consistency. Consider the consistency equations in (2.65). It is remarked that any continuous field $\varphi_a \in C^0(\Omega_e)$ integrated exactly in (2.65) will lead to direct satisfaction of quadrature consistency. Such is the case for linear CG-PEM elements. However, if φ_a is not a continuous field, neither (2.65) nor quadrature consistency will be satisfied, in general. Such is the case for the DG-PEM, even if exact integration is used. The consequence is violation of patch tests. This can be mitigated through the use of a gradient correction scheme, or alternatively through an appropriate selection of the DG-PEM parameters. Specifically, in the limit as $\alpha_{\gamma_0} \rightarrow \infty$, the DG-PEM reduces to the CG-PEM, and the resulting patch test errors can be eliminated. Table 5.4 demonstrates this behavior for increasing values of α_{γ_0} , in the absence of a gradient correction scheme.

Additionally, it is noted that the DG-PEM recovers integration consistency in the limit as $\alpha_{\gamma_0} \rightarrow 0$. This is a direct consequence of (3.50). It is tempting to want to specify α_{γ_0} to be sufficiently small/large enough to reduce patch test errors to an acceptable

DG-PEM	$\alpha_{\gamma 0} = 10^{-6}$	$\alpha_{\gamma 0} = 10^{-3}$	$\alpha_{\gamma 0} = 10^0$	$\alpha_{\gamma 0} = 10^3$	$\alpha_{\gamma 0} = 10^6$
$\alpha_{\gamma 1} = 0.0$	2.8433E-009	2.8152E-006	3.3114E-004	4.8035E-006	4.8278E-009
$\alpha_{\gamma 1} = 10^{-3}$	2.8505E-009	2.8224E-006	3.2288E-004	4.9805E-006	5.0082E-009
$\alpha_{\gamma 1} = 10^0$	3.4853E-009	3.4604E-006	2.4827E-003	7.4284E-004	8.6376E-007
$\alpha_{\gamma 1} = 10^3$	3.5460E-009	3.5450E-006	3.0047E-003	1.3898E-002	7.4705E-004
$\alpha_{\gamma 1} = 10^6$	3.5457E-009	3.5456E-006	3.0054E-003	1.4604E-002	1.3953E-002

Table 5.4: Computed values of $\|\boldsymbol{\sigma}^h - \boldsymbol{\sigma}\|/\|\boldsymbol{\sigma}\|$ for the DG-PEM using various penalty parameter settings. No gradient correction scheme was utilized. Identical trends were observed for $\|\mathbf{u}^h - \mathbf{u}\|/\|\mathbf{u}\|$.

level. However, this thinking must be tempered by an understanding of the effects of interpolation error on patch test errors. Recall that the interpolation error $E_1(\Omega)$ for a given element is controlled largely by the conditioning of \mathbf{J} . In turn, $\kappa(\mathbf{J})$ will be adversely affected by sufficiently small/large values of $\alpha_{\gamma 0}$. Table 5.5 demonstrates the consequent limitations imposed upon the choice of $\alpha_{\gamma 0}$ due to excessive interpolation error.

DG-PEM	$\kappa(\mathbf{J})$	$E_1(\Omega)$	$\ \mathbf{u}^h - \mathbf{u}\ /\ \mathbf{u}\ $	$\ \boldsymbol{\sigma}^h - \boldsymbol{\sigma}\ /\ \boldsymbol{\sigma}\ $
$\alpha_{\gamma 0} = 10^0$	4.3653E+000	3.7339E-015	3.9872E-005	3.3113E-004
$\alpha_{\gamma 0} = 10^3$	6.1670E+003	2.5645E-012	3.5373E-007	4.8035E-006
$\alpha_{\gamma 0} = 10^6$	6.1816E+006	2.2129E-009	3.5767E-010	4.8276E-009
$\alpha_{\gamma 0} = 10^9$	6.1817E+009	1.6471E-006	1.4331E-009	2.4472E-008
$\alpha_{\gamma 0} = 10^{12}$	6.1821E+012	1.7678E-003	2.1612E-006	3.0495E-005

Table 5.5: The effects of interpolation error on patch test errors in the DG-PEM. No gradient correction scheme was utilized.

If the interpolation error $E_1(\Omega)$ becomes large enough (due to poor conditioning of \mathbf{J}), it will dominate any other sources of error incurred in the patch test. Moreover, interpolation errors persist even if a gradient correction scheme is employed, and can become particularly troublesome for: thin elements, higher-order elements, or elements with nearly degenerate features.

Linear Patch Tests in 3D

For the linear patch test described in the previous example, a fairly straightforward extension to the case of 3-dimensions is obtained by considering a cube of dimensions $L \times L \times L$ with normal displacements constrained on its $-X_1$, $-X_2$, and $-X_3$ faces:

$$u_1(X_1 = 0) = 0, \quad u_2(X_2 = 0) = 0, \quad u_3(X_3 = 0) = 0. \quad (5.27)$$

A constant vertical traction $\bar{\mathbf{t}} = (0, 0, T)$ is prescribed on the $+X_3$ face of the patch. For a linear elastic body, the exact solution is:

$$u_1(\mathbf{X}) = -\frac{\nu}{E}TX_1, \quad u_2(\mathbf{X}) = -\frac{\nu}{E}TX_2, \quad u_3(\mathbf{X}) = \frac{T}{E}X_3, \quad (5.28)$$

$$\sigma_{33}(\mathbf{X}) = T, \quad \text{all other } \sigma_{ij}(\mathbf{X}) = 0. \quad (5.29)$$

The two hexahedral meshes depicted in Figure 5.4 were used in conjunction with the FEM, whereas the DG-PEM was used on the polyhedral mesh depicted in Figure 5.5. The DG-PEM parameter settings were consistent with those used for the 2D patch test. The results are displayed in Table 5.6.

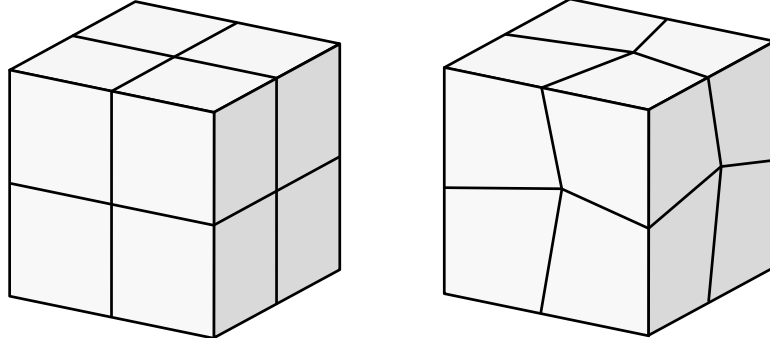


Figure 5.4: Hexahedral meshes: (left) regular, (right) distorted.

It is interesting to note that the FEM incurs mild errors on the distorted hexahedral mesh. Given that the elements' interpolation error remains unchanged, this error is partially attributable to inaccuracies in the numerical integration used for the elements. Using higher-order Gaussian product rules on the isoparametric elements and their faces reduces patch test errors to a limited extent. Nonetheless, some residual errors still remain.

In contrast, the accuracy of the DG-PEM appears to be limited more by interpolation error. As before, these errors are attributable to poor conditioning of the DG-PEM

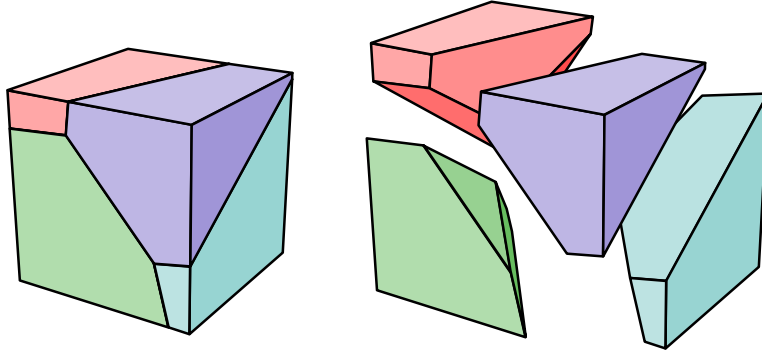


Figure 5.5: Patch of polyhedral elements.

	$E_1(\Omega)$	$\ \mathbf{u}^h - \mathbf{u}\ /\ \mathbf{u}\ $	$\ \boldsymbol{\sigma}^h - \boldsymbol{\sigma}\ /\ \boldsymbol{\sigma}\ $
FEM (regular hexahedra)	2.4441E-016	1.5371E-015	8.1102E-016
FEM (distorted hexahedra)	3.4394E-016	7.5402E-011	1.6047E-010
DG-PEM (no gradient correction)	2.0369E-008	2.7189E-001	4.4846E-001
DG-PEM (symmetric correction)	4.1522E-008	1.2598E-008	4.1608E-008
DG-PEM (nonsymmetric correction)	2.0369E-008	1.0193E-008	2.9253E-008

Table 5.6: 3D linear patch test results comparison for FEM and DG-PEM.

systems of equations. The current evidence suggests that the conditioning of \mathbf{J} becomes worse in higher spatial dimensions. The use of either the symmetric or nonsymmetric gradient correction scheme assists in restoring integration consistency, yielding patch test errors on the order of $E_1(\Omega)$.

Quadratic Patch Tests in 2D

Like the linear patch test, the quadratic patch test considers a similarly constrained square patch of elements, as depicted in Figure 5.6. A constant body force $\mathbf{b} = (b_1, b_2)$ acts uniformly over the patch. Additionally, linearly varying tractions are applied to the unconstrained faces of the patch:

$$\bar{t}_1(X_1 = L) = -\frac{\lambda}{\lambda + 2\mu} b_2 X_2, \quad \bar{t}_2(X_1 = L) = 0, \quad (5.30)$$

$$\bar{t}_2(X_2 = L) = -\frac{\lambda}{\lambda + 2\mu} b_1 X_2, \quad \bar{t}_1(X_2 = L) = 0. \quad (5.31)$$

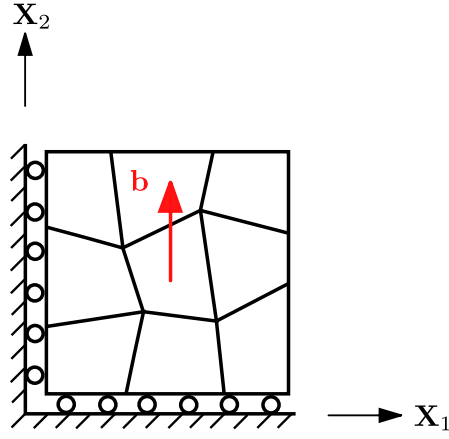


Figure 5.6: Depiction of the 2D quadratic patch test.

For a linear elastic material under plane strain conditions, an exact solution may be obtained of the form:

$$u_1(\mathbf{X}) = \frac{b_1}{2(\lambda + 2\mu)}(L - X_1)X_1 + \frac{\nu(b_1 - b_2)}{2\mu}LX_1, \quad (5.32)$$

$$u_2(\mathbf{X}) = \frac{b_2}{2(\lambda + 2\mu)}(L - X_2)X_2 + \frac{\nu(b_2 - b_1)}{2\mu}LX_2, \quad (5.33)$$

$$\sigma_{11}(\mathbf{X}) = b_1(L - X_1) + \frac{\lambda}{\lambda + 2\mu}b_2X_2, \quad (5.34)$$

$$\sigma_{22}(\mathbf{X}) = b_2(L - X_2) + \frac{\lambda}{\lambda + 2\mu}b_1X_1, \quad (5.35)$$

$$\sigma_{12}(\mathbf{X}) = 0. \quad (5.36)$$

A special (uniaxial) case will be considered, involving only a constant body force and no boundary tractions (provided $\nu = 0$ and $b_1 = 0$):

$$u_1(\mathbf{X}) = 0, \quad u_2(\mathbf{X}) = \frac{b_2}{2(\lambda + 2\mu)}(L - X_2)X_2, \quad (5.37)$$

$$\sigma_{11}(\mathbf{X}) = \sigma_{12}(\mathbf{X}) = 0, \quad \sigma_{22}(\mathbf{X}) = b_2(L - X_2). \quad (5.38)$$

The two quadrilateral meshes depicted in Figure 5.7 were used in conjunction with the FEM, using both 8-node serendipity and 9-node Lagrange isoparametric formulations. The DG-PEM was used on the polygonal mesh depicted in Figure 5.8.

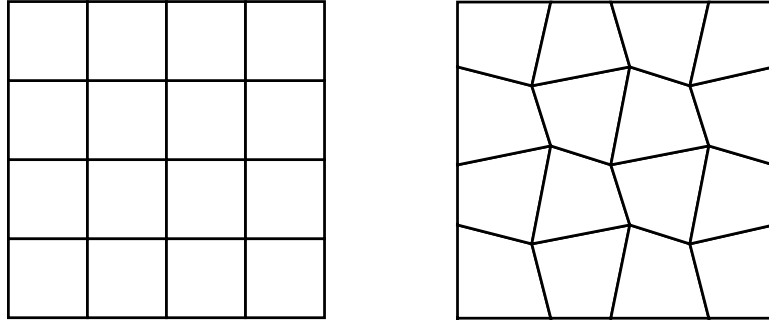


Figure 5.7: Quadrilateral meshes: (left) regular, (right) distorted.

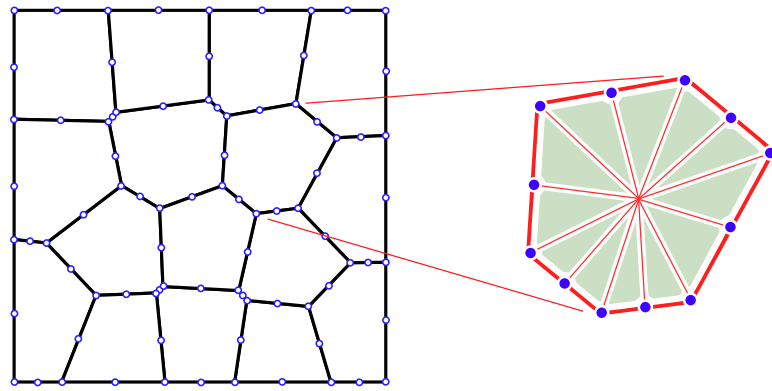


Figure 5.8: Patch of serendipity polygonal elements.

	$E_2(\Omega)$	$\ \mathbf{u}^h - \mathbf{u}\ / \ \mathbf{u}\ $	$\ \boldsymbol{\sigma}^h - \boldsymbol{\sigma}\ / \ \boldsymbol{\sigma}\ $
FEM (regular 8-node quadrilaterals)	9.0812E-016	1.7437E-009	1.3950E-008
FEM (distorted 8-node quadrilaterals)	4.7831E-003	9.9714E-005	2.0795E-003
FEM (regular 9-node quadrilaterals)	8.6713E-016	1.7437E-009	1.3950E-008
FEM (distorted 9-node quadrilaterals)	1.2818E-015	2.0841E-009	1.5752E-008
DG-PEM (no gradient correction)	3.3857E-008	9.8535E-002	2.8876E-001
DG-PEM (symmetric correction)	3.6486E-007	3.5935E-008	1.4642E-007
DG-PEM (nonsymmetric correction)	3.3857E-008	4.5498E-009	5.5341E-009

Table 5.7: Quadratic patch test results comparison for FEM and DG-PEM.

Quadratic patch test errors for the FEM and DG-PEM were explored. The DG-PEM bases were chosen such that $\varphi^h \in \mathcal{D}_2^h(\Omega)$, yielding quadratically complete shape functions. The results are presented in table 5.7.

It is interesting to note that the 8-node isoparametric quadrilaterals fail the quadratic

patch test if the mesh becomes distorted. Only affinely distorted 8-node quadrilaterals will exhibit quadratic completeness. Arbitrarily distorted elements will suffer from excessive interpolation errors, as observed in Table 5.7. This behavior is discussed in greater detail in [2] and [3]. In comparison, the 9-node quadrilateral elements preserve quadratic completeness, even when distorted as in Figure 5.7. However, it should be remarked that if the elements' edges are curved, both the 8- and 9-node isoparametric elements will lose 2nd order completeness, and fail quadratic patch tests.

To account for the effects of integration error, the DG-PEM requires the use of a gradient correction scheme. However, if a symmetric correction scheme is employed, there is an observed loss of completeness in the representation of the solution gradients over the element, corresponding to an increase in the interpolation error. Only the nonsymmetric gradient correction method is able to achieve the desired level of accuracy in the quadratic patch test.

Quadratic Patch Tests in 3D

The quadratic patch test described in the previous example may be extended directly to the 3-dimensional setting if the special (uniaxial) case is considered. As with the 3D linear patch test, the two hexahedral meshes depicted in Figure 5.4 were used in conjunction with the FEM, this time using 20-node isoparametric elements. The DG-PEM was used on the “serendipity” polyhedral mesh depicted in Figure 5.9, with similar parameter settings to those used for the 2D quadratic patch test. The results are displayed in Table 5.8.

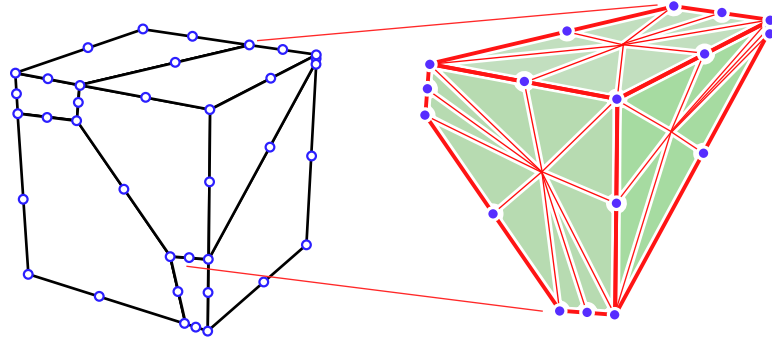


Figure 5.9: Patch of serendipity polyhedral elements.

As was the case in 2D, the 20-node isoparametric brick elements perform well on

	$E_2(\Omega)$	$\ \mathbf{u}^h - \mathbf{u}\ /\ \mathbf{u}\ $	$\ \boldsymbol{\sigma}^h - \boldsymbol{\sigma}\ /\ \boldsymbol{\sigma}\ $
FEM (regular hexahedra)	6.1677E-016	6.9751E-009	2.7900E-008
FEM (distorted hexahedra)	5.6085E-003	1.4755E-004	1.4958E-003
DG-PEM (no gradient correction)	3.2351E-008	1.3054E-001	2.9833E-001
DG-PEM (symmetric correction)	9.7520E-002	2.4536E-002	3.1112E-002
DG-PEM (nonsymmetric correction)	3.2351E-008	2.6577E-008	1.1622E-008

Table 5.8: 3D quadratic patch test results comparison for FEM and DG-PEM.

the regular (undistorted) mesh, but lose polynomial completeness on the distorted mesh. Correspondingly, there is an observed loss of accuracy in both $E_2(\Omega)$ and the patch test error metrics.

For the DG-PEM elements, an interesting phenomenon is observed with respect to the choice of gradient correction scheme. As was the case for the 2D quadratic patch test, applying a symmetric gradient correction (to both the trial and test functions) adversely impacts the polynomial completeness properties of the trial solution space. The effect is more pronounced for the 3D patch test. This result highlights the particular advantage of the nonsymmetric gradient correction scheme, which only modifies the test functions. Polynomial completeness of the trial solution space is therefore preserved, and patch test errors are rendered comparable with the (undistorted) FEM. The nonsymmetric gradient correction scheme shall therefore be used exclusively throughout the remainder of this chapter.

5.3 Tests for Element Quality

The primary advantage of partitioned element methods is that they allow for the elements to take on virtually arbitrary shape. However, elements with non-convex or degenerate features may degrade the overall accuracy of the resulting numerical solution. The motivation for the present study is to assess the effects of element formulation upon a given element's susceptibility to geometric locking phenomena.

Heuristically: an element will be more sensitive to the effects of locking if its local

stiffness matrix contains a number of eigenmodes (modes of deformation) whose corresponding eigenvalues are excessively large in comparison with the low-order (affine) deformation modes. In turn, meshes containing such elements will likewise possess several high-energy modes of deformation, contributing to the phenomenon of “mesh locking.”

As a separate issue from locking, if a given element’s local stiffness matrix is poorly conditioned, the global stiffness matrix of a mesh which contains said element may become poorly conditioned, as well. This may negatively impact the degree of solution accuracy that can be obtained due to floating point arithmetic. For implicit solid mechanics applications, the accuracy of any linear solver (whether direct or iterative) will be compromised by poor conditioning of the global stiffness matrix.

With these considerations borne in mind, several tests are conducted to examine the eigenvalue spectra of individual element stiffness matrices using varying element formulations and parameter settings. The eigenvalue spectra of several global stiffness matrices for polygonal meshes of variable quality are considered, as well.

Conditioning of Individual Element Stiffness Matrices

This section attempts to characterize the behavior of a representative sampling of polygonal PEM elements by examining the eigenvalues of each element’s elastic stiffness matrix.

For the elements considered, a comparison study is carried out to examine differences in the eigenvalue spectra of elements whose stiffness matrices were computed using various element formulations. Specifically, approximations to harmonic shape functions were obtained for each element using the CG-PEM, the DG-PEM, and a contemporary variant of the VETFEM arising from (3.25). These results are compared against a computed reference solution for the harmonic shape functions.

For each element, the elastic constants for Young’s modulus and Poisson’s ratio are chosen as $E = 1.0$ and $\nu = 0.0$, respectively. The choice of $\nu = 0.0$ is deliberate, and aims to decouple the effects of volumetric locking from the effects of geometric locking. For the purposes of comparison, all elements have roughly unit diameter.

Examination of the Effects of Geometric Non-convexity

A study was carried out to assess the effects of geometric non-convexity on a given element's eigenvalue spectrum. Three element shapes are considered, including: (A) a regular convex polygon, (B) an element with two collinear edges, and (C) a non-convex polygon. These elements are illustrated in Figure 5.10.

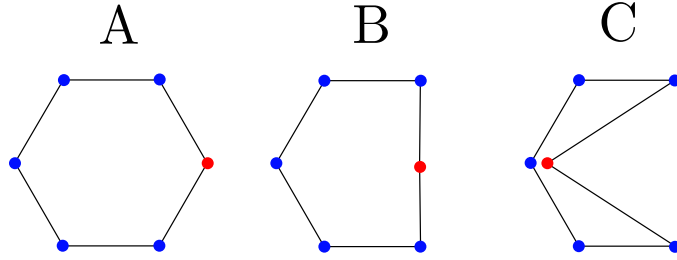


Figure 5.10: A representative sampling of hexagonal elements: (A) strictly convex, (B) two collinear edges, (C) non-convex.

The harmonic shape functions defined on these elements were approximated using the VETFEM, the CG-PEM, and the DG-PEM. The VETFEM approximations consisted of 4th order polynomials, and were obtained as the solutions to (3.25). The CG-PEM and DG-PEM approximations were obtained using the random Delaunay partitions shown in Figure 5.11. The penalty parameters appearing in (3.53) for the DG-PEM were chosen such that $\alpha_{\gamma 0} = 10$, $\alpha_{\gamma 1} = 0$ for all segments γ . Unless otherwise noted, the NIPG version of the DG-PEM (with $\epsilon = +1$) was utilized throughout. Reference solutions for the harmonic shape functions were computed on a highly refined partition of the element using the CG-PEM.

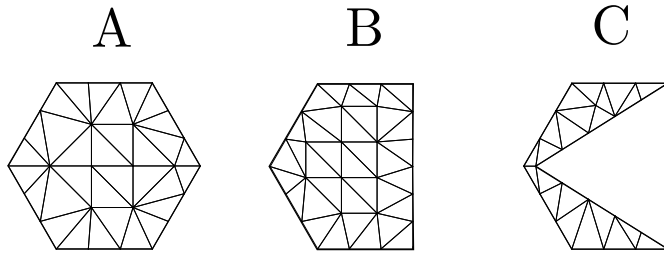


Figure 5.11: Delaunay partitions for elements A, B, and C.

For the red nodes indicated in Figure 5.10, color plots of the associated harmonic shape functions (and their corresponding approximations) are provided in Figure 5.12.

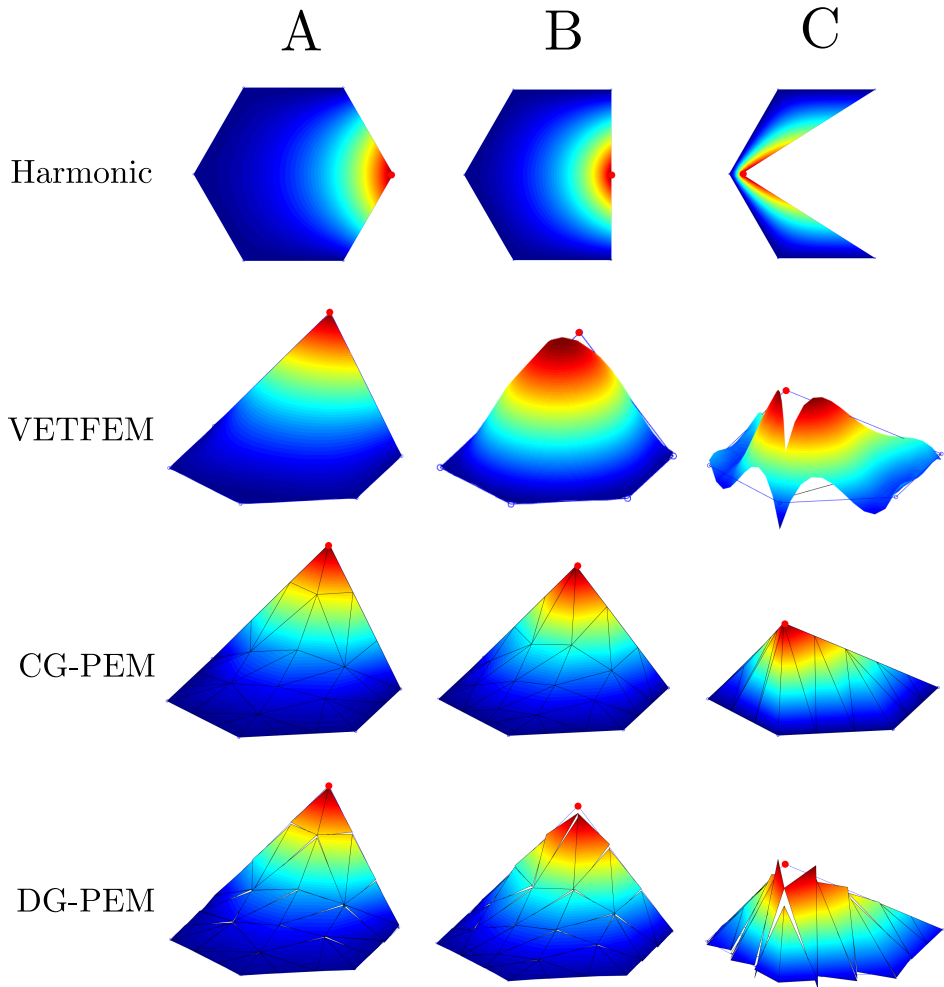


Figure 5.12: Comparison of the shape functions computed for elements A, B, and C using the VETFEM, CG-PEM, and DG-PEM.

Concerning the VETFEM approximations depicted in Figure 5.12 (particularly for elements B and C), the resulting shape functions present a number of undesirable features: oscillations, non-positivity, and non-interpolatory behavior. By comparison, the DG-PEM approximations avoid the issue of oscillations, though they are not strictly positive, nor are they interpolatory. Only the CG-PEM approximations can claim good behavior on all three fronts: they are non-oscillatory, strictly positive, and interpolatory. Nonetheless, it is important to emphasize that the aforementioned properties are not strictly necessary for convergence of the overall method. So long as a stable and consistent integration of the weak form is obtained, convergence is achieved. For certain applications, maintaining strict positivity or continuity of the shape function approximations may be desirable,

Element	A	B	C
Harmonic	0.9635	1.2151	7.1166
VETFEM	0.9950	4.4864	6.0305
CG-PEM	1.0723	1.2760	8.7108
DG-PEM	0.9668	1.1997	6.2766

(a) Largest eigenvalue: λ_{\max}

Element	A	B	C
Harmonic	0.5226	0.3449	0.00562
VETFEM	0.5335	0.3491	0.09189
CG-PEM	0.6175	0.3935	0.00694
DG-PEM	0.5345	0.3425	0.00527

(b) Smallest (non-zero) eigenvalue: λ_{\min}

Table 5.9: Comparison of maximum and minimum (non-zero) eigenvalues of the element stiffness matrices for the elements shown in Figure 5.10.

though such applications are not considered here.

Using the aforementioned approximations in place of the harmonic shape functions, the elements' elastic stiffness matrices were computed (by numerical quadrature). The eigendecomposition of each element's local stiffness matrix was then determined, with particular attention paid to the largest eigenvalue λ_{\max} and the smallest (non-zero) eigenvalue λ_{\min} . A comparison of the computed values for λ_{\max} and λ_{\min} is provided in table 5.9.

Irrespective of the chosen approximation method, the condition number for a given element's stiffness matrix becomes large as the degree of geometric non-convexity increases. The VETFEM yields a fairly accurate approximation for the eigenvalues of element A, but obtains an overly stiff approximation for element B, and overestimates the eigenvalues at the low end of the spectrum for element C. The CG-PEM appears to uniformly overestimate the eigenvalue spectra of all elements A, B, and C (though not significantly). By contrast, the DG-PEM under-estimates the eigenvalues for elements B and C, though this behavior is observed to be contingent upon how the penalty parameters $\alpha_{\gamma 0}$ and $\alpha_{\gamma 1}$ are specified. Table 5.10 illuminates the dependence of λ_{\max} and λ_{\min} (for element C) upon the choice of DG-PEM penalty parameters. Similar parameter dependencies are obtained for elements A and B.

The eigenvalue spectrum obtained for the DG-PEM converges to that of the CG-PEM as the value of $\alpha_{\gamma 0}$ is increased (provided $\alpha_{\gamma 1}$ is sufficiently small). Moreover, the shape functions will themselves converge to the C^0 continuous approximations obtained by the

DG-PEM	$\alpha_{\gamma 0} = 10^{-3}$	$\alpha_{\gamma 0} = 10^0$	$\alpha_{\gamma 0} = 10^3$	$\alpha_{\gamma 0} = 10^6$
$\alpha_{\gamma 1} = 0.0$	5.9210	5.4949	8.6484	8.7108
$\alpha_{\gamma 1} = 10^0$	5.9210	5.2235	7.7525	8.7106
$\alpha_{\gamma 1} = 10^3$	5.9210	5.0938	3.9671	7.7874
$\alpha_{\gamma 1} = 10^6$	5.9210	5.0935	3.8699	3.9640

(a) Largest eigenvalue: λ_{\max}

DG-PEM	$\alpha_{\gamma 0} = 10^{-3}$	$\alpha_{\gamma 0} = 10^0$	$\alpha_{\gamma 0} = 10^3$	$\alpha_{\gamma 0} = 10^6$
$\alpha_{\gamma 1} = 0.0$	0.004747	0.003554	0.006920	0.006943
$\alpha_{\gamma 1} = 10^0$	0.004748	0.003675	0.006489	0.006941
$\alpha_{\gamma 1} = 10^3$	0.004748	0.004210	0.002898	0.006508
$\alpha_{\gamma 1} = 10^6$	0.004748	0.004211	0.003660	0.002896

(b) Smallest (non-zero) eigenvalue: λ_{\min}

Table 5.10: Comparison of maximum and minimum (non-zero) eigenvalues of the element stiffness matrix for element C, computed for various DG-PEM penalty parameter values.

CG-PEM. Additionally, if $\alpha_{\gamma 0}$ is made sufficiently small, the eigenvalues will become relatively insensitive to the choice of $\alpha_{\gamma 1}$.

Conversely, as $\alpha_{\gamma 0}$ is increased, the eigenvalues (and the corresponding shape function approximations) become more sensitive to the choice of $\alpha_{\gamma 1}$. In such cases, $\alpha_{\gamma 1}$ may be thought of as a “regularization” parameter, acting to effectively smooth out variations in the gradient of the shape functions over the element. For low-order DG-PEM, increasing $\alpha_{\gamma 1}$ tends the element towards a uniform gradient formulation. Doing so risks rank-deficiency of the element’s resulting stiffness matrix. If $\alpha_{\gamma 0}$ and $\alpha_{\gamma 1}$ are increased proportionally to one another, one recovers the behavior of the pure penalty DG-PEM corresponding to (3.42).

Examination of the Effects of Nearly Degenerate Features

A study was carried out to assess the effects of geometric degeneracy on a given element’s eigenvalue spectrum. The two elements illustrated in Figure 5.13 are considered: a regular pentagon, and an irregular pentagon with a comparatively short edge.

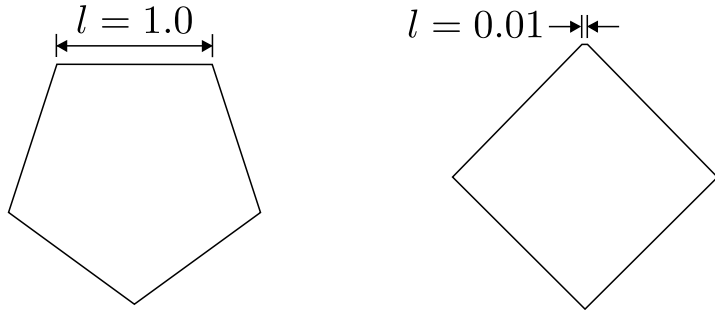


Figure 5.13: Two convex pentagonal elements: (left) regular pentagon with edges of equal length $l = 1.0$, (right) pentagon with a comparatively short edge of length $l = 0.01$.

	$l = 1.0$	$l = 0.01$
Harmonic	0.9510	5.0899
VETFEM	0.9510	1.6818
CG-PEM	1.1326	64.098
DG-PEM	0.9510	1.3085

(a) Largest eigenvalue: λ_{\max}

	$l = 1.0$	$l = 0.01$
Harmonic	0.4925	0.3951
VETFEM	0.4906	0.3746
CG-PEM	0.8387	0.5516
DG-PEM	0.4739	0.2592

(b) Smallest (non-zero) eigenvalue: λ_{\min}

Table 5.11: Comparison of maximum and minimum (non-zero) eigenvalues of the element stiffness matrices computed for the elements shown in Figure 5.13.

As in the previous example, the harmonic shape functions defined on these elements were approximated by the VETFEM (using 3rd order polynomials), the CG-PEM (using an edge-based partition), and the DG-PEM (using an edge-based partition, and the parameter settings described for the previous problem). Reference solutions for the harmonic shape functions were computed on a highly refined partition of the element using the CG-PEM.

As in the previous example, the aforementioned approximations were used in place of the harmonic shape functions when integrating the elements' elastic stiffness matrices. A comparison of the computed values for λ_{\max} and λ_{\min} is provided in table 5.11.

As noted in the previous example, the CG-PEM consistently over-estimates the eigenvalue spectra of the elements. Using a coarse (edge-based) partition further degrades the accuracy of the CG-PEM shape functions, to the extent that higher-order modes of deformation are severely over-stiff. Upon decreasing the edge length l further, the maximum

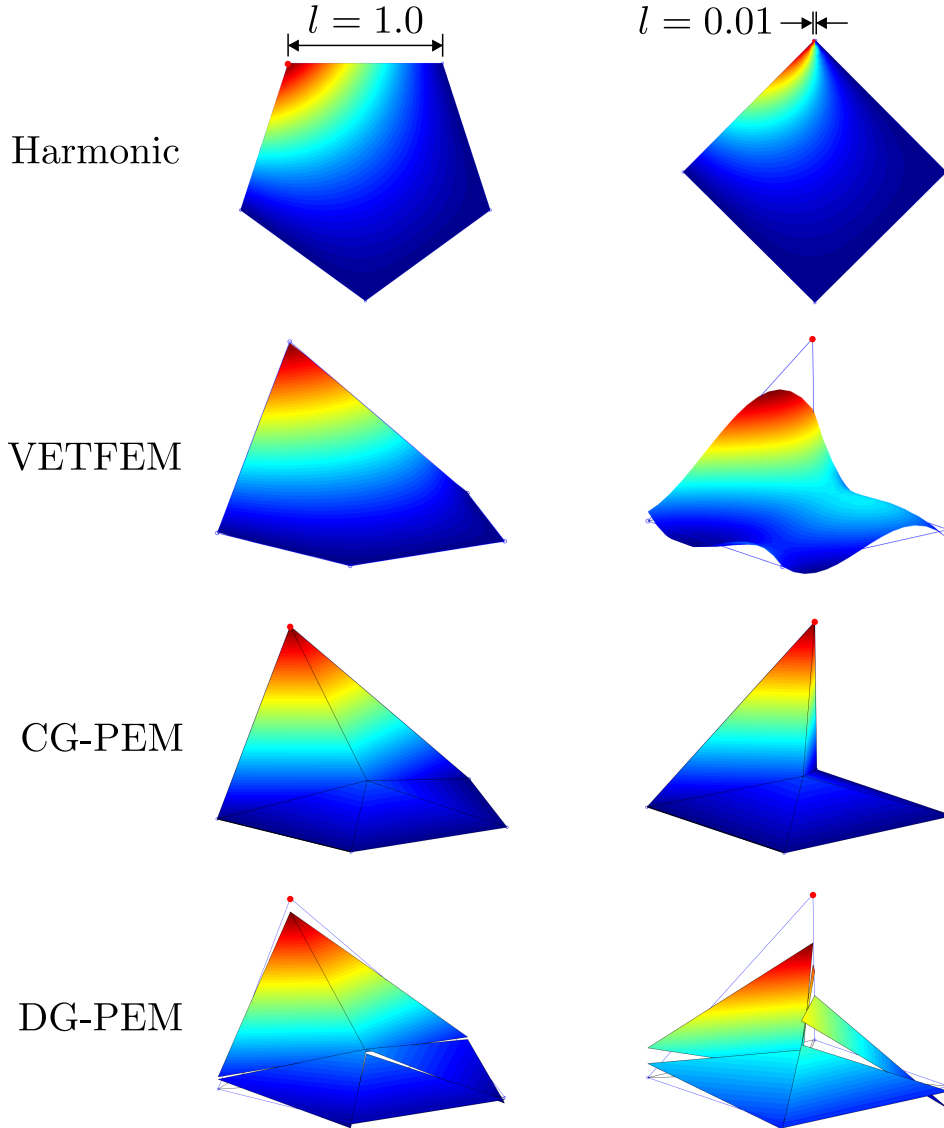


Figure 5.14: Comparison of shape functions computed for the two pentagonal elements with $l = 1.0$ and $l = 0.01$ using VETFEM, CG-PEM, and DG-PEM.

eigenvalue was observed to increase as $\lambda_{\max} \approx O(l^{-1})$. By comparison, the eigenvalue spectra for the VETFEM and DG-PEM remain small (well-conditioned), and relatively constant as $l \rightarrow 0$. The VETFEM, however, is observed to yield oscillatory solutions for the shape functions with decreasing l .

It remains to be seen whether the aforementioned insensitivity of the DG-PEM's eigenvalue spectra to short edges is a desirable quality. The following series of investigations seeks to evaluate the implications of this behavior for several polygonal meshes.

Meshes Consisting of Elements with Degenerate Edges

The present study seeks to quantify the effects of having an over-abundance of short edges within a polygonal finite element mesh. The two square patches depicted in Figure 5.15 are considered, each containing 1,000 polygonal elements. Both meshes were generated using PolyMesher, a polygonal meshing tool detailed in [78]. The Voronoi mesh in Figure 5.15a was obtained by a random point sampling process, and contains numerous elements with short edges. The mesh in Figure 5.15b was obtained after 100 iterations of Lloyd's algorithm, yielding a polygonal mesh with reasonably well-proportioned elements. Additionally, any remaining short edges in the mesh of Figure 5.15b were collapsed out according to the procedure described in [78].

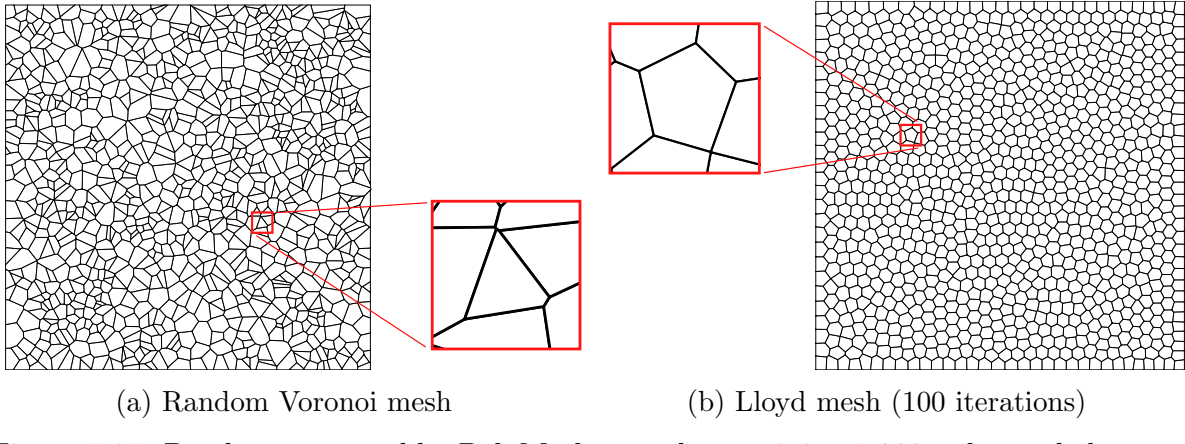


Figure 5.15: Patches generated by PolyMesher, each containing 1,000 polygonal elements.

First, some preliminary definitions are provided for a number of relevant mesh metrics. For every polygonal element $\Omega_e \subset \mathbb{R}^2$, let h_e denote the diameter of Ω_e , such that

$$h_e = \sup_{\mathbf{X}_1, \mathbf{X}_2 \in \Omega_e} \|\mathbf{X}_1 - \mathbf{X}_2\|_2. \quad (5.39)$$

Further, denote by $|E|$ the length of any edge $E \subset \partial\Omega_e$, and define ρ_e as the ratio of the smallest edge length $|E|$ divided by the element diameter h_e , i.e.

$$\rho_e = \max_{E \subset \partial\Omega_e} \frac{|E|}{h_e}. \quad (5.40)$$

For the meshes depicted in Figure 5.15, the aforementioned edge length metrics were computed for all elements and edges in each mesh. Several histograms which characterize this data are provided in Figure 5.16.

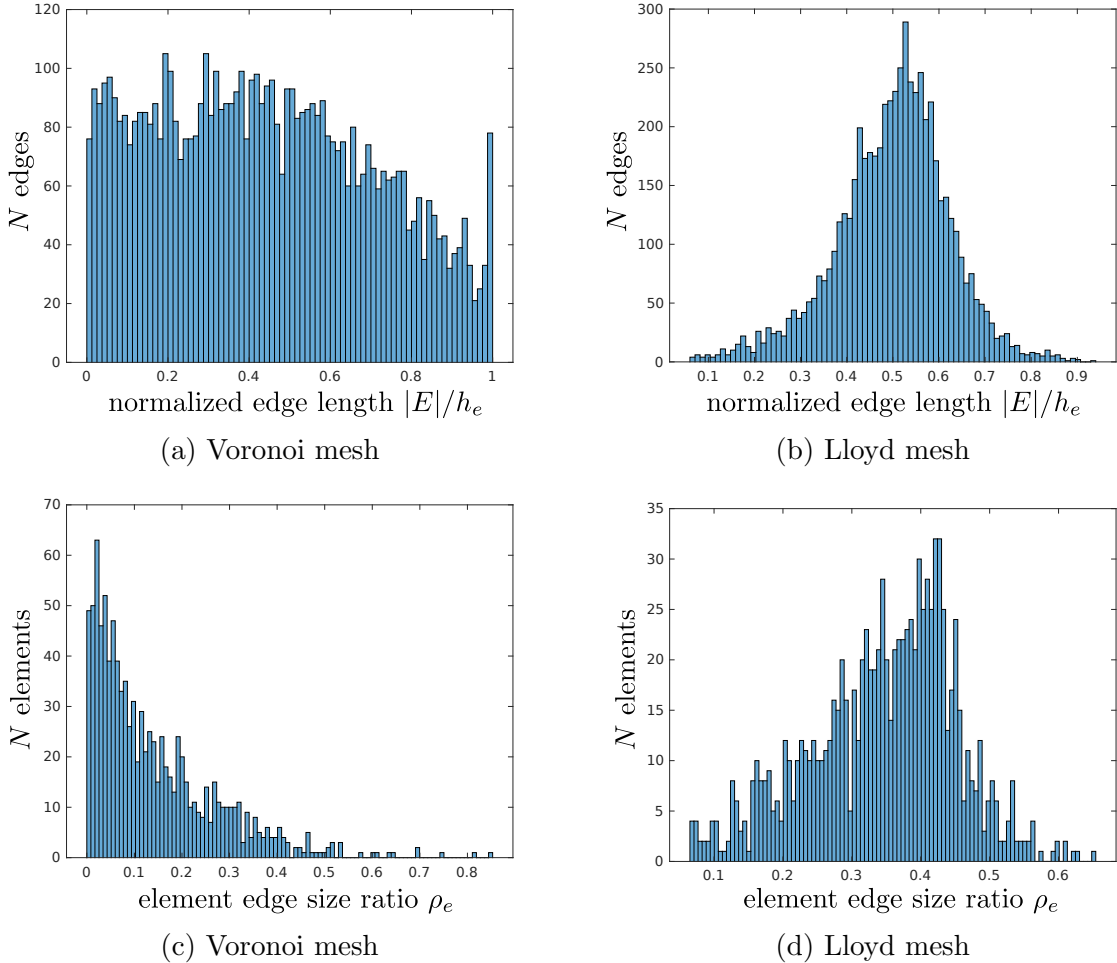


Figure 5.16: Histograms of various mesh metrics associated with the polygonal meshes depicted in Figure 5.15: (a) and (b) show the distributions of edge lengths contained in the random Voronoi and Lloyd meshes, respectively. (c) and (d) show the distributions for the smallest edge length ratios ρ_e in the random Voronoi and Lloyd meshes, respectively.

A key observation regarding Figure 5.16 concerns the distribution of edge lengths within the random Voronoi mesh. The normalized lengths of all edges in the Voronoi mesh appear to be distributed almost uniformly, as seen in Figure 5.16a. Nonetheless, Figure 5.16c suggests that there is a relatively high probability that any given element in the random Voronoi mesh will contain at least one short edge. By comparison, the distributions for $|E|/h_e$ and ρ_e in the Lloyd mesh are more Gaussian in nature, as demonstrated by Figures 5.16b and 5.16d, respectively.

To quantify the potential impact of short edges on finite element solution accuracy, the

eigenvalue spectra of each patch's global stiffness matrix \mathbf{K} were examined. Excessively large eigenvalues (particularly for the Voronoi mesh) may indicate solution sensitivity to the choice of discretization.

Each patch was specified to have unit dimensions (1×1) and material properties ($E = 1.0$, $\nu = 0.0$). Global stiffness matrices were assembled for the two polygonal meshes shown in Figure 5.15 using the CG-PEM and the DG-PEM. Both formulations employed an edge-based partitioning scheme with composite mid-point quadrature on each element. The DG-PEM parameters were specified as $\epsilon = +1$, $\alpha_{\gamma 0} = 10$, and $\alpha_{\gamma 1} = 0$. The resulting eigenvalue spectra are plotted in Figure 5.17.

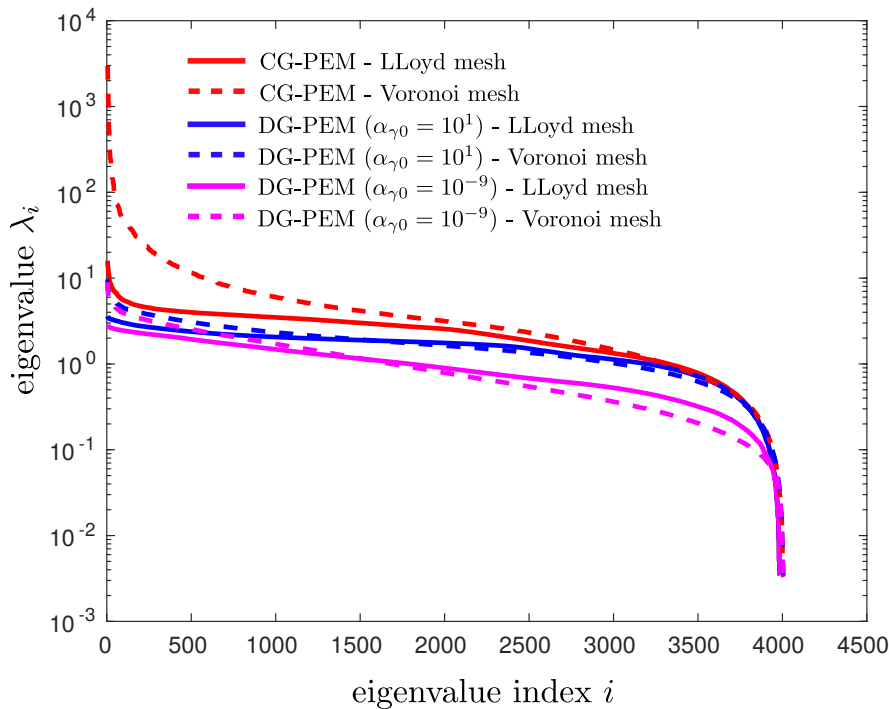


Figure 5.17: Eigenvalue spectra $\{\lambda_i\}_{i=1}^{N=3}$ for the (elastic) global stiffness matrix \mathbf{K} , computed for the CG-PEM and the DG-PEM ($\epsilon = +1$, $\alpha_{\gamma 1} = 0$).

For the Lloyd mesh, both the CG-PEM and DG-PEM produce fairly comparable eigenvalue spectra. For the random Voronoi mesh, the CG-PEM produces higher-energy modes with significantly larger eigenvalues than the DG-PEM. Interestingly, the DG-PEM yields very similar eigenvalue spectra for both meshes. This appears to indicate a diminished sensitivity of the DG-PEM solution to the chosen discretization. Importantly,

the behavior of the lower-energy modes remains the same across all meshes and element formulations. Figure 5.18 depicts the lowest-energy mode shapes determined by the DG-PEM. Similar mode shapes and corresponding eigenvalues were obtained for the CG-PEM.

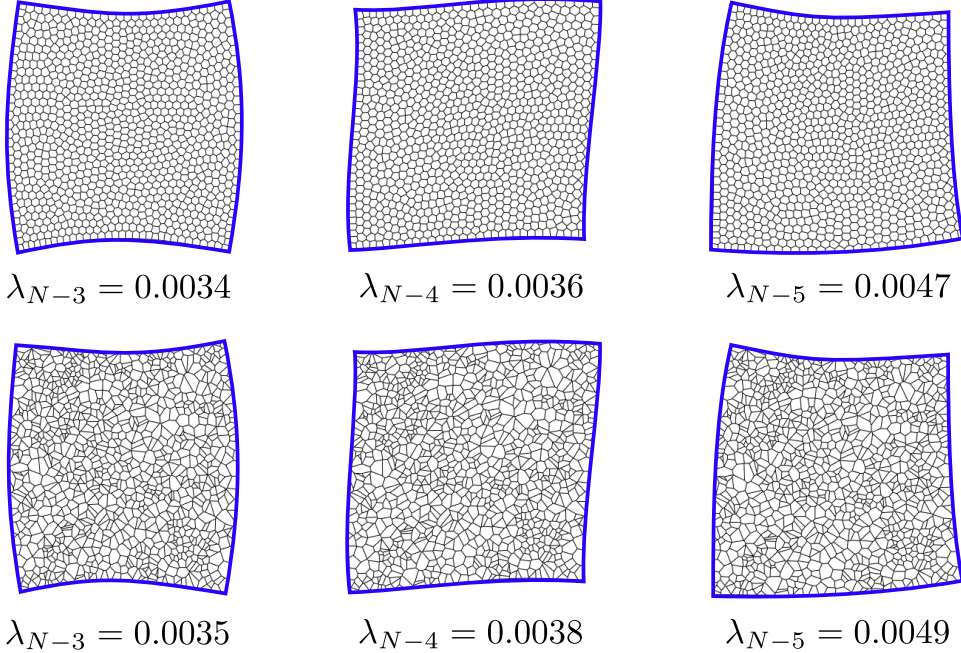


Figure 5.18: Depiction of the smallest non-zero eigenvalues and corresponding eigenmodes computed using the DG-PEM ($\epsilon = +1$, $\alpha_{\gamma 0} = 10$, $\alpha_{\gamma 1} = 0$). N denotes the size of the global stiffness matrix \mathbf{K} , and $\lambda_N = \lambda_{N-1} = \lambda_{N-2} = 0$ correspond to the zero-energy modes of deformation.

It is stressed that the results obtained for the DG-PEM will vary depending on the choice of penalty parameters $\alpha_{\gamma 0}$ and $\alpha_{\gamma 1}$. As $\alpha_{\gamma 0} \rightarrow \infty$ the behavior of the CG-PEM is recovered. The corresponding variability in the condition number of \mathbf{K} is characterized in Table 5.12.

The condition number of the resulting global stiffness matrix will become large (asymptotically approaching that of the CG-PEM) as $\alpha_{\gamma 0}$ is increased. Conversely, decreasing $\alpha_{\gamma 0}$ lowers the condition number of \mathbf{K} , achieving an apparent lower-bound on $\kappa(\mathbf{K})$ in the limit as $\alpha_{\gamma 0} \rightarrow 0$. Importantly, the resulting stiffness matrix does not contain spurious zero-energy modes, regardless of the choice of $\alpha_{\gamma 0}$. Because any choice of $\alpha_{\gamma 0} > 0$ yields stability, $\alpha_{\gamma 0}$ should not be regarded as a type of hourglass control parameter.

	Voronoi mesh	Lloyd mesh
CG-PEM	9.1e+05	4.6e+03
DG-PEM ($\alpha_{\gamma_0} = 10^3$)	4.8e+04	4.4e+03
DG-PEM ($\alpha_{\gamma_0} = 10^1$)	2.9e+03	1.0e+03
DG-PEM ($\alpha_{\gamma_0} = 10^{-1}$)	2.7e+03	8.1e+02
DG-PEM ($\alpha_{\gamma_0} = 10^{-9}$)	2.7e+03	8.1e+02

Table 5.12: Computed values for the condition number $\kappa(\mathbf{K})$ of the global stiffness matrix \mathbf{K} (excluding rigid body modes).

5.4 Convergence Studies

A handful of studies were conducted to assess the convergence behavior of the DG-PEM. These studies sought to verify that the DG-PEM yields convergent sequences of approximations under mesh refinement. A few relatively simple two- and three-dimensional elasticity problems are considered. The results obtained for the DG-PEM are compared against the results for the classical FEM. The DG-PEM employed the standard parameter settings utilized in previous problems. Convergence of both linear and quadratic PEM elements is established, and convergence in the incompressible limit is examined for discretizations consisting of hexahedra and arbitrary polyhedra.

Infinite Elastic Plate in Far-Field Tension

To demonstrate optimal convergence of the PEM for higher-order elements, consider the 2D elastostatics problem of an infinite plate with a circular hole in uniaxial tension (depicted in figure 5.19). The following analytical solutions for the displacement and stress fields were obtained from reference [84]:

$$u_1(r, \theta) = \frac{Ta}{8\mu} \left[\frac{r}{a}(\kappa + 1) \cos \theta + \frac{2a}{r}((1 + \kappa) \cos \theta + \cos 3\theta) - \frac{2a^3}{r^3} \cos 3\theta \right], \quad (5.41)$$

$$u_2(r, \theta) = \frac{Ta}{8\mu} \left[\frac{r}{a}(\kappa - 3) \sin \theta + \frac{2a}{r}((1 - \kappa) \sin \theta + \sin 3\theta) - \frac{2a^3}{r^3} \sin 3\theta \right], \quad (5.42)$$

$$\sigma_{11}(r, \theta) = T - T \frac{a^2}{r^2} \left(\frac{3}{2} \cos 2\theta + \cos 4\theta \right) + T \frac{3a^4}{2r^4} \cos 4\theta, \quad (5.43)$$

$$\sigma_{22}(r, \theta) = -T \frac{a^2}{r^2} \left(\frac{1}{2} \cos 2\theta - \cos 4\theta \right) - T \frac{3a^4}{2r^4} \cos 4\theta, \quad (5.44)$$

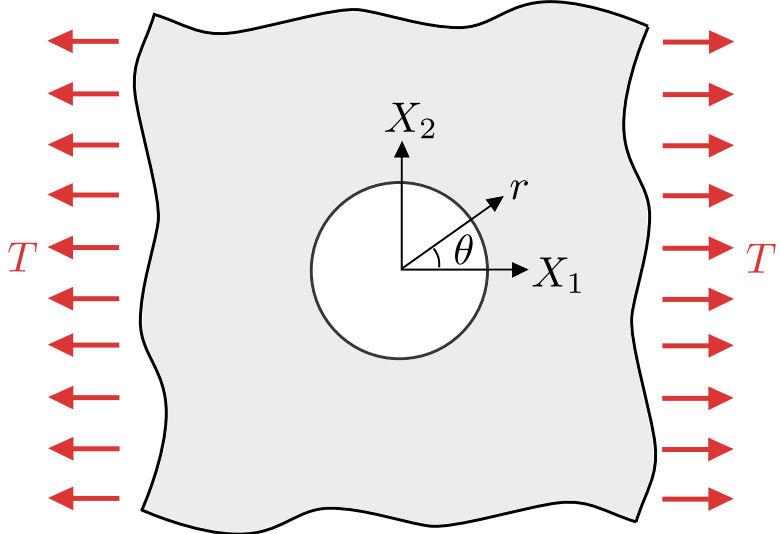


Figure 5.19: Infinite plate with a circular hole placed in uniaxial tension.

$$\sigma_{12}(r, \theta) = -T \frac{a^2}{r^2} \left(\frac{1}{2} \sin 2\theta + \sin 4\theta \right) + T \frac{3a^4}{2r^4} \sin 4\theta, \quad (5.45)$$

where T is the far-field value of the applied tensile stress, a is the radius of the circular hole centered at $r = 0$, $\kappa = 4 - 3\nu$ (under plane-strain conditions), and ν and μ are the Poisson's ratio and shear modulus of the material, respectively.

A convergence study was carried out using a series of quadrilateral meshes with varying levels of refinement, discretizing the restricted problem domain $X_i \in [-1, +1]$, $i = 1, 2$ with $a = 0.25$ (see figure 5.20.) The meshes consisted of either 4-node quadrilateral or 8-node serendipity quadrilateral elements. In each case, the elements employed either an isoparametric formulation, or a sufficiently high-order DG-PEM formulation (i.e. $k = 1$ for 4-node quadrilaterals, and $k = 2$ for 8-node quadrilaterals.) Displacement boundary conditions were prescribed to be consistent with the exact solution on the restricted domain boundary.

Displacement and stress error norms were computed with reference to the exact solution for the following problem parameters: $E = 29000.0$, $\nu = 0.3$, and $T = 1.0$. Convergence plots for the displacement and stress error norms are provided in Figures 5.21a and 5.21b, respectively.

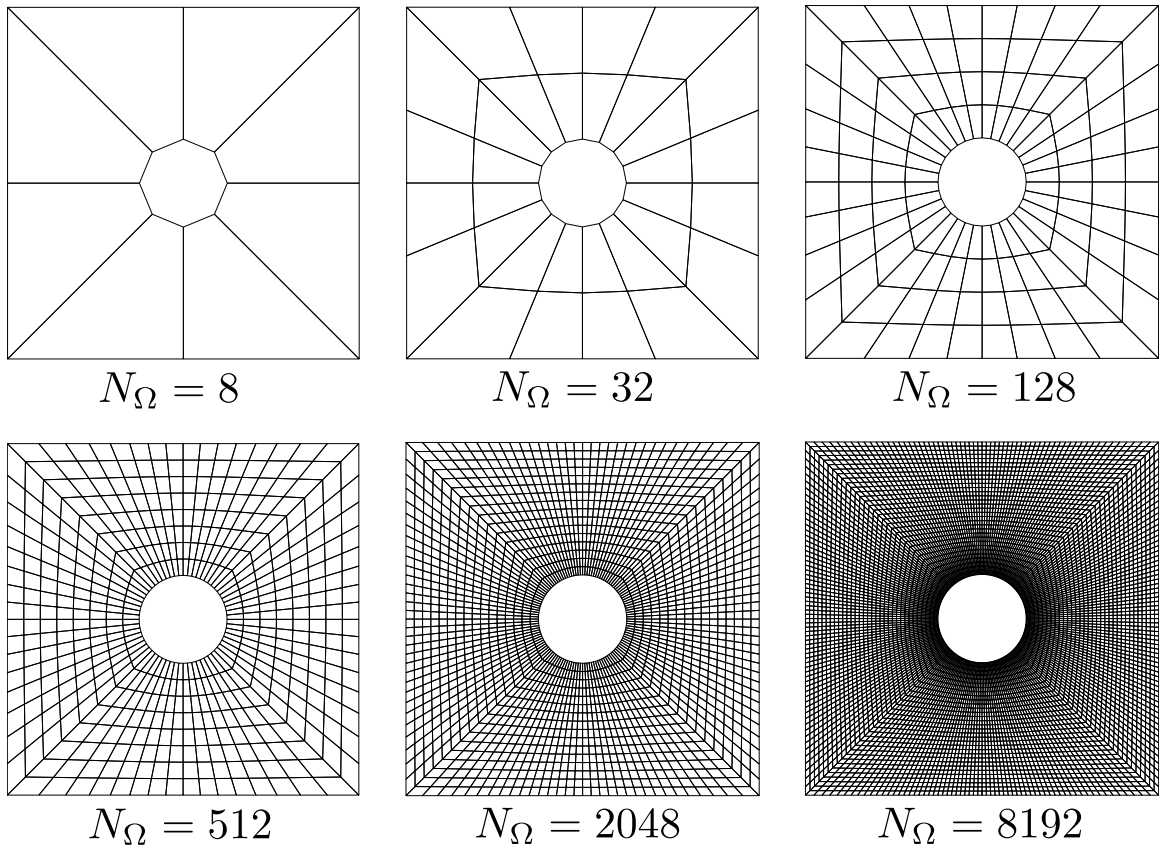


Figure 5.20: Quadrilateral meshes with varying levels of refinement.

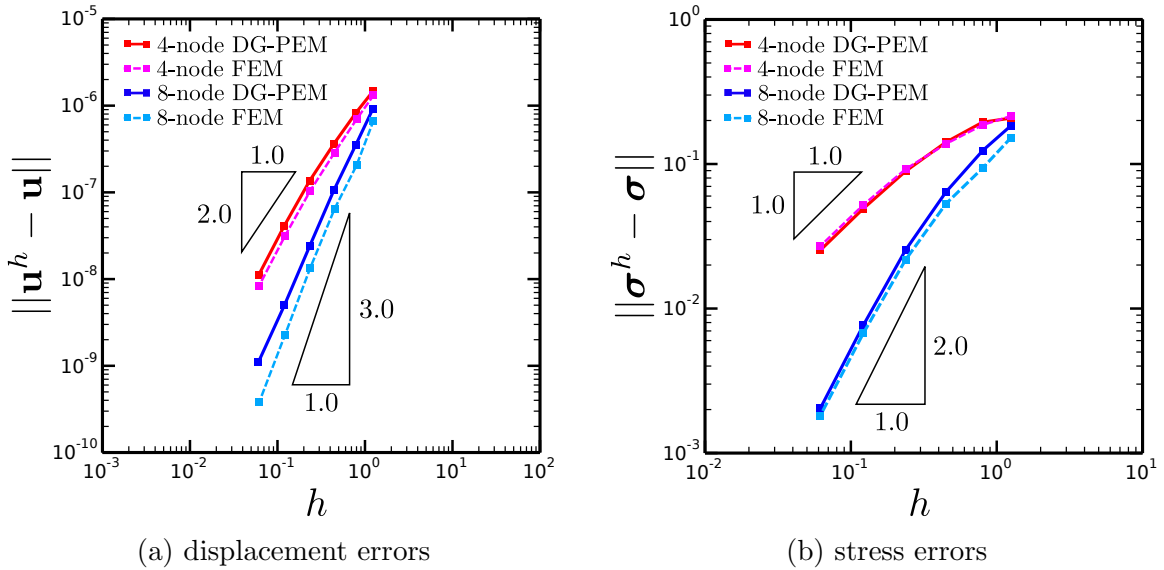


Figure 5.21: Convergence plots for the plate with hole problem using FEM and DG-PEM.

For a given element formulation, the *rate* of convergence in the two error metrics

$$\|\mathbf{u}^h - \mathbf{u}\| \leq Ch^p\|\mathbf{u}\|, \quad \|\boldsymbol{\sigma}^h - \boldsymbol{\sigma}\| \leq Ch^q\|\boldsymbol{\sigma}\|, \quad (5.46)$$

is characterized by the powers p and q , respectively. The average and maximal rates of convergence for each element formulation across all levels of mesh refinement are displayed in Table 5.13.

	p_{avg}	p_{max}	q_{avg}	q_{max}
FEM (4-node quadrilateral)	1.66 (2.0)	1.94 (2.0)	0.66 (1.0)	0.96 (1.0)
DG-PEM (4-node quadrilateral)	1.88 (2.0)	2.13 (2.0)	0.73 (1.0)	0.99 (1.0)
FEM (8-node quadrilateral)	2.48 (3.0)	2.68 (3.0)	1.43 (2.0)	1.93 (2.0)
DG-PEM (8-node quadrilateral)	2.34 (3.0)	3.02 (3.0)	1.71 (2.0)	2.42 (2.0)

Table 5.13: Average and maximal convergence rates for each method. The optimal rates are shown in parentheses.

It should be noted that part of the solution error incurred for the coarse meshes may be attributable to the inexact representation of the problem geometry (the circular hole). This would explain why the observed convergence rates are lower at coarser levels of refinement, but approach the optimal rates as the mesh is further refined.

In the limit as $h \rightarrow 0$, the linear and quadratic DG-PEM converge at the optimal rates in both the displacement and stress error norms. Because the quadrilateral meshes in Figure 5.20 consist of non-affinely distorted elements, the FEM using 8-node serendipity elements does not achieve the optimal rates of convergence. Overall, the DG-PEM appears to converge at slightly faster rates than the FEM. However, the solution errors at coarser levels of refinement tend to be smaller for the FEM, in general.

Future work will seek to investigate the measured error and convergence rates of the PEM when the elements take on arbitrary shape, and for a variety of different formulations and penalization parameter settings.

Incompressible Twisting Annulus

Consider the elastic annulus depicted in Figure 5.22, whose inner radius at $r = R_i$ is fixed, and whose outer radius $r = R_o$ rigidly rotates at an angular velocity of Φ . The radially

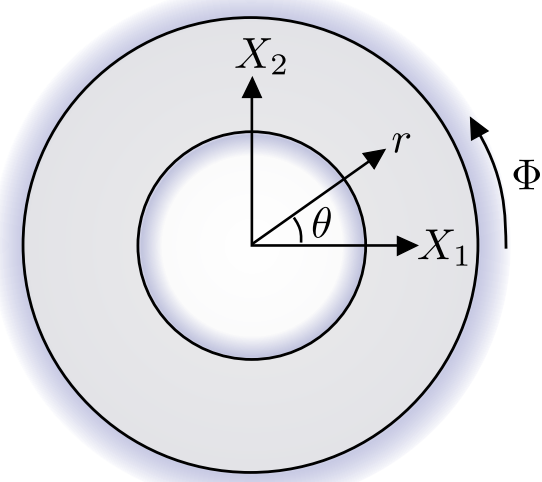


Figure 5.22: Depiction of the twisting annulus problem.

symmetric displacement boundary conditions for this motion are described by

$$u_r(R_i, t) = u_r(R_o, t) = 0, \quad u_z(R_i, t) = u_z(R_o, t) = 0, \quad (5.47)$$

$$u_\theta(R_i, t) = 0, \quad u_\theta(R_o, t) = R_o \Phi t, \quad (5.48)$$

for all $t \geq 0$.

Let the elastic material be characterized by the isotropic hypoelastic model of grade zero, consistent with the Jaumann rate of stress:

$$\dot{\boldsymbol{\sigma}} = \mathbb{C} : \mathbf{D} + \mathbf{W}\boldsymbol{\sigma} - \boldsymbol{\sigma}\mathbf{W}. \quad (5.49)$$

If the material is incompressible (if $\text{tr}(\mathbf{D}) = 0$), an analytical solution may be determined which is valid for finite deformations. The solutions for the displacement and stress fields are derived in the Appendix. The resulting expressions are given below:

$$u_r = u_z = 0, \quad u_\theta = \frac{R_o^2}{r} \frac{r^2 - R_i^2}{R_o^2 - R_i^2} \Phi t, \quad (5.50)$$

$$\sigma_{rr} = -\sigma_{\theta\theta} = \mu \frac{R_i^2}{r^2} \left[\cos \left(2 \frac{R_o^2}{R_o^2 - R_i^2} \Phi t \right) - 1 \right], \quad \sigma_{r\theta} = \mu \frac{R_i^2}{r^2} \sin \left(2 \frac{R_o^2}{R_o^2 - R_i^2} \Phi t \right). \quad (5.51)$$

Because the element formulations used herein possess only displacement degrees of freedom, it is not possible to run an analysis for a truly incompressible material. It suffices to examine numerical solutions in the near-incompressible regime (i.e. $\nu = 0.4999$). To

combat the issue of volumetric locking, the kinematic enhancement suggested in [63] was implemented, and utilized in conjunction with each of the element formulations considered herein. Element formulations which have been “enhanced” in this manner are henceforth indicated as such.

Additionally, because an accurate prediction of the pressure field would otherwise require the use of a mixed formulation, the stress error metric in (5.23) will be dominated by errors in the pressure field. For this reason, only the errors in the deviatoric stress field will be examined:

$$\frac{||\mathbf{s}^h - \mathbf{s}||}{||\mathbf{s}||} = \sqrt{\frac{\int_{B_0} (\mathbf{s}^h - \mathbf{s}) : (\mathbf{s}^h - \mathbf{s}) dV}{\int_{B_0} \mathbf{s} : \mathbf{s} dV}}, \quad (5.52)$$

where $s_{ij} = \sigma_{ij} - \frac{1}{3}\sigma_{kk}\delta_{ij}$ denotes the stress deviator.

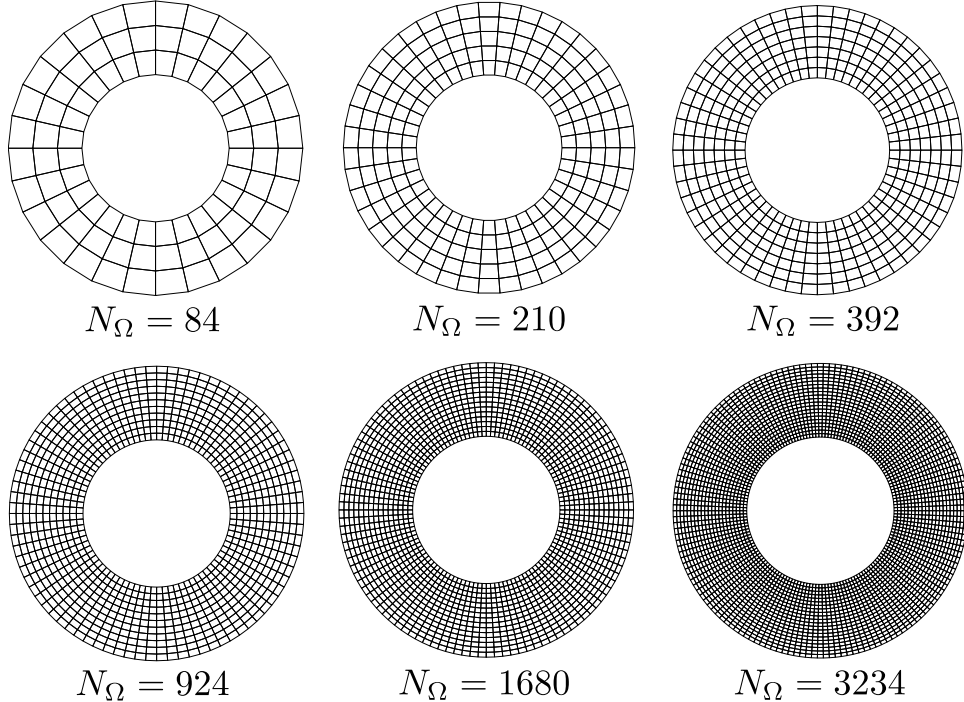


Figure 5.23: Hexahedral meshes with varying levels of refinement for the twisting annulus problem.

Convergence studies were carried out using the hexahedral and polyhedral meshes depicted in Figures 5.23, 5.24, and 5.25. The hexahedral meshes were used in conjunction with the FEM, whereas the polyhedral meshes were used in conjunction with the

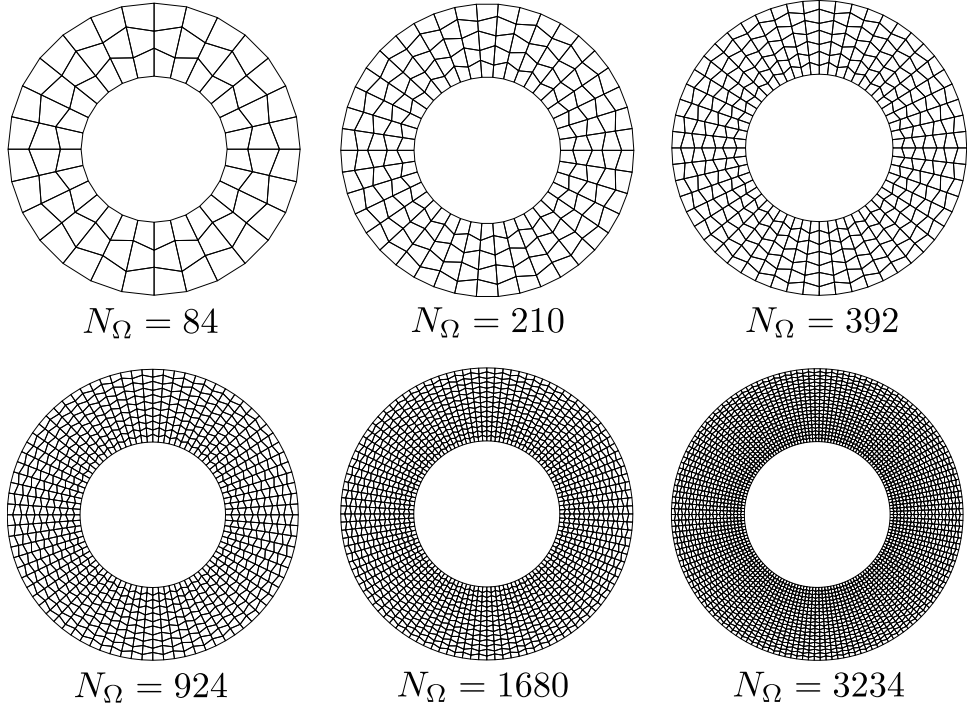


Figure 5.24: Distorted hexahedral meshes with varying levels of refinement for the twisting annulus problem.

DG-PEM. Each mesh consisted of a single layer of elements in the z -direction. All z -displacements were constrained, consistent with the assumptions of plane strain.

Finite deformations were considered in the analysis, albeit at relatively small strains (roughly 0.26%). Error norms were computed with reference to the exact solution using the following problem parameters: $R_i = 0.5$, $R_o = 1.0$, $\Phi = 0.001$, $E = 1.0$, $\nu = 0.4999$, $t \in [0.0, 1.0]$.

For a given element formulation, the rate of convergence in the two error metrics

$$\|\mathbf{u}^h - \mathbf{u}\| \leq Ch^p\|\mathbf{u}\|, \quad \|\mathbf{s}^h - \mathbf{s}\| \leq Ch^q\|\mathbf{s}\|, \quad (5.53)$$

is characterized by the powers p and q , respectively. The average and maximal rates of convergence for each element type across all levels of mesh refinement are displayed in Table 5.14. A convergence plot is provided in Figure 5.26 for the purposes of comparison.

Interestingly, the undistorted hexahedral meshes of Figure 5.23 do not present symptoms of volumetric locking. On these meshes, both the standard and enhanced element formulations converge at roughly the same rates in the displacement and stress error

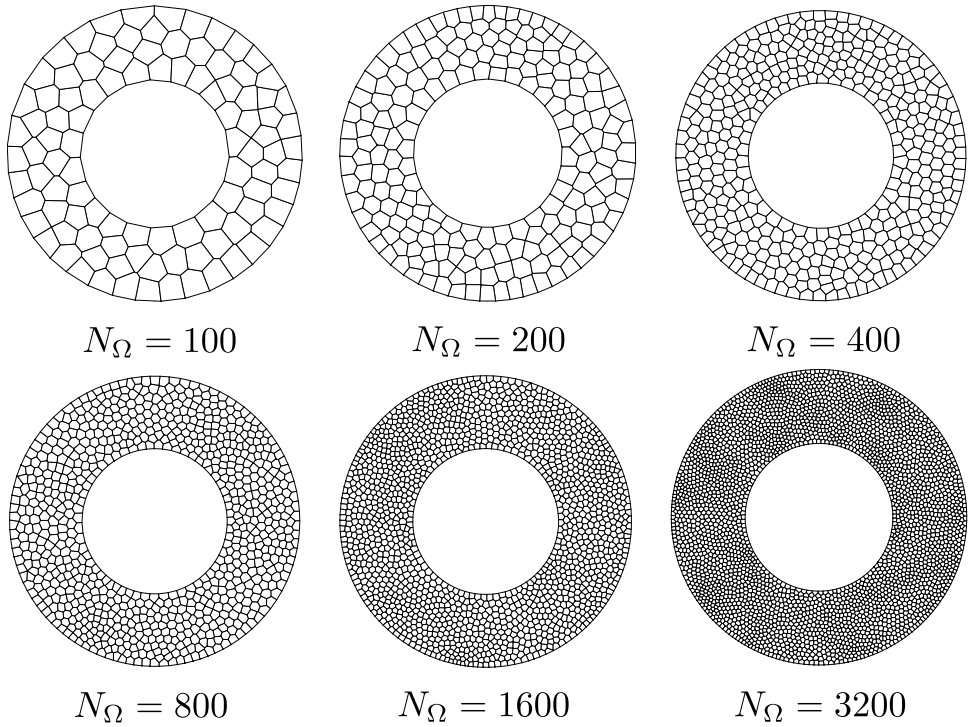


Figure 5.25: Polyhedral meshes with varying levels of refinement for the twisting annulus problem.

	p_{avg}	p_{max}	q_{avg}	q_{max}
Hexahedra (FEM)	1.61 (2.0)	2.72 (2.0)	1.01 (1.0)	1.01 (1.0)
Hexahedra (enhanced)	1.91 (2.0)	2.66 (2.0)	1.01 (1.0)	1.01 (1.0)
Distorted Hexahedra (FEM)	-0.66 (2.0)	0.57 (2.0)	-0.03 (1.0)	0.35 (1.0)
Distorted Hexahedra (enhanced)	0.51 (2.0)	0.66 (2.0)	0.28 (1.0)	0.39 (1.0)
Polyhedra (DG-PEM)	0.23 (2.0)	0.92 (2.0)	0.67 (1.0)	1.04 (1.0)
Polyhedra (enhanced)	2.05 (2.0)	2.74 (2.0)	1.11 (1.0)	1.20 (1.0)

Table 5.14: Average and maximal convergence rates for each element type/formulation. The optimal rates are shown in parentheses.

norms.

In contrast, the distorted hexahedral meshes of Figure 5.24 succumb to spurious oscillations in the pressure field, regardless of whether the kinematic enhancement of [63] is employed. Figures 5.27b and 5.27e illustrate the characteristic “checkerboard” pattern in the pressure field that arises for the distorted meshes. The corresponding rates of

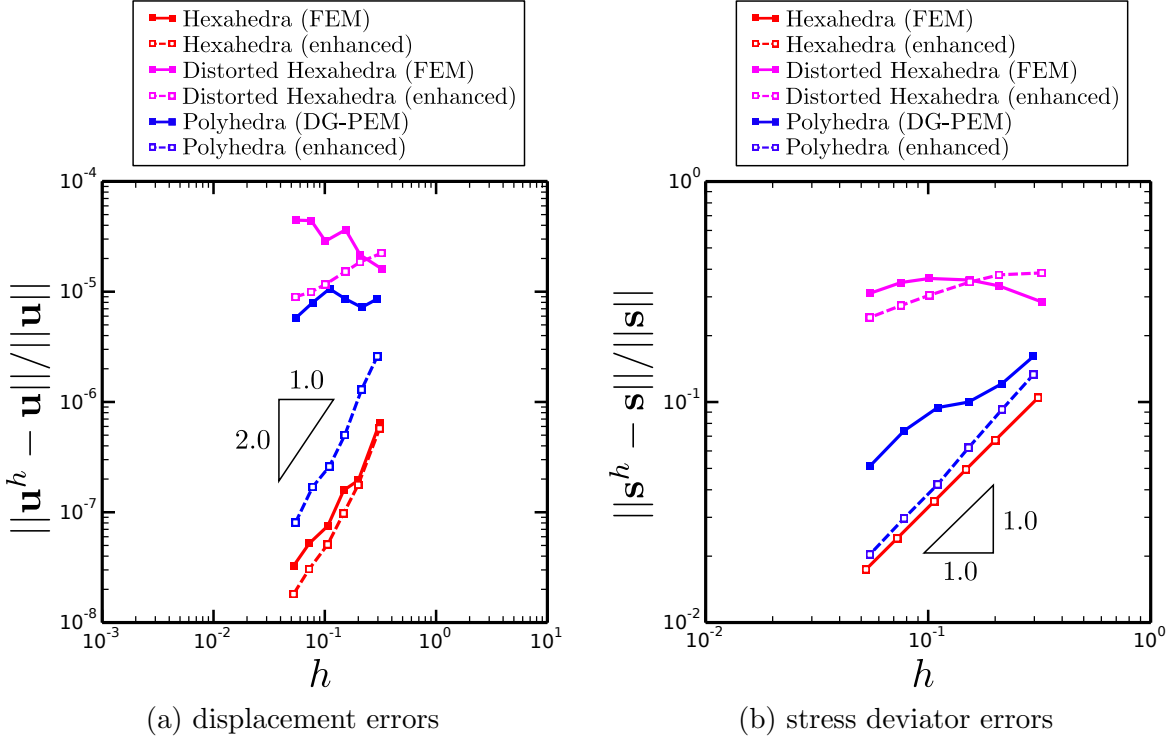


Figure 5.26: Convergence plots for the twisting annulus problem using FEM for hexahedra and DG-PEM for polyhedra.

convergence are only slightly improved for the enhanced formulation.

The arbitrary polyhedral meshes of Figure 5.25 are less sensitive to the effects of volumetric locking. Optimal rates of convergence are fully restored when the kinematic enhancement is utilized.

If the DG-PEM is utilized on either of the two series of hexahedral meshes shown in Figures 5.23 and 5.24, the resulting convergence rates match those of the FEM. This illustrates an important point: the particular choice of *discretization* (the shape of the elements) controls mesh sensitivity to volumetric locking, more so than the underlying element formulation. Consider the extreme case of a mesh consisting entirely of linear tetrahedra. Such a mesh will produce identical results for the FEM, and all variants of the PEM. In the aforementioned scenario, volumetric locking will persist, regardless of which element formulation is utilized. The same rationale is true for the distorted hexahedral meshes. As such, the PEM should not be viewed as a direct remedy to volumetric locking. Rather, the PEM simply enables the use of more general discretizations, which may

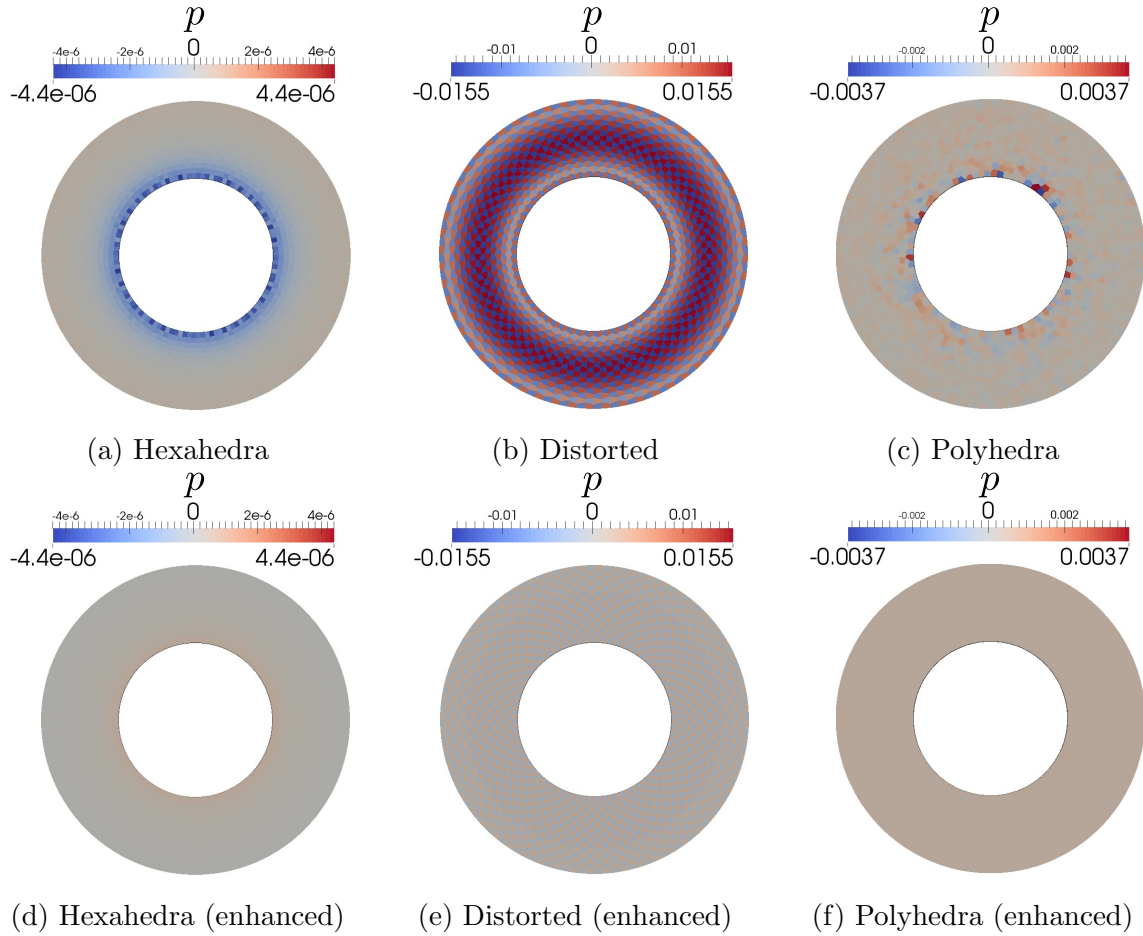


Figure 5.27: Comparison of pressure fields for various element types and formulations. Color scales are kept consistent between similar mesh types.

themselves be less susceptible to locking.

These observations lead to a related line of inquiry: can a given discretization be designed in such a fashion as to obviate locking altogether? Do random Voronoi meshes produce “better” results (in some statistical sense) over hexahedral meshes, and can such improvements be adequately quantified? With the geometric flexibility of the PEM in hand, the answers to these questions are within reach. The continued pursuit of such questions remains the subject of ongoing work.

5.5 Large Deformation Problems with Elasto-plastic Material Behavior

A set of examples were explored to examine the behavior of the DG-PEM in the context of both geometric and material nonlinearity. The primary motivation for the present study is to evaluate the DG-PEM's ability to handle problems involving high plastic flow. Such problems pose two primary, yet opposing challenges: excessive plastic deformation may lead to mesh tangling and element inversion, and certain element types may succumb to volumetric locking, thereby preventing plastic deformation from occurring. To combat the latter problem, the kinematic enhancement suggested in [63] is utilized in conjunction with the element formulations considered herein. Unless noted otherwise, the DG-PEM employed the standard parameter settings utilized in previous problems.

A simple J_2 model for hypo-elasto-plasticity with linear isotropic hardening was implemented, employing the canonical radial return algorithm discussed in [1]. This model is utilized in the two problems considered in this section, entailing the specification of the following material parameters: Young's modulus E , Poisson's ratio ν , an initial yield stress Y_0 , and a linear hardening modulus E_h .

Necking of a Ductile Steel Tensile Specimen

A tensile test for a 4130 steel plate specimen with square cross-section was simulated under isothermal conditions. The test setup was based in part upon the experimental procedures discussed in [37]. The dimensions of the plate specimen illustrated in Figure 5.28 conform with the ASTM 2008 standard [26]. The J_2 elasto-plasticity model was utilized with the following model parameters chosen based upon the data provided by [44]: $E = 29,700$ ksi, $\nu = 0.29$, $Y_0 = 63.1$ ksi, and $E_h = 0.0$ ksi. Perfect plasticity was assumed to induce the immediate onset of necking within the specimen, as suggested in [48].

The tests were simulated under quasi-static loading conditions. The (reflected) eighth-symmetric meshes shown in Figures 5.29a and 5.29b were used in conjunction with the FEM and DG-PEM, respectively. Both meshes consisted of roughly 400 elements. To

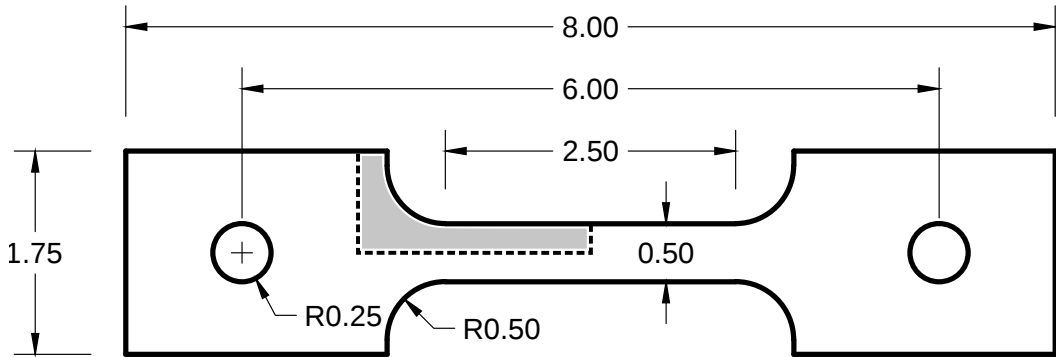


Figure 5.28: Tensile specimen dimensions, in inches. The thickness of the plate specimen shown is 0.5 in., resulting in a square cross-section along the gage length. The area shown in grey represents the eighth-symmetric modeling domain.

assist with the initiation of necking, each mesh also contained a small geometric defect mid-way along the gage length: a 1% reduction in the cross-sectional area of the specimen.

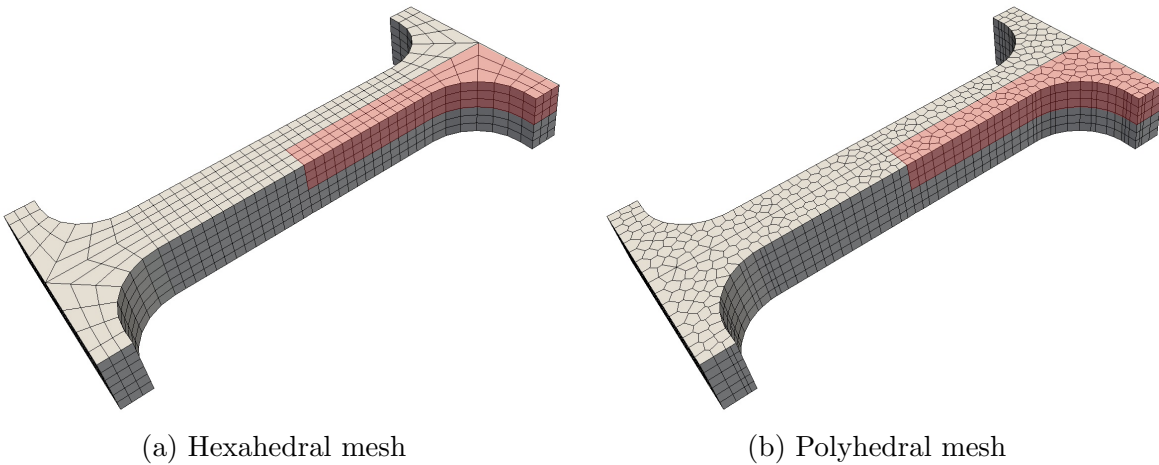


Figure 5.29: Plate specimen meshes used for the tensile necking problem, modeled as an eighth-symmetric problem.

Values of true (Cauchy) stress and engineering strain were measured from the analysis results via the post-processing tools available in ParaView [4]. The vertical component of Cauchy stress was averaged over the necked area of the specimen to determine an average tensile stress. To maintain consistency with the experimental procedures in [37], the engineering strain and percent elongation of the specimen were measured over a gage length of 2 inches. The % reduction in area of the specimen was also recorded at the location of necking.

The visualized results of the simulations are depicted in Figure 5.30. When the kinematic enhancement is utilized, the results obtained using the FEM and the DG-PEM are comparable to one another. Both formulations succumb to volumetric locking if the enhancement is omitted. However, the polyhedral discretization used with the DG-PEM is less sensitive to the effects of locking, consistent with previous observations.

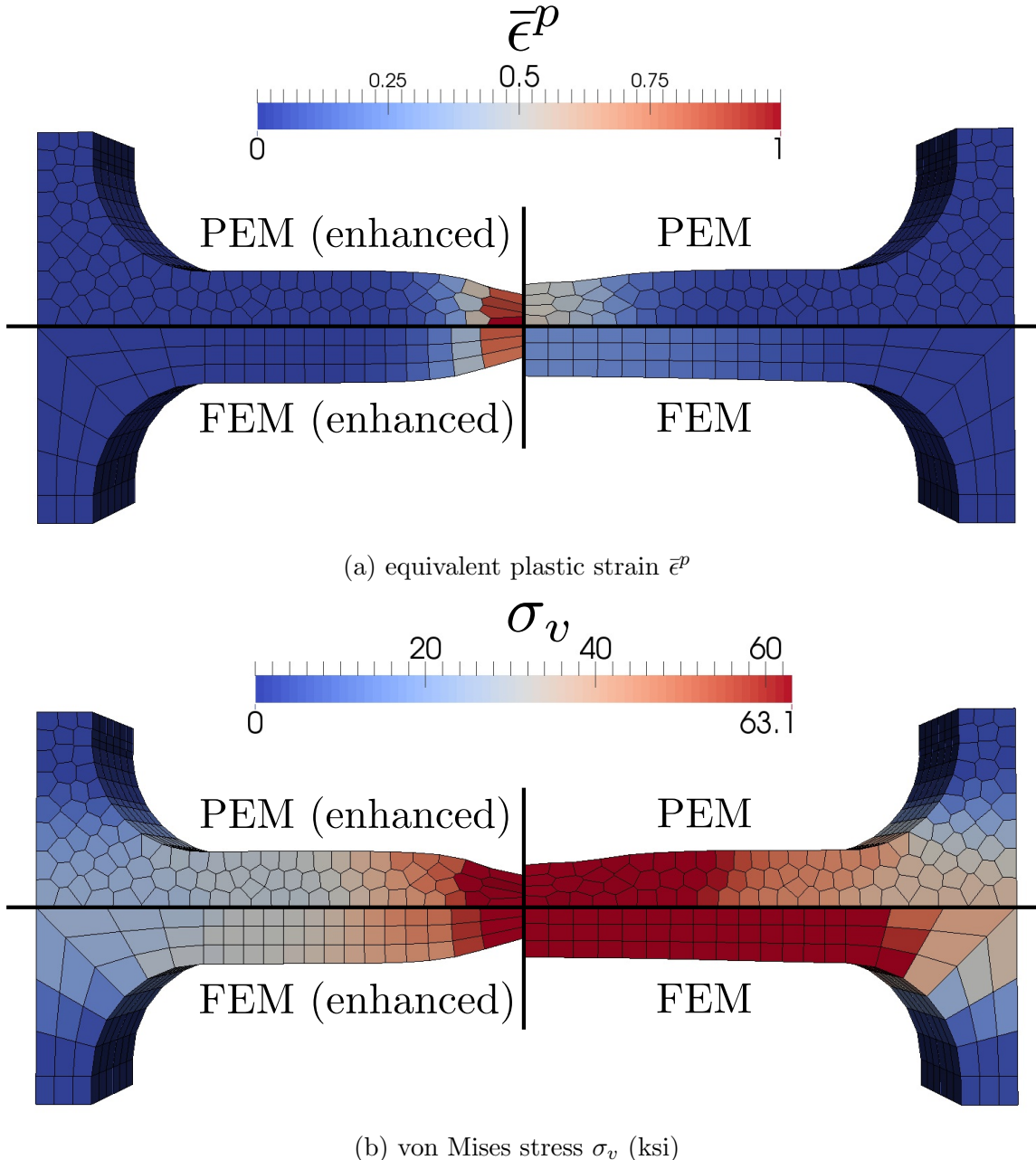


Figure 5.30: Comparison of necking behavior at 16.5% elongation, depicting deformed shapes and color map values of equivalent plastic strain $\bar{\epsilon}^p$ and von Mises stress σ_v (ksi).

Plots of the computed (Cauchy) stress vs. engineering strain curves from each simulation are depicted in Figure 5.31a. Additionally, Figure 5.31b compares the decrease in the necked area of the specimen vs. engineering strain. In each plot, the results for the FEM and the DG-PEM provide comparable accuracy if the kinematic enhancement is employed. If the enhancement is not utilized, the FEM performs more poorly than the DG-PEM, exhibiting little to no necking behavior.

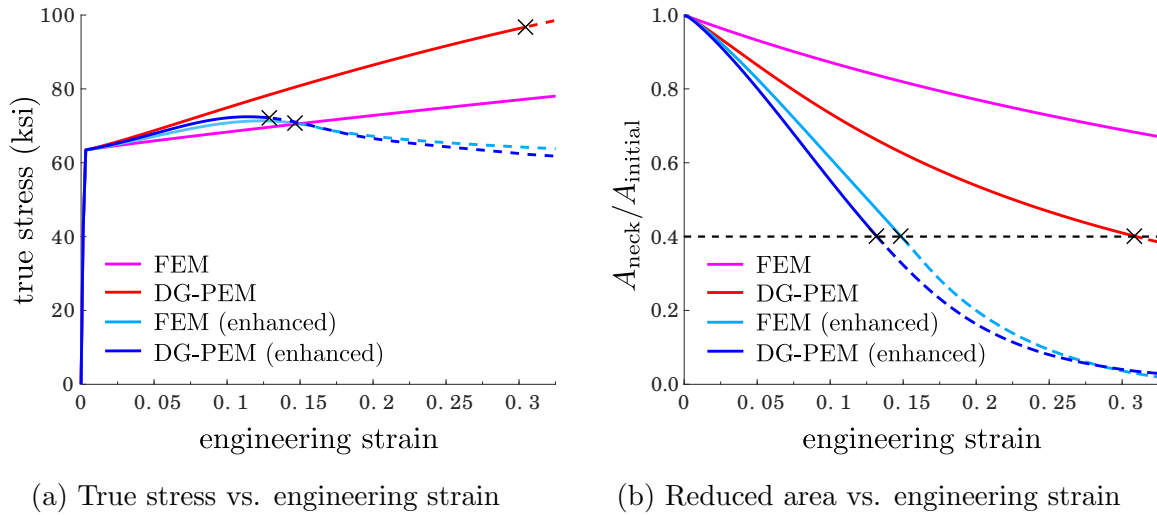


Figure 5.31: Plotted results for the FEM and DG-PEM models, both with and without the kinematic enhancement discussed in [63]. The estimated point of rupture is indicated by an X in each plot.

Without the use of an adequate model for ductile fracture, it is not possible to predict when rupture will occur within the specimen. Nonetheless, an ad hoc metric of 60% reduction in area is used herein to *estimate* the point of rupture, with the % elongation at failure recorded at this point in the analysis. Table 5.15 shows the recorded values of % elongation at failure and maximum tensile stress for the FEM and DG-PEM simulations. These results were compared against a more refined solution obtained using the FEM, showing that the DG-PEM performs comparatively well on the polyhedral mesh at coarser levels of refinement.

If the PEM is employed on the hexahedral mesh in Figure 5.29a, the results are comparable with those of the FEM. As noted in the twisting annulus problem, this suggests that arbitrary polyhedral discretizations may be less sensitive to the effects of volumet-

	% elongation at failure	max tensile stress (ksi)
FEM (enhanced)	14.65	70.74
DG-PEM (enhanced)	12.89	72.15
FEM (refined)	13.35	75.58

Table 5.15: Tensile test data results comparison. The values of % elongation were recorded after reaching 60% reduction in area.

ric locking. The consequences of this decreased sensitivity are further explored in the subsequent problem.

Taylor Bar Impact Problem

A standard problem in the literature entailing high plastic flow is the Taylor bar impact test. For the present study, an impact test for an OFHC copper rod will be investigated. The HTT- α implicit dynamics time integration algorithm [42] is utilized with $\alpha = -0.1$.

For high impact velocities, the Taylor impact test is canonically modeled as a coupled thermo-mechanical problem. Moreover, many finite element simulations ([67], [8]) employ temperature- and strain-rate-dependent material models (such as the model of Johnson and Cook [45]). To avoid over-complicating the subsequent analyses, however, isothermal conditions are assumed. Additionally, the simple (rate-independent) J_2 elasto-plasticity model described previously will be utilized. The following model parameters were taken from [29]: $E = 117$ GPa, $\nu = 0.35$, $Y_0 = 0.4$ GPa, $E_h = 0.1$ GPa, and $\rho_0 = 8,930$ kg/m³.

The experimental procedures detailed in [45] and [40] are emulated. As in [45], the impact specimen was a cylindrical copper rod with an initial height of 30 mm, and an initial diameter of 6 mm. Prior to impact, the rod was given an initial velocity of 200 m/s.

Frictionless contact between the rod and a rigid surface corresponding to $X_3 = 0.0$ was modeled via the inclusion of a penalty traction of the form:

$$\bar{t}_1 = \bar{t}_2 = 0, \quad \bar{t}_3 = p \langle -u_3 | u_3 | \rangle. \quad (5.54)$$

In (5.54), u_3 corresponds to the vertical displacement of a given point on the bottom face of the rod, $\langle \cdot \rangle$ denote the Macaulay brackets, and p is a penalty stiffness parameter. For

the problem at hand, an ad hoc value of $p = 6.0 \times 10^{10} \text{ GPa/mm}^2$ was chosen (following a process of trial-and-error).

The (reflected) quarter-symmetric meshes shown in Figures 5.32a and 5.32b were used in conjunction with the FEM and DG-PEM, respectively. Both meshes consisted of roughly 1000 elements, each.

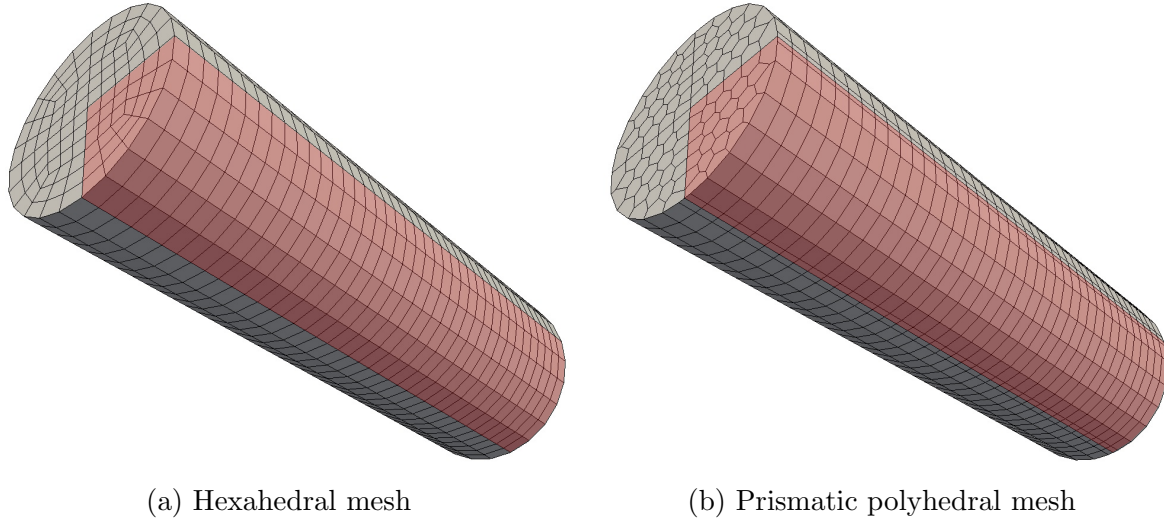
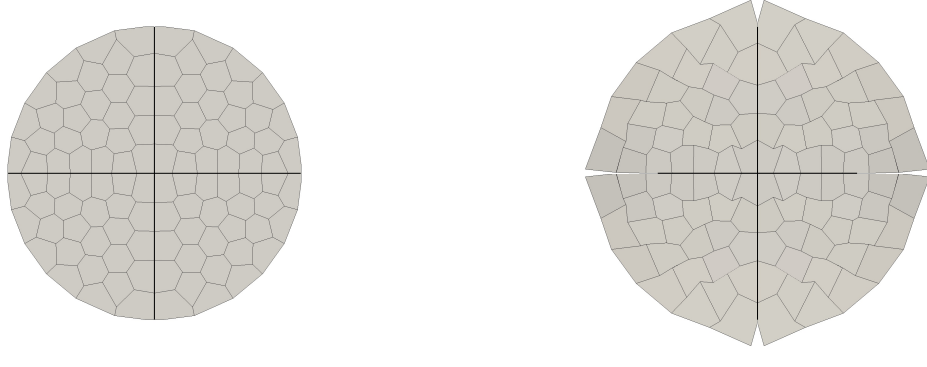


Figure 5.32: Impact specimen meshes used for the Taylor bar problem, modeled using quarter-symmetry.

Because high plastic flow is expected, volumetric locking is a concern. Once again, the kinematic enhancement of [63] is employed to address this issue. However, an interesting result occurs for the Taylor impact problem if the kinematic enhancement is applied to the polyhedral mesh in Figure 5.32b. Specifically, the polyhedral mesh becomes tangled, as illustrated in Figure 5.33. The elements become overly flexible with respect to the isochoric modes of deformation, and inertial effects are sufficient to cause the elements to ultimately invert after just a few time steps. For this reason, a complete analysis could not be run for the DG-PEM using the kinematic enhancement.

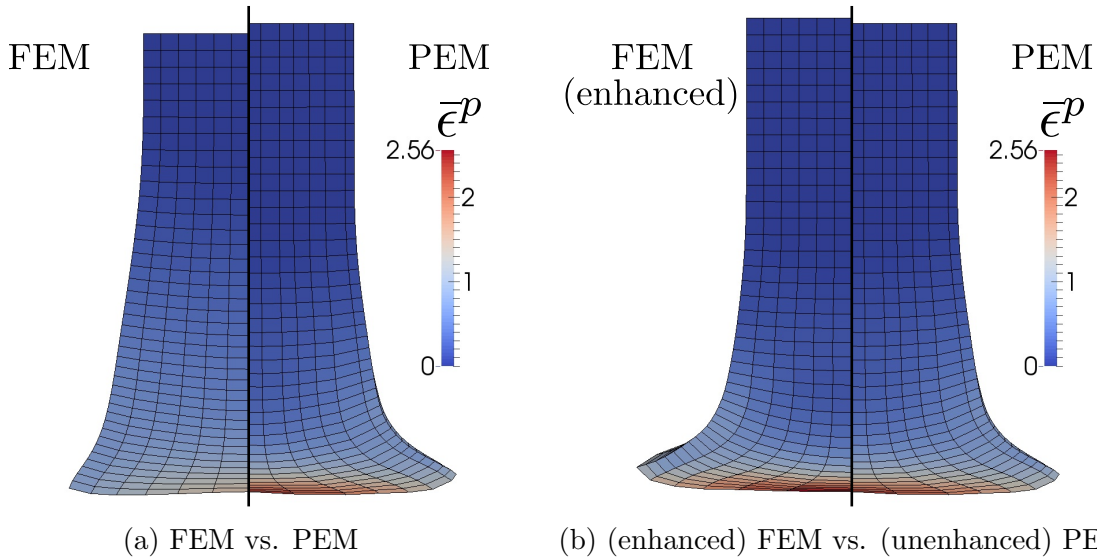
Figures 5.34 and 5.35 provide illustrations of the results of each simulation. Without the kinematic enhancement, the hexahedral FEM mesh clearly suffers from volumetric locking. Interestingly, the polyhedral DG-PEM mesh does not appear to exhibit any serious symptoms of volumetric locking, yielding comparable results to the kinematically enhanced FEM solution.



(a) $t = 0.0 \text{ ms}$

(b) $t = 0.002 \text{ ms}$

Figure 5.33: DG-PEM element inversion when using the kinematic enhancement of [63], viewed from the bottom of the mesh (the impacting surface).



(a) FEM vs. PEM

(b) (enhanced) FEM vs. (unenhanced) PEM

Figure 5.34: Comparison of results between the FEM and PEM models at the final time $t = 0.08 \text{ ms}$, depicting deformed shape and color map values of equivalent plastic strain $\bar{\epsilon}^p$.

To provide a more quantitative comparison of the results obtained for each method, two canonical deformation metrics are considered: the rod's final base diameter D_{final} and compressed length L_{final} , measured after the rod has achieved full impact. The results are displayed in Table 5.16, and compared against a more refined solution obtained using the FEM. Despite the apparent stability issues pertaining to the kinematic enhancement, the data indicate that the DG-PEM performs favorably in comparison with the FEM.

The issue of element inversion when using arbitrary polyhedral discretizations for

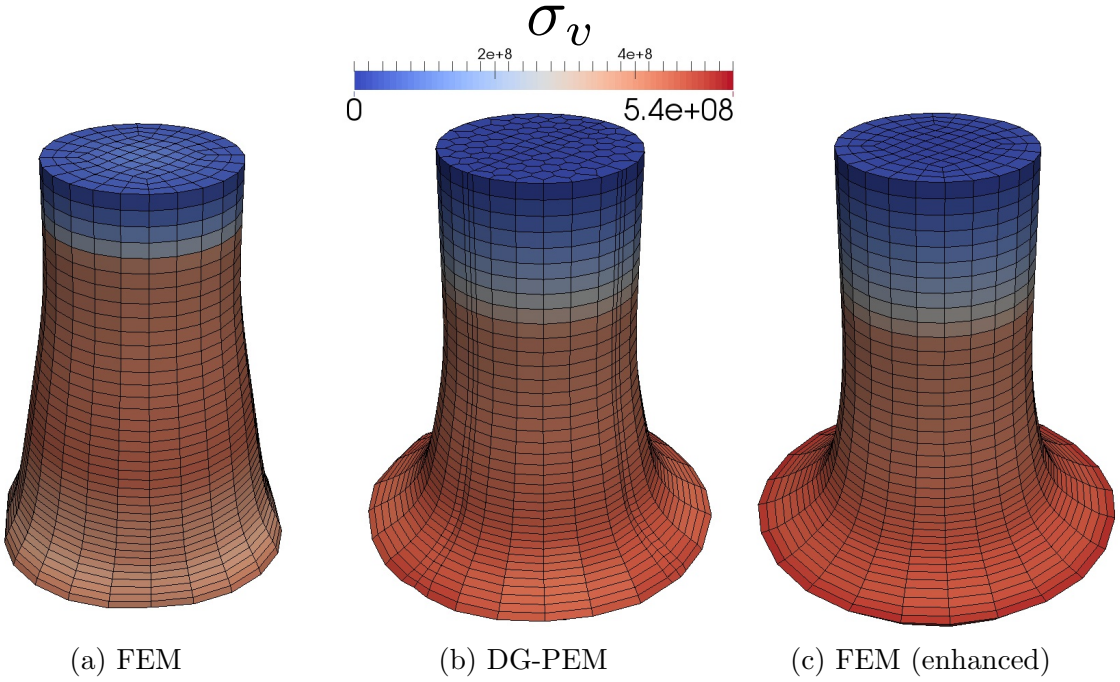


Figure 5.35: Comparison of von Mises stress σ_v (in Pascals) within the FEM and PEM models at the final time $t = 0.08$ ms.

	D_{final} (mm)	L_{final} (mm)
FEM	11.37	23.04
DG-PEM	13.47	23.38
FEM (enhanced)	13.91	23.60
DG-PEM (enhanced)	(unstable)	(unstable)
FEM (refined)	13.87	23.61

Table 5.16: Measurements of the rod’s final base diameter D_{final} and overall length L_{final} .

highly dynamic problems warrants further investigation. Evidently, the kinematic enhancement of [63] is not adequate for general element shapes. Because arbitrary polyhedra possess more nodes (degrees of freedom) than traditional hexahedra, a “mean” dilatation formulation is likely to result in under-constrained modes of deformation. A more intricate, and element-specific enhancement is needed. This issue is left as the subject of future work.

Chapter 6

Conclusions and Future Work

Based upon the preceding investigations, the DG-PEM performs well in comparison to the classical FEM for a variety of large deformation problems. Though the DG-PEM does not directly address the issue of locking, it nonetheless provides an avenue for exploring more general discretizations which may be less sensitive to locking. Additionally, the DG-PEM demonstrates crucial improvements over the CG-PEM and the VETFEM with regard to its ability to tolerate non-convex elements, and elements with comparatively short edges.

Although some initial sensitivity analyses have been conducted for the DG-PEM with regard to the choice of penalty parameters $\alpha_{\sigma 0}$, $\alpha_{\sigma 1}$, a more thorough study is warranted. Particularly for the case where $\epsilon = +1$, $\alpha_{\sigma 0} = \alpha_{\sigma 1} = 0$ (corresponding to the OBB method [58]), such settings may yield integration consistency without having to apply a gradient correction scheme. Additionally, the OBB method is provably stable for approximation spaces consisting of polynomials of order $k = 2$, though this would present a challenge with regard to accurate and efficient numerical integration of quadratic polynomials.

It currently remains to be rigorously proven that the PEM yields a stable integration of the weak form for elements employing an edge-based partition and composite mid-point quadrature. Moreover, the effects of using a gradient correction scheme on high-order elements needs to be investigated further.

An exploration of the PEM for explicit dynamics applications is also warranted. Given the preliminary results that were obtained for the Taylor bar problem (using implicit dynamics), the major challenges would likely be mesh tangling and element inversion.

The stable time step size for explicit analyses may present an additional challenge, being limited by the smallest dimension of any element contained in the mesh. Consequently, the inclusion of elements with short edges may negatively impact the efficiency of the computations for explicit time-stepping if random Voronoi meshes are utilized. However, considering the reasonably well-conditioned element stiffness matrices produced by the DG-PEM for elements with short edges, it may be possible to overcome some of these limitations. Further investigation is required to confirm if this is the case.

Another important consideration for the PEM in the context of non-linear solid mechanics applications is the issue of contact constraint enforcement. Particularly in 3-dimensions, the representation of a given face's shape functions (and its deformed shape) will be discontinuous if the DG-PEM is employed. Consequently, it is not clear how best to enforce contact constraints upon these discontinuous surfaces. Moreover, if the intermediary information regarding the representation of a given element face's shape functions is ultimately discarded prior to the beginning of the analysis (as suggested in 4), then there would be no clear way to evaluate gap functions. The use of the PEM for contact applications would therefore necessitate storage of each boundary face's geometric partition. Additionally, the shape functions for these faces would need to be represented explicitly as piecewise polynomial fields.

A node-on-face method of contact enforcement would likely present a number of challenges for the DG-PEM, owing to the inherently discontinuous representation of the deformed mesh boundary. The CG-PEM may be preferred in this setting, if only for the sake of defining shape functions on element faces. In contrast, a face-on-face method may be capable of handling contact between discontinuous surfaces. Specifically, the mortar-based approach proposed in [87] constructs a projected medial plane between each pair of contacting faces, enforcing a zero-mean gap condition between each overlapping face pair. The use of such projections may allow for the DG-PEM to be utilized directly, even if the geometric representation for each face is discontinuous.

Ongoing efforts are currently directed at improving the resistance of PEM elements to traditional forms of locking, including volumetric locking, and shear locking for thin

elements. Numerous attempts were made to try to improve the bending behavior of thin elements, in particular, but these encountered various issues. An examination of enhanced strain formulations in the context of PEM may yield fruitful results. In particular, because the PEM establishes a local approximation space to construct an element's shape functions, this same space could be utilized to construct a set of enhancement functions, specific to each element.

Another issue that was given considerable attention was the subject of non-planar faces and non-linear edges. Within this setting, it suffices to say that the preservation of polynomial completeness is not a trivial matter. Various approaches to address this issue were explored, though they all invariably encountered issues of numerical precision for nearly-planar faces and nearly-linear edges, resulting in very poor interpolation errors. Most of the aforementioned investigations examined only cases where the faces/edges were represented as piecewise linear manifolds. The consideration of curved geometries (such as NURBS surfaces) would present an additional challenge.

Extending the DG-PEM approach to higher-order elements (beyond $k = 2$) poses a number of practical barriers, particularly with regard to efficiency. For successively higher order elements, the size of the local DG-PEM problems arising from (4.18) can become large. The assembly and solution of these systems of equations will therefore impart a large computational expense for analyses with high-order elements. In such cases, solving (4.18) directly may be impractical. As a possible alternative, it may be sufficient to solve (4.18) using an iterative approach, such as the conjugate gradient method. Certain essential characteristics of the resulting solution would need to be preserved, namely: polynomial completeness, and rank sufficiency of the resulting element stiffness matrices. If successful, such an approach could greatly reduce the computational burden of the PEM shape function construction procedure.

However, the performance of any iterative solver typically depends upon the numerical conditioning of the associated linear system of equations. Poor conditioning of the DG-PEM equation systems would therefore present a major obstacle to the aforementioned approach. Even for reasonably well-scaled polynomial bases, preconditioning would likely

be required to address this issue. Given the structure of the PEM, a geometric multigrid-based preconditioner could be readily obtained, though a simple Jacobi (diagonal) preconditioner might suffice. A more thorough investigation would need to be carried out to determine the efficacy of any iterative approach for constructing PEM shape functions.

Finally, an investigation into the computational efficiency of the PEM still needs to be carried out. The computational expense of the PEM shape function construction procedure should be quantified in this setting. For general polyhedral discretizations, it is expected (and informally observed for the problems considered in this work) that the classical FEM outperforms the DG-PEM on meshes with comparable numbers of elements. Two key observations may explain this behavior: in comparison to polyhedral meshes with the same number of elements, hexahedral meshes typically possess fewer nodes (degrees of freedom), and the bandwidth of the resulting global stiffness matrix tends to be smaller, as well. Moreover, elements with arbitrary topology necessitate the use of data structures with variable size, incurring an additional overhead. The FEM is therefore expected to yield better computational efficiency, in general. Nonetheless, the PEM could potentially enable the use of novel linear solution methodologies (such as geometric multigrid methods), exploiting the geometric flexibility of the elements. Such approaches could help to improve the overall efficiency of the PEM.

Appendix A

An Exact Solution for the Incompressible Twisting Annulus Problem

An exact solution for the twisting annulus problem described in chapter 5 may be obtained by considering the stress divergence equations in cylindrical polar coordinates:

$$\nabla \cdot \boldsymbol{\sigma} = \left\{ \begin{array}{l} \frac{\partial \sigma_{rr}}{\partial r} + \frac{\sigma_{rr}}{r} + \frac{1}{r} \frac{\partial \sigma_{\theta r}}{\partial \theta} + \frac{\partial \sigma_{zr}}{\partial z} - \frac{\sigma_{\theta \theta}}{r} \\ \frac{1}{r} \frac{\partial \sigma_{\theta \theta}}{\partial \theta} + \frac{\partial \sigma_{r\theta}}{\partial r} + \frac{\sigma_{r\theta}}{r} + \frac{\sigma_{\theta r}}{r} + \frac{\partial \sigma_{z\theta}}{\partial z} \\ \frac{\partial \sigma_{zz}}{\partial z} + \frac{\partial \sigma_{rz}}{\partial r} + \frac{\sigma_{rz}}{r} + \frac{1}{r} \frac{\partial \sigma_{\theta z}}{\partial \theta} \end{array} \right\} = \mathbf{0}. \quad (\text{A.1})$$

By the assumptions of plane strain and axisymmetry, it is rationalized that $\boldsymbol{\sigma}(r)$ must be a function of r , alone. Therefore:

$$\nabla \cdot \boldsymbol{\sigma} = \left\{ \begin{array}{l} \frac{\partial \sigma_{rr}}{\partial r} + \frac{\sigma_{rr} - \sigma_{\theta \theta}}{r} \\ \frac{\partial \sigma_{r\theta}}{\partial r} + \frac{2\sigma_{r\theta}}{r} \\ \frac{\partial \sigma_{rz}}{\partial r} + \frac{\sigma_{rz}}{r} \end{array} \right\} = \mathbf{0}. \quad (\text{A.2})$$

Furthermore, by the assumptions of plane strain, it is observed that $\sigma_{rz} = 0$ and $\sigma_{\theta z} = 0$. Additionally, imposing the incompressibility condition $\nabla \cdot \mathbf{v} = \text{tr}(\mathbf{D}) = 0$:

$$\text{tr}(\dot{\boldsymbol{\sigma}}) = 0 \Rightarrow \text{tr}(\boldsymbol{\sigma}) = 0 \forall t. \quad (\text{A.3})$$

Suppose that $p = \sigma_{zz} = 0$, and therefore $\sigma_{\theta\theta} = -\sigma_{rr}$. This yields 2 governing differential equations for σ_{rr} and $\sigma_{r\theta}$:

$$\frac{\partial \sigma_{rr}}{\partial r} + \frac{2\sigma_{rr}}{r} = 0, \quad \frac{\partial \sigma_{r\theta}}{\partial r} + \frac{2\sigma_{r\theta}}{r} = 0, \quad (\text{A.4})$$

whose solutions are of the form

$$\sigma_{rr} = \frac{\sigma}{r^2}, \quad \sigma_{r\theta} = \frac{\tau}{r^2}, \quad (\text{A.5})$$

where $\sigma(t)$ and $\tau(t)$ are independent functions of time. Consequently,

$$\begin{Bmatrix} \sigma_{rr} \\ \sigma_{\theta\theta} \\ \sigma_{r\theta} \end{Bmatrix} = r^{-2} \begin{Bmatrix} +\sigma \\ -\sigma \\ \tau \end{Bmatrix}. \quad (\text{A.6})$$

Under the assumption of incompressibility, the velocity field is $v_r = 0$, $v_z = 0$, and $v_\theta(r) = r\dot{\phi}(r)$, for some $\phi(r, t)$. The velocity gradient (in cylindrical polar coordinates) is written:

$$\mathbf{L} = \nabla \mathbf{v} = \begin{bmatrix} v_{r,r} & v_{r,\theta}/r - v_\theta/r & v_{r,z} \\ v_{\theta,r} & v_{\theta,\theta}/r + v_r/r & v_{\theta,z} \\ v_{z,r} & v_{z,\theta}/r & v_{z,z} \end{bmatrix} = \begin{bmatrix} 0 & -\dot{\phi} & 0 \\ \dot{\phi} + r\dot{\phi}_{,r} & 0 & 0 \\ 0 & 0 & 0 \end{bmatrix}. \quad (\text{A.7})$$

The corresponding rate of deformation and spin tensors are:

$$\mathbf{D} = \frac{r\dot{\phi}_{,r}}{2} \begin{bmatrix} 0 & +1 & 0 \\ +1 & 0 & 0 \\ 0 & 0 & 0 \end{bmatrix}, \quad \mathbf{W} = \frac{2\dot{\phi} + r\dot{\phi}_{,r}}{2} \begin{bmatrix} 0 & -1 & 0 \\ +1 & 0 & 0 \\ 0 & 0 & 0 \end{bmatrix}. \quad (\text{A.8})$$

The stress rate equations resulting from $\dot{\boldsymbol{\sigma}} = \mathbb{C} : \mathbf{D} + \mathbf{W}\boldsymbol{\sigma} - \boldsymbol{\sigma}\mathbf{W}$ are

$$\begin{Bmatrix} \dot{\sigma}_{rr} \\ \dot{\sigma}_{\theta\theta} \\ \dot{\sigma}_{r\theta} \end{Bmatrix} = \begin{Bmatrix} 0 \\ 0 \\ \mu r \dot{\phi}_{,r} \end{Bmatrix} + (2\dot{\phi} + r\dot{\phi}_{,r}) \begin{Bmatrix} -\sigma_{r\theta} \\ \sigma_{r\theta} \\ \sigma_{rr} \end{Bmatrix}, \quad (\text{A.9})$$

or (in terms of σ, τ):

$$\begin{Bmatrix} \dot{\sigma} \\ \dot{\tau} \end{Bmatrix} = \begin{Bmatrix} 0 \\ \mu r^3 \dot{\phi}_{,r} \end{Bmatrix} + (2\dot{\phi} + r\dot{\phi}_{,r}) \begin{bmatrix} 0 & -1 \\ 1 & 0 \end{bmatrix} \begin{Bmatrix} \sigma \\ \tau \end{Bmatrix}, \quad (\text{A.10})$$

which must be valid for all r, t . Assume that $\dot{\phi}(r)$ is a function of r (and not of t), corresponding to a steady rate of deformation. By recognizing that $\sigma_{,r} = \tau_{,r} = 0$, one obtains the condition

$$3\dot{\phi}_{,r} + r\dot{\phi}_{,rr} = 0, \quad (\text{A.11})$$

implying $\dot{\phi}_{,r} = Br^{-3}$, and $\phi(r, t) = (A - Br^{-2}/2)t$. Thus

$$\begin{Bmatrix} \dot{\sigma} \\ \dot{\tau} \end{Bmatrix} = \begin{Bmatrix} 0 \\ \mu B \end{Bmatrix} + 2A \begin{bmatrix} 0 & -1 \\ 1 & 0 \end{bmatrix} \begin{Bmatrix} \sigma \\ \tau \end{Bmatrix}, \quad (\text{A.12})$$

and

$$\sigma(t) = -\frac{\mu B}{2A} - C_2 \sin(2At) + C_1 \cos(2At), \quad (\text{A.13})$$

$$\tau(t) = C_1 \sin(2At) + C_2 \cos(2At). \quad (\text{A.14})$$

Imposing the initial conditions $\sigma(0) = \tau(0) = 0$ results in:

$$\sigma(t) = \frac{\mu B}{2A} [\cos(2At) - 1], \quad \tau(t) = \frac{\mu B}{2A} \sin(2At). \quad (\text{A.15})$$

Imposing the boundary conditions $\phi(R_i, t) = 0 \forall t$, $\phi(R_o, t) = \Phi t \forall t$ yields:

$$A = \frac{R_o^2}{R_o^2 - R_i^2} \Phi, \quad B = 2 \frac{R_o^2 R_i^2}{R_o^2 - R_i^2} \Phi. \quad (\text{A.16})$$

The final analytical solutions for the displacement and stress fields are:

$$u_r = u_z = 0, \quad u_\theta = \frac{R_o^2}{r} \frac{r^2 - R_i^2}{R_o^2 - R_i^2} \Phi t, \quad (\text{A.17})$$

$$\sigma_{rr} = -\sigma_{\theta\theta} = \mu \frac{R_i^2}{r^2} \left[\cos \left(2 \frac{R_o^2}{R_o^2 - R_i^2} \Phi t \right) - 1 \right], \quad \sigma_{r\theta} = \mu \frac{R_i^2}{r^2} \sin \left(2 \frac{R_o^2}{R_o^2 - R_i^2} \Phi t \right). \quad (\text{A.18})$$

According to [12], the above solution for $\sigma_{r\theta}$ is also valid for compressible elastic materials.

REFERENCES

- [1] *LS-DYNA Keyword User's Manual, Volume II: Material Models.*
- [2] D. N. Arnold, D. Boffi, and R. S. Falk. Approximation by quadrilateral finite elements. *Mathematics of Computation*, 71(239):909–922, 2002.
- [3] D. N. Arnold, D. Boffi, R. S. Falk, and L. Gastaldi. Finite element approximation on quadrilateral meshes. *Communications in Numerical Methods in Engineering*, 17(11):805–812, 2001.
- [4] Utkarsh Ayachit. *The ParaView Guide: A Parallel Visualization Application.*
- [5] Ivo Babuška. Error-bounds for finite element method. *Numerische Mathematik*, 16:322–333, 1971.
- [6] Ivo Babuška and Manil Suri. Locking effects in the finite element approximation of elasticity problems. *Numerische Mathematik*, 62:439–463, 1992.
- [7] Ivo Babuška and Manil Suri. On locking and robustness in the finite element method. *SIAM Journal on Numerical Analysis*, 29(5):1261–1293, 1992.
- [8] Biswajit Banerjee. Taylor impact tests: Detailed report. *C-SAFE Internal Report*, Report No. C-SAFE-CD-IR-05-001, 2005.
- [9] F. Bassi, L. Botti, A. Colombo, D.A. Di Pietro, and P. Tesini. On the flexibility of agglomeration based physical space discontinuous galerkin discretizations. *Journal of Computational Physics*, 231(1):45 – 65, 2012.
- [10] G.P. Bazeley, Y.K. Cheung, B.M. Irons, and O.C. Zienkiewicz. Triangular elements in bending. conforming and non-conforming solutions. *Proc. Conf. Matrix Methods in Structural Mechanics*, 1965.
- [11] J. E. Bishop. A displacement-based finite element formulation for general polyhedra using harmonic shape functions. *International Journal for Numerical Methods in Engineering*, 97:1–31, 2014.
- [12] Rebecca Brannon. Annulus twist as a verification test.
- [13] Franco Brezzi. On the existence, uniqueness and approximation of saddle-point problems arising from lagrangian multipliers. *ESAIM: Mathematical Modelling and Numerical Analysis - Modlisation Mathmatique et Analyse Numrique*, 8:129–151, 1974.
- [14] Erik Burman. A penalty-free nonsymmetric nitsche-type method for the weak imposition of boundary conditions. *SIAM Journal on Numerical Analysis*, 50(4):1959–1981, 2012.

- [15] Jiun-Shyan Chen, Michael Hillman, and Marcus Rüter. An arbitrary order variationally consistent integration for galerkin meshfree methods. *International Journal for Numerical Methods in Engineering*, 95:387–418, 2013.
- [16] H. Chi, L. Beirão da Veiga, and G. H. Paulino. Some basic formulations of the virtual element method (vem) for finite deformations. *Computer Methods in Applied Mechanics and Engineering*, 318:148–192, 2017.
- [17] Heng Chi, Cameron Talischi, Oscar Lopez-Pamies, and Glaucio H. Paulino. A paradigm for higher-order polygonal elements in finite elasticity using a gradient correction scheme. *Computer Methods in Applied Mechanics and Engineering*, 306:216–251, 2016.
- [18] Eric B. Chin, Jean B. Lasserre, and N. Sukumar. Numerical integration of homogeneous functions on convex and nonconvex polygons and polyhedra. *Computational Mechanics*, 56:967–981, 2015.
- [19] Zhong ci Shi. The f-e-m-test for convergence of nonconforming finite elements. *Mathematics of Computation*, 49(180):391–405, 1987.
- [20] M. Cicuttin, D.A. Di Pietro, and A. Ern. Implementation of discontinuous skeletal methods on arbitrary-dimensional, polytopal meshes using generic programming. *Journal of Computational and Applied Mathematics*, 2017.
- [21] L. Beirão da Veiga, F. Brezzi, A. Cangiani, G. Manzini, L. D. Marini, and A. Russo. Basic principles of virtual element methods. *Computer Methods in Applied Mechanics and Engineering*, 23:199–214, 2013.
- [22] L. Beirão da Veiga, C. Lovadina, and D. Mora. A virtual element method for elastic and inelastic problems on polytope meshes. *Computer Methods in Applied Mechanics and Engineering*, 295:327–346, 2015.
- [23] E. A. de Souza Neto, D. Perić, M. Dukto, and D. R. J. Owen. Design of simple low order finite elements for large strain analysis of nearly incompressible solids. *International Journal of Solids and Structures*, 33:3277–3296, 1996.
- [24] C. R. Dohrmann and M. M. Rashid. Polynomial approximation of shape function gradients from element geometries. *International Journal for Numerical Methods in Engineering*, 53:945–958, 2002.
- [25] D. A. Dunavant. High degree efficient symmetrical gaussian quadrature rules for the triangle. *International Journal for Numerical Methods in Engineering*, 21(6):1129–1148, 1985.
- [26] Standard test methods for tension testing of metallic materials. Standard, ASTM International, 100 Barr Harbor Drive, PO Box C700, West Conshohocken, PA 19428-2959, United States, 2008.

- [27] Mohamed S. Ebeida and Scott A. Mitchell. Uniform random voronoi meshes. *Proceedings of the 20th International Meshing Roundtable*, pages 273–290, 2011.
- [28] Mohamed Salah Ebeida. Vorocrust v. 1.0, Jul 2017.
- [29] Tobias Erhart. Review of solid element formulations in ls-dyna, 2011.
- [30] Carlos A. Felippa. *Introduction to Finite Element Methods*. University of Colorado, Boulder, 2004.
- [31] Sonia Fernndez-Mndez and Antonio Huerta. Imposing essential boundary conditions in mesh-free methods. *Computer Methods in Applied Mechanics and Engineering*, 193(12):1257 – 1275, 2004. Meshfree Methods: Recent Advances and New Applications.
- [32] D. P. Flanagan and T. Belytschko. A uniform strain hexahedron and quadrilateral with orthogonal hourglass control. *International Journal for Numerical Methods in Engineering*, 17:679–706, 1981.
- [33] Michael S. Floater. Mean value coordinates. *Computer Aided Geometric Design*, 20:19–27, 2003.
- [34] Jouni Freund and Rolf Stenberg. On weakly imposed boundary conditions for second order problems. pages 327–336, 01 1995.
- [35] Arun Gain, Cameron Talischi, and Glaucio H. Paulino. On the virtual element method for three-dimensional elasticity problems on arbitrary polyhedral meshes. *Computer Methods in Applied Mechanics and Engineering*, 282, 11 2013.
- [36] Xifeng Gao, Wenzel Jakob, Marco Tarini, and Daniele Panozzo. Robust hex-dominant mesh generation using field-guided polyhedral agglomeration. *ACM Transactions on Graphics*, 36, 2017.
- [37] W. W. Gerberich, H. E. Martens, and R. A. Boundy. Tensile properties of five low-alloy and stainless steels under high-heating-rate and constant-temperature conditions. *Jet Propulsion Laboratory*, Technical Report No. 32-222, 1962.
- [38] William J. Gordon and James A. Wixom. Pseudo-harmonic interpolation on convex domains. *SIAM Journal on Numerical Analysis*, 11(5):909–933, 1974.
- [39] Axel Grundmann and H. M. Möller. Invariant integration formulas for the n-simplex by combinatorial methods. *SIAM Journal on Numerical Analysis*, 15(2):282–290, 1978.
- [40] W. H. Gust. High impact deformation of metal cylinders at elevated temperatures. *Journal of Applied Physics*, 53(5):3566–3575, 1982.

- [41] Jan S. Hesthaven and Tim Warburton. *Nodal Discontinuous Galerkin Methods: Algorithms, Analysis, and Applications*. Springer Publishing Company, Incorporated, 1st edition, 2010.
- [42] Hans M. Hilber, Thomas J. R. Hughes, and Robert L. Taylor. Improved numerical dissipation for time integration algorithms in structural dynamics. *Earthquake Engineering & Structural Dynamics*, 5(3):283–292, 1977.
- [43] Thomas J. R. Hughes. *The Finite Element Method—Linear Static and Dynamic Finite Element Analysis*. Dover Publications, 2000.
- [44] Aerospace Specification Metals Inc. Aisi 4130 steel, normalized at 870c (1600f), 2018.
- [45] G.R. Johnson and W.H. Cook. A constitutive model and data for metals subjected to large strains, high strain rates, and high temperatures. *Proceedings 7th International Symposium on Ballistics, The Hague*, 19-21:541–547, April 1983.
- [46] Pushkar Joshi, Mark Meyer, Tony DeRose, Brian Green, and Tom Sanocki. Harmonic coordinates for character articulation. *ACM Transactions on Graphics*, 26, 2007.
- [47] Mika Juntunen and Rolf Stenberg. Nitsche’s method for general boundary conditions. *Mechanics of Computation*, 78(267):1353–1374, 2009.
- [48] Hyo Young Seop Kim, Sung Ho Kim, and Woo-Seog Ryu. Finite element analysis of the onset of necking and the post-necking behaviour during uniaxial tensile testing. *MATERIALS TRANSACTIONS*, 46(10):2159–2163, 2005.
- [49] Nam-Sua Lee and Klaus-Jürgen Bathe. Effects of element distortions on the performance of isoparametric elements. *International Journal for Numerical Methods in Engineering*, 36:3553–3576, 1993.
- [50] Qiaoluan H. Li and Junping Wang. Weak galerkin finite element methods for parabolic equations. *Numerical Methods for Partial Differential Equations*, 29:2004–2024, 2013.
- [51] Guang Lin, Jiangguo Liu, and Farrah Sadre-Marandi. A comparative study on the weak galerkin, discontinuous galerkin, and mixed finite element methods. *Journal of Computational and Applied Mathematics*, 273:346–362, 2015.
- [52] Richard H. MacNeal. A theorem regarding the locking of tapered four-noded membrane elements. *International Journal for Numerical Methods in Engineering*, 24:1793–1799, 1987.
- [53] David S. Malkus and Thomas J.R. Hughes. Mixed finite element methods reduced and selective integration techniques: A unification of concepts. *Computer Methods in Applied Mechanics and Engineering*, 15(1):63 – 81, 1978.

- [54] Sebastian Martin, Peter Kaufmann, Mario Botsch, Martin Wicke, and Markus Gross. Polyhedral finite elements using harmonic basis functions. *Eurographics Symposium on Geometry Processing 2008*, 27(5), 2008.
- [55] L. Mu, J. Wang, and Y. Wang. A computational study of the weak galerkin method for second-order elliptic equations. *Numerical Algorithms*, 63:753, 2013.
- [56] L. Mu, J. Wang, and X. Ye. Weak galerkin finite element method for second-order elliptic problems on polytopal meshes. *International Journal of Numerical Analysis and Modeling.*, 12:31–53, 2015.
- [57] Lin Mu, Junping Wang, and Xiu Ye. A weak galerkin finite element method with polynomial reduction. *Journal of Computational and Applied Mathematics*, 285:45–58, 2015.
- [58] J.Tinsley Oden, Ivo Babuška, and Carlos Erik Baumann. A discontinuoushpfinite element method for diffusion problems. *J. Comput. Phys.*, 146(2):491–519, October 1998.
- [59] Daniel Pantuso and Klaus-Jürgen Bathe. On the stability of mixed finite elements in large strain analysis of incompressible solids. *Finite Elements in Analysis and Design*, 28:83–104, 1997.
- [60] M. M. Rashid. Incremental kinematics for finite element applications. *International Journal for Numerical Methods in Engineering*, 36:3937–3956, 1993.
- [61] M. M. Rashid and P. M. Gullett. On a finite element method with variable element topology. *Computer Methods in Applied Mechanics and Engineering*, 190:1509–1527, 2000.
- [62] M. M. Rashid and A. Sadri. The partitioned element method in computational solid mechanics. *Computer Methods in Applied Mechanics and Engineering*, 237–240:152–165, 2012.
- [63] M. M. Rashid and M. Selimotić. A three-dimensional finite element method with arbitrary polyhedral elements. *International Journal for Numerical Methods in Engineering*, 67:226–252, 2006.
- [64] J.-F. Remacle, J. Lambrechts, B. Seny, E. Marchandise, A. Johnen, and C. Geuzainet. Blossom-quad: a non-uniform quadrilateral mesh generator using a minimum cost perfect matching algorithm. *International Journal for Numerical Methods in Engineering*, 89:1102–1119, 2012.
- [65] Béatrice Rivière. *Discontinuous Galerkin Methods for Solving Elliptic and Parabolic Equations: Theory and Implementation*. Society for Industrial and Applied Mathematics, 3600 Market Street, 6th Floor, Philadelphia, PA 19104-2688 USA, 2008.

- [66] Béatrice Rivière, Mary F. Wheeler, and Vivette Girault. A priori error estimates for finite element methods based on discontinuous approximation spaces for elliptic problems. *SIAM Journal on Numerical Analysis*, 39(3):902–931, 2001.
- [67] A. C. Robinson, Martin W. Heinstein, and Guglielmo Scovazzi. Lagrangian modeling at sandia national laboratories: Current status and future directions. *Proceedings of 5LC*, 19-21:541–547, 2005.
- [68] Mili Selimović. *Polyhedral Finite-Element Approximants in 3D Solid Mechanics*. PhD thesis, University of California, Davis, 2008.
- [69] J. C. Simo and F. Armero. Geometrically non-linear enhanced strain mixed methods and the method of incompatible modes. *International Journal for Numerical Methods in Engineering*, 33:1413–1449, 1992.
- [70] J. C. Simo, F. Armero, and R. L. Taylor. Improved versions of assumed enhanced strain tri-linear elements for 3d finite deformation problems. *Computer Methods in Applied Mechanics and Engineering*, 110:359–386, 1993.
- [71] J. C. Simo and M. S. Rifai. A class of mixed assumed strain methods and the method of incompatible modes. *International Journal for Numerical Methods in Engineering*, 29:1595–1638, 1990.
- [72] Friedrich Stummel. The generalized patch test. *SIAM Journal on Numerical Analysis*, 16(3):449–471, 1979.
- [73] Friedrich Stummel. The limitations of the patch test. *International Journal for Numerical Methods in Engineering*, 16:177–188, 1980.
- [74] N. Sukumar. Construction of polygonal interpolants: a maximum entropy approach. *International Journal for Numerical Methods in Engineering*, 61:2159–2181, 2004.
- [75] Manil Suri. On the robustness of the h - and p -versions of the finite-element method. *Journal of Computational and Applied Mathematics*, 35:303–310, 1991.
- [76] Theodore Sussman and Klaus-Jürgen Bathe. Spurious modes in geometrically non-linear small displacement finite elements with incompatible modes. *Computers & Structures*, 140:14–22, 2014.
- [77] Cameron Talischi and Glaucio H. Paulino. Addressing integration error for polygonal finite elements through polynomial projections: A patch test connection. *Mathematical Models and Methods in Applied Sciences*, 24:1701–1727, 2014.
- [78] Cameron Talischi, Glaucio H. Paulino, Anderson Pereira, and Ivan F. M. Menezes. Polymesher: a general-purpose mesh generator for polygonal elements written in matlab. *Structural and Multidisciplinary Optimization*, 45(3):309–328, Mar 2012.

- [79] Cameron Talischi, Anderson Pereira, Ivan F. M. Menezes, and Glaucio H. Paulino. Gradient correction for polygonal and polyhedral finite elements. *International Journal for Numerical Methods in Engineering*, 102:728–747, 2015.
- [80] R. L. Taylor, J. C. Simo, O. C. Zienkiewicz, and A. C. H. Chan. The patch test condition for assessing fem convergence. *International Journal for Numerical Methods in Engineering*, 22(1):39–62, 1986.
- [81] Eugene L. Wachspress. *A Rational Finite Element Basis*. Academic Press, 1975.
- [82] J. Wang and X. Ye. A weak galerkin finite element method for second-order elliptic problems. *Journal of Computational and Applied Mathematics*, 241:103–115, 2013.
- [83] X. Wang, N.S. Malluwawadu, F. Gao, and T.C. McMillan. A modified weak galerkin finite element method. *Journal of Computational and Applied Mathematics*, 271:319–329, 2014.
- [84] Wikiversity. Introduction to elasticity/plate with hole in tension, 2017.
- [85] E.L. Wilson, R. Taylor, W.P. Doherty, and Jamshid Ghaboussi. *Incompatible Displacement Models*. 12 1973.
- [86] Robert Winkler. Comments on membrane locking. *Proceedings in Applied Mathematics and Mechanics*, 10:229–230, 2010.
- [87] Steven R. Wopschall. *A Novel Face-on-Face Contact Method for Nonlinear Solid Mechanics*. PhD thesis, 2017.

Brian Doran Giffin
December 2017
Civil and Environmental Engineering

A POLYTOPAL ELEMENT FRAMEWORK FOR
IMPROVED SOLUTION ACCURACY AND ROBUSTNESS

Abstract

The abstract that is submitted to UMI must be formatted as shown in the example here. The body of the abstract cannot exceed 350 words. It should be in typewritten form, double-spaced, and on bond paper. It is important to write an abstract that gives a clear description of the content and major divisions of the dissertation, since UMI will publish the abstract exactly as submitted. Students completing their requirements under Plan A should provide extra copies of the typed summary for use by the dissertation committee during the examination.

The abstract that is submitted to UMI must be formatted as shown in the example here. The body of the abstract cannot exceed 350 words. It should be in typewritten form, double-spaced, and on bond paper. It is important to write an abstract that gives a clear description of the content and major divisions of the dissertation, since UMI will publish the abstract exactly as submitted. Students completing their requirements under Plan A should provide extra copies of the typed summary for use by the dissertation committee during the examination.

The abstract that is submitted to UMI must be formatted as shown in the example here. The body of the abstract cannot exceed 350 words. It should be in typewritten form, double-spaced, and on bond paper. It is important to write an abstract that gives a clear description of the content and major divisions of the dissertation, since UMI will publish the abstract exactly as submitted. Students completing their requirements under Plan A should provide extra copies of the typed summary for use by the dissertation committee during the examination.

The abstract that is submitted to UMI must be formatted as shown in the example here. The body of the abstract cannot exceed 350 words. It should be in typewritten

form, double-spaced, and on bond paper. It is important to write an abstract that gives a clear description of the content and major divisions of the dissertation, since UMI will publish the abstract exactly as submitted. Students completing their requirements under Plan A should provide extra copies of the typed summary for use by the dissertation committee during the examination.